

**Calibration of the Flow in the Test  
Section of the Low-Speed Wind Tunnel  
at AMRL**

Lincoln P. Erm

DSTO-TR-1073

20020108 143

# Calibration of the Flow in the Test Section of the Low-Speed Wind Tunnel at AMRL

*Lincoln P. Erm*

**Air Operations Division  
Aeronautical and Maritime Research Laboratory**

DSTO-TR-1073

## ABSTRACT

The circuit of the low-speed wind tunnel remained essentially the same from when the tunnel was built in 1941 until 1996 when an extended test section and a new contraction were installed. In this report, the results of a detailed calibration of the flow in the test section are given for the tunnel with the contraction as installed from 1941 to 1996. The calibration was performed to: (1) provide a data base of the flow quality, to be used when analysing tests carried out between 1941 and 1996, and (2) provide a data base for assessing the changes in the flow quality resulting from the new contraction and extended test section installed in 1996. Longitudinal mean-flow velocities, flow angles, turbulence intensities and spectra, were measured at up to 155 grid points across the flow for longitudinal positions of  $x_T = -1.0, 0.0$  and  $1.0$  m from the centre of the turntables in the test section for nominal free-stream velocities of 30, 45, 60 and 75 m/s. The most important area of the test section, where models are usually located, is the region comprising approximately the central 50% of the cross sectional area of the test section. In this region, over the longitudinal measurement range ( $x_T = -1.0$  to  $1.0$  m), the following flow non-uniformities were observed. For the four velocities, longitudinal mean-flow velocities deviated within the range  $-0.8\%$  to  $+2.0\%$  from their values at the centre of the tunnel test section ( $x_T = 0.0$  m). For velocities of 30 and 60 m/s, horizontal flow angles deviated within the range  $-0.8^\circ$  to  $+0.8^\circ$  and vertical flow angles deviated within the range  $-1.0^\circ$  to  $+0.4^\circ$ . For velocities of 30 and 60 m/s, the u-component turbulence intensities were generally below 0.4%, and the v- and w-component intensities were generally below 0.7%. Corresponding spectra for the u- v- and w-components of the turbulence were relatively smooth over the frequency range 0.3 Hz to 10 kHz, with no significant spikes associated with irregularities in the flow.

## RELEASE LIMITATION

*Approved for public release*

DEPARTMENT OF DEFENCE  
DEFENCE SCIENCE & TECHNOLOGY ORGANISATION

**DSTO**

AQ F02-04-0467

*Published by*

*DSTO*

*Aeronautical and Maritime Research Laboratory*

*506 Lorimer St*

*Fishermans Bend Vic 3207 Australia*

*Telephone: (03) 9626 7000*

*Fax: (03) 9626 7999*

*© Commonwealth of Australia 2000*

*AR-011-637*

*November 2000*

**APPROVED FOR PUBLIC RELEASE**

# Calibration of the Flow in the Test Section of the Low-Speed Wind Tunnel at AMRL

## Executive Summary

The low-speed wind tunnel at the Aeronautical and Maritime Research Laboratory was commissioned in 1941 and it is the major low-speed aerodynamic testing facility for the Department of Defence. The tunnel has a closed return circuit with an octagonal test section 2.74 m wide and 2.13 m high, and it has a maximum velocity in the test section of about 100 m/s. The tunnel circuit remained essentially unchanged from 1941 until 1996, when the length of the test section was increased from 4.12 m to 6.56 m and a new contraction was installed upstream of the original contraction.

The flow in the test section of a wind tunnel is never completely uniform. Detailed measurements need to be taken in the empty test section to see how the flow deviates from location to location. Tunnels are calibrated to: (1) establish if corrections have to be made to test results, (2) indicate what adjustments have to be made to the orientation of a model when testing and (3) assess the suitability of the tunnel for a given test. Although some early calibration measurements were taken in the tunnel for specific purposes, they were not comprehensive.

In this report, the results of a detailed and comprehensive calibration of the flow in the test section are given for the tunnel with the contraction that was in place until 1996. The calibration was performed to: (1) provide an authoritative flow data base to facilitate detailed analysis of all tests conducted between 1941 and 1996, and (2) provide a data base for assessing the changes in the flow quality resulting from installing a new contraction and an extended test section in 1996. An extensive range of longitudinal mean-flow velocities, flow angles, turbulence intensities and spectra were measured in the test section. Data were taken at up to 155 grid points across the flow at each of three longitudinal distances of  $x_T = -1.0, 0.0$  and  $1.0$  m from the centres of the upper and lower turntables in the test section and for nominal free-stream velocities of 30, 45, 60 and 75 m/s.

The most important area of the test section, where models are usually located, is the region comprising approximately the central 0.7 of the width and 0.7 of the height, i.e. approximately the central 50% of the cross sectional area of the test section. In this region, over the longitudinal measurement range ( $x_T = -1.0, 0.0$  and  $1.0$  m), the following flow non-uniformities were observed. For velocities of 30, 45, 60 and 75 m/s, longitudinal mean-flow velocities deviated within the range  $-0.8\%$  to  $+2.0\%$  from their values at the centre of the tunnel test section ( $x_T = 0.0$  m). For velocities of 30 and 60 m/s, horizontal flow angles deviated within the range  $-0.8^\circ$  to  $+0.8^\circ$  and vertical flow angles deviated within the range  $-1.0^\circ$  to  $+0.4^\circ$ . For velocities of 30 and 60 m/s, the u-component turbulence intensities were generally below 0.4%, and the v- and w-component intensities were generally below 0.7%. Spectra for the u- v- and w-components of the turbulence were relatively smooth over the frequency range 0.3 Hz to 10 kHz, with no significant spikes which are associated with irregularities in the flow. The literature indicates that, for a tunnel similar to that at AMRL, a variation of up to 0.6% for longitudinal mean-flow velocity is acceptable and that flow angles should not exceed  $0.4^\circ$ . In addition, the u-component intensities should be less than about 0.1% for research tunnels, although intensities as high as 0.5% are acceptable for tunnels used for developmental testing. The measurements for the AMRL low-speed wind tunnel are generally on a par with other similar tunnels, but some improvement in the quality of the flow in the test section of the AMRL tunnel would be beneficial.



## Author



### **Lincoln P. Erm**

Air Operations Division

*Lincoln Erm obtained a Bachelor of Engineering (Mechanical) degree in 1967 and a Master of Engineering Science degree in 1969, both from the University of Melbourne. His Master's degree was concerned with the yielding of aluminium alloy when subjected to both tensile and torsional loading. He joined the Aeronautical Research Laboratories (now called the Aeronautical and Maritime Research Laboratory) in 1970 and has worked on a wide range of research projects, including the prediction of the performance of gas turbine engines under conditions of pulsating flow, parametric studies of ramrocket performance, flow instability in aircraft intakes and problems associated with the landing of a helicopter on the flight deck of a ship. Concurrently with some of the above work, he studied at the University of Melbourne and in 1988 obtained his Doctor of Philosophy degree for work on low-Reynolds-number turbulent boundary layers. Lincoln is currently employed as a Research Scientist and is undertaking research investigations in the low-speed wind tunnel and the water tunnel.*

---

# Contents

<b>1. INTRODUCTION.....</b>	<b>1</b>
<b>2. MEAN-VELOCITY MEASUREMENTS.....</b>	<b>3</b>
2.1 Test Schedule.....	3
2.2 Procedure Used to Measure Reference Free-Stream Velocities .....	5
2.3 Cross-Tunnel Rake .....	5
2.4 Procedure Used to Measure Mean Velocities.....	5
2.5 Analysis of Mean Velocities.....	9
2.5.1 Analysis With Respect to Each Cross Section .....	9
2.5.2 Analysis With Respect to the Central Cross Section.....	14
2.5.3 Longitudinal Velocity Variation.....	14
2.5.4 Effect of Change in Nominal Free-Stream Velocity .....	15
2.5.5 Effect of Probe Misalignment With Respect to the Flow.....	15
2.6 Errors in Measured Mean Velocities .....	15
<b>3. FLOW-ANGLE MEASUREMENTS.....</b>	<b>24</b>
3.1 Test Schedule.....	24
3.2 Six-Hole Probe.....	24
3.3 Transformation of Coordinates .....	27
3.4 Traversing Mechanism.....	28
3.5 Procedure Used to Measure Flow Angles .....	34
3.6 Corrections to Flow Angles to Allow for Probe Support Interference .....	35
3.7 Analysis of Flow Angles.....	38
3.8 Errors in Measured Flow Angles.....	39
3.8.1 Instrumentation Errors .....	39
3.8.2 Probe Setup Errors.....	39
3.8.3 Accumulation of Errors .....	46
<b>4. TURBULENCE-INTENSITY MEASUREMENTS.....</b>	<b>46</b>
4.1 Test Schedule.....	46
4.2 Modified Cross-Tunnel Rake.....	46
4.3 Procedure Used to Measure Turbulence Intensities.....	48
4.4 Analysis of Turbulence Intensities.....	49
4.5 Errors in Measured Turbulence Intensities .....	58
4.6 Turbulence Signals and Mean-Velocity Variations.....	58
<b>5. SPECTRAL MEASUREMENTS.....</b>	<b>59</b>
5.1 Test Schedule.....	59
5.2 Procedure Used to Measure Spectra.....	59
5.3 Analysis of Spectra.....	64
<b>6. ASSESSMENT OF FLOW QUALITY IN THE LSWT.....</b>	<b>72</b>
6.1 Mean Velocities .....	72
6.2 Flow Angles.....	72
6.3 Turbulence Intensities and Spectra.....	73
6.4 Adequacy of Flow Quality in the LSWT.....	73
<b>7. POSSIBLE CAUSES OF FLOW NON UNIFORMITIES AND POSSIBLE     METHODS FOR IMPROVING THE FLOW .....</b>	<b>74</b>

<b>8. CONCLUDING REMARKS.....</b>	<b>77</b>
<b>9. ACKNOWLEDGEMENTS.....</b>	<b>78</b>
<b>10. REFERENCES.....</b>	<b>79</b>

## Notation

$C_{P_n}$	Pressure coefficients associated with the six-hole probe, $C_{P_n} = (p_n - p_{ref}) / (0.5 \rho V_y^2)$ , ( $n = 1$ to $6$ ).
$f$	Frequency, (Hz).
$H$	Height of the test section of the low-speed wind tunnel, ( $H = 2134$ mm).
$M$	Molecular weight of air ( $M = 28.9644$ ), (dimensionless).
$p_{cu}, p_{cd}$	Static pressures at the upstream and downstream ends respectively of the tunnel contraction, (Pa).
$p_{ref}$	Reference pressure (Pa).
$p_1, p_2, p_3 \dots$	Pressures associated with the six-hole probe or the cross-tunnel rake (pressures are not necessarily total or static), (Pa).
$R^*$	Universal gas constant ( $R^* = 8314.32$ J/[K.kg Mol]).
$S_u, S_v, S_w$	Normalized power spectral densities for the $u$ , $v$ and $w$ components of the turbulence respectively, (dimensionless).
$t$	Static temperature of the air in the test section, (K).
$u$	Fluctuating component of velocity in the $x_T$ direction, (m/s).
$U$	Velocity in the $x_T$ direction ( $U = \bar{U} + u$ ), (m/s).
$\bar{U}$	Mean velocity in the $x_T$ direction, (m/s).
$\bar{U}_B$	Mean velocity in the $x_B$ direction in the probe body coordinate system, (m/s)
$\bar{U}_{NOM}$	Nominal free-stream velocity in the $x_T$ direction, (m/s).
$\bar{U}_{REF}$	Reference free-stream velocity at the "centre" of the test section, (m/s).
$\bar{U}_T$	Mean velocity in the $x_T$ direction in the tunnel coordinate system, (m/s).
$\bar{U}_{-1.0}$	Mean velocity in the $x_T$ direction at the location where $x_T = -1.0$ m, $y_T = 0.0$ m and $z_T = 0.0$ m, (m/s).
$\bar{U}_{0.0}$	Mean velocity in the $x_T$ direction at the location where $x_T = 0.0$ m, $y_T = 0.0$ m and $z_T = 0.0$ m, (m/s).
$\bar{U}_{1.0}$	Mean velocity in the $x_T$ direction at the location where $x_T = 1.0$ m, $y_T = 0.0$ m and $z_T = 0.0$ m, (m/s).
$v$	Fluctuating component of velocity in the $y_T$ direction, (m/s).
$\bar{V}_B$	Mean velocity in the $y_B$ direction in the probe body coordinate system, (m/s)
$\bar{V}_T$	Mean velocity in the $y_T$ direction in the tunnel coordinate system, (m/s).
$V_y$	Velocity vector as measured with the six-hole probe (yawmeter) (Figure 16), (m/s).
$w$	Fluctuating component of velocity in the $z_T$ direction, (m/s).

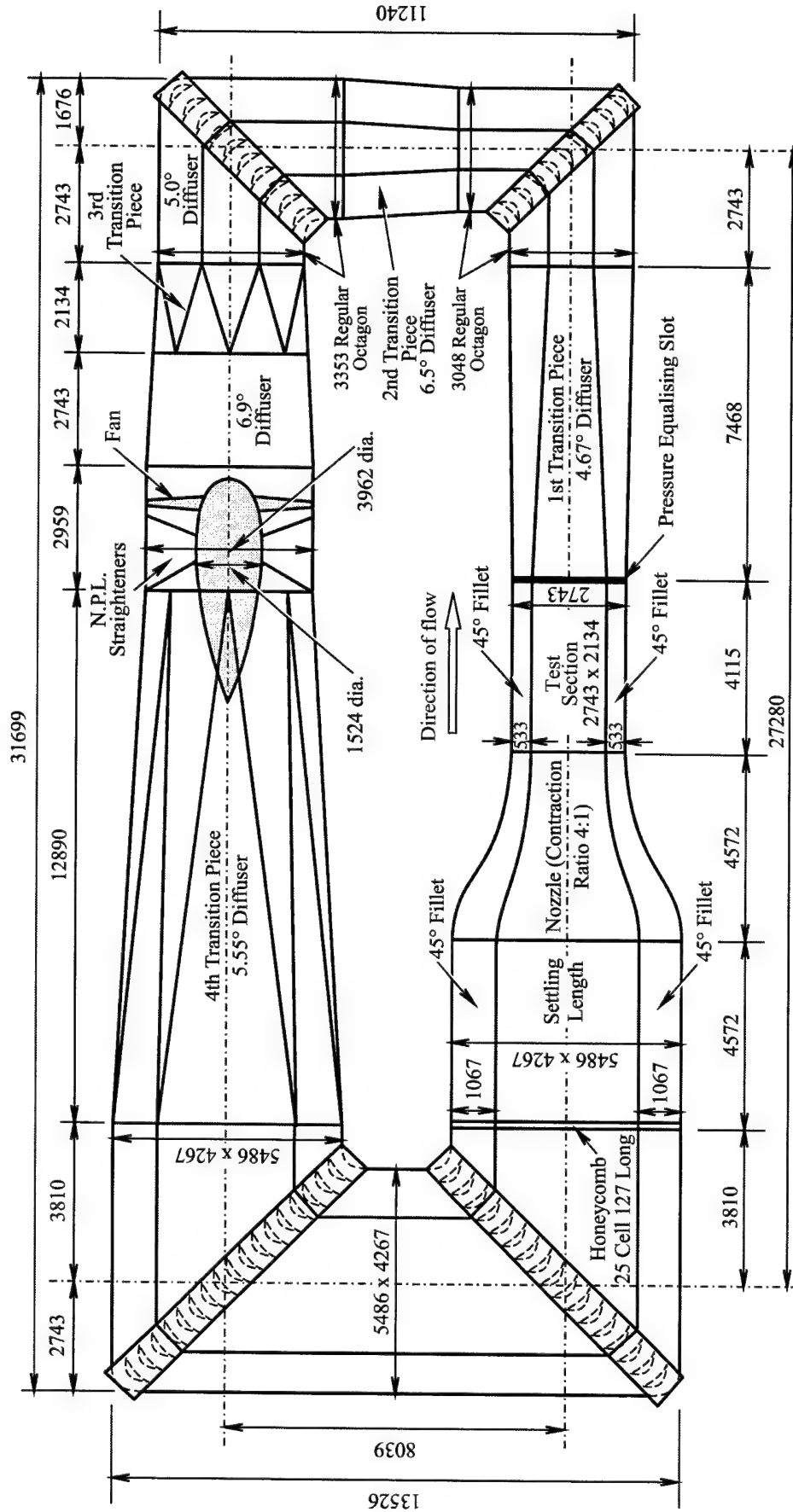
$W$	Width of the test section of the low-speed wind tunnel, ( $W = 2743$ mm).
$\overline{W}_B$	Mean velocity in the $z_B$ direction in the probe body coordinate system, (m/s)
$\overline{W}_T$	Mean velocity in the $z_T$ direction in the tunnel coordinate system, (m/s).
$x_B, y_B, z_B$	Body coordinate system (right-handed) for the six-hole probe (Figure 16). The origin is located at centre of the hemisphere which forms the tip of the probe. The $x_B$ axis is along the probe longitudinal axis, the $y_B$ axis is in the plane passing through holes 2, 4 and 5 and the $z_B$ axis is in the plane passing through holes 1, 3 and 5. The axes remain fixed with respect to the probe.
$x_B, y_B, z_B$	Directions or distances in the probe body coordinate system (Figure 16), (m)
$x_T, y_T, z_T$	Tunnel coordinate system (right-handed) (Figure 2). The origin is located at the midpoint of the line joining the centres of the lower and upper turntables in the test section. The $x_T$ axis is on the test section longitudinal centreline and is positive in the downstream direction, the $y_T$ axis is horizontal and is positive to port and the $z_T$ axis is positive vertically downwards. The axes remain fixed with respect to the tunnel.
$x_T, y_T, z_T$	Directions or distances in the tunnel coordinate system (Figure 2), (m).
$\epsilon_H$	Horizontal flow angle in the tunnel coordinate system (Figure 21), (deg).
$\epsilon_V$	Vertical flow angle in the tunnel coordinate system (Figure 21), (deg).
$\theta$	Pitch angle for the six-hole probe, relative to the tunnel coordinate system, $x_T, y_T, z_T$ (Figure 16), (deg).
$\theta_Y$	Flow angle as measured with the six-hole probe (yawmeter) (Figure 16), (deg).
$[\lambda]_{BT}$	Matrix of direction cosines used to transform velocities from the tunnel coordinate system to the probe body coordinate system.
$[\lambda]_{TB}$	Matrix of direction cosines used to transform velocities from the probe body coordinate system to the tunnel coordinate system.
$\rho$	Density of the air in the test section, ( $\text{kg/m}^3$ ).
$\phi$	Roll angle for the six-hole probe, relative to the tunnel coordinate system, $x_T, y_T, z_T$ (Figure 16), (deg).
$\phi_Y$	Flow angle as measured with the six-hole probe (yawmeter) (Figure 16), (deg).
$\psi$	Yaw angle for the six-hole probe, relative to the tunnel coordinate system, $x_T, y_T, z_T$ (Figure 16), (deg).

## 1. Introduction

The low-speed wind tunnel (LSWT) at the Aeronautical and Maritime Research Laboratory (AMRL) was designed in 1939 and commissioned in 1941. It has a closed return circuit with an octagonal test section 2.74 m wide and 2.13 m high, as shown in Figure 1 (Reference 1). The circuit remained essentially unchanged from 1941 until 1996, when the length of the test section was increased, enabling longer models to be tested, and a redesigned contraction was installed. Within the constraints imposed by the space available in the existing settling chamber and the new contraction design, the length of the test section was increased from 4.12 m to 6.56 m. The tunnel is driven by electric motors with a combined output of 0.75 MW and the maximum velocity obtainable in the test section is about 100 m/s. At the downstream end of the test section there is a pressure equalizing slot which maintains the test section at near atmospheric pressure.

Ideally, the flow in the test section of a wind tunnel is uniform throughout, is parallel to the tunnel walls (for parallel-walled tunnels) and has zero turbulence. However, the flow is never perfect and it is necessary to calibrate the flow to determine the extent of the irregularities. To calibrate the flow in a tunnel, detailed flow measurements are taken throughout the empty test section to see how the flow deviates from location to location. The calibration enables it to be estimated if corrections should be made to test results, e.g. corrections may have to be made to measurements if the angle of the flow incident on one wing of an aircraft is slightly different from that on the other wing. The calibration also indicates what adjustments have to be made to the orientation of a model when testing, e.g. the flow may have some angularity so that a strain-gauge balance in a model may need to be aligned with the flow rather than the axes of the tunnel. A calibration enables an assessment to be made of the suitability of a tunnel for a given project, e.g. a tunnel having a high free-stream turbulence intensity may be unsuitable for fundamental experiments in which boundary-layer transition is important, since high turbulence levels can significantly affect the characteristics of the flow being studied. A calibration establishes the limitations of the tunnel.

In the mid 1940s, a limited number of measurements were taken in the LSWT to determine mean-velocity distributions across the test section (Reference 1) as well as turbulence intensities at a few locations (unpublished), but these early measurements were very limited. There have been some changes to the tunnel since that time. In the early 1960s, the complete air-flow propulsion system, i.e. the fan, fairing, straightening vanes, controller and motor, was redesigned and replaced. The original fan had 6 wooden blades and there were 7 straightening vanes in the fan assembly. The new fan has 8 blades made from foam covered with fibreglass and there are 7 new straightening vanes. In 1984, the 9 turning vanes at the first corner were replaced with 22 new ones of a different aerodynamic shape. This was done to provide some cooling of the air by pumping chilled water through the centres of the vanes. At this time, the catch screen at the leading edge of the original vanes was also moved about 5 m upstream to a position



All dimensions in mm

Figure 1. Diagrammatic representation of the low-speed wind tunnel at AMRL (based on a diagram given in Reference 1).

about 4.9 m downstream of the test section. Although no comparative measurements were made, it is unlikely that these modifications had a significant effect on the quality of the flow in the test section. In 1983, some calibration data were taken for a specific purpose (Reference 2), but a thorough calibration has never been carried out. Prior to the current work, no measurements had ever been taken to determine how flow angles or spectra varied throughout the test section.

A comprehensive calibration of the flow in the test section of the tunnel with the original contraction was carried out not long before the extended test section and new contraction were installed in 1996. Details of the calibration are given in this report. The calibration was performed to: (1) provide a data base of the flow quality for tests carried out up until 1996 and (2) provide a basis on which to assess the effectiveness of the new contraction and extended test section. An extensive range of longitudinal mean-flow velocities, flow angles, turbulence intensities and turbulence spectra were measured. Data were taken at up to 155 grid points across the flow at each of three longitudinal distances of -1.0, 0.0 and 1.0 m from the datum of the tunnel coordinate system (see Section 2.1) and for nominal free-stream velocities of 30, 45, 60 and 75 m/s. The calibration data are presented and analysed and possible explanations of flow behaviour are given.

Fitting the extended test section and new contraction in 1996 was the first step in an attempt to improve the quality of the flow in the test section. The quality of the flow with the extended test section and new contraction in place will be measured and reported at a later date. Depending on the results, further modifications to the tunnel may be made, which could include fitting a redesigned honeycomb and installing screens (currently the tunnel has no screens). However fitting screens would have the disadvantage of reducing the maximum velocity in the test section.

## 2. Mean-Velocity Measurements

### 2.1 Test Schedule

Longitudinal mean velocities,  $\bar{U}$ , were measured in the test section of the tunnel at the 155 grid points shown in Figure 2 for each of three longitudinal positions,  $x_T$  (see below), of -1.0, 0.0 and 1.0 m and for nominal free-stream velocities,  $\bar{U}_{\text{NOM}}$ , of 30, 45, 60 and 75 m/s.

The origin of the tunnel coordinate system,  $x_T y_T z_T$ , shown in Figure 2, is located at the midpoint of the line joining the centres of the concentric lower and upper turntables in the test section. The  $x_T$  axis is on the test section longitudinal centreline and is positive in the downstream direction, the  $y_T$  axis is horizontal and is positive to the port side of



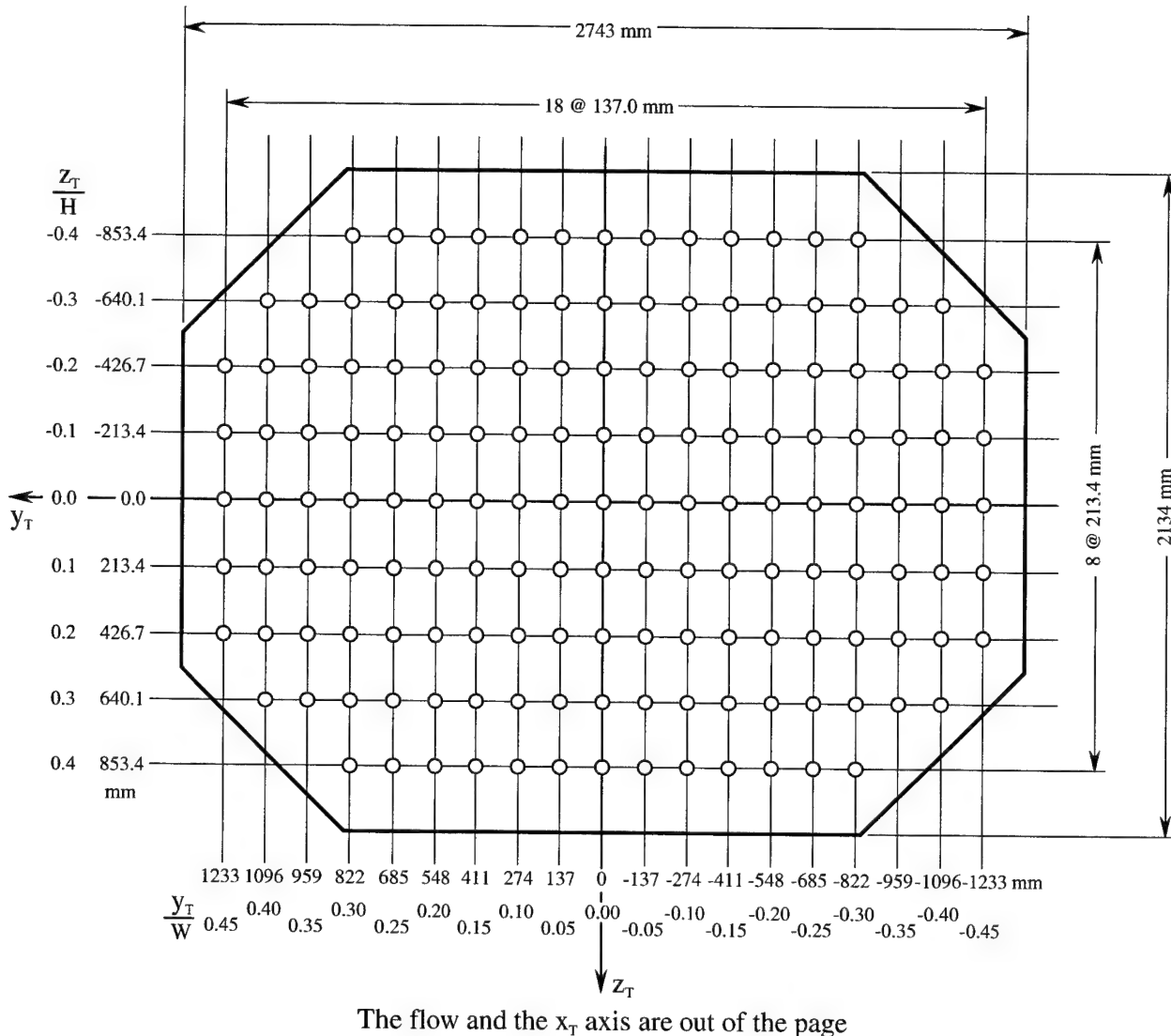


Figure 2. Grid points, shown circled, at which mean velocities and flow angles were measured.

the tunnel and the  $z_T$  axis is positive vertically downwards. The axes form a right-handed coordinate system and remain fixed with respect to the tunnel.

In Figure 2, the grid points are spaced at intervals of 137.0 mm in the  $y_T$  direction, corresponding to the spacing of the pressure probes on the cross-tunnel rake (Section 2.3), and at intervals of 213.4 mm in the  $z_T$  direction. The  $y_T$  spacing corresponds to 1/20th of the width of the octagonal test section and the  $z_T$  spacing corresponds to 1/10th of the height of the test section ( $W = 2.743$  m and  $H = 2.134$  m).

## 2.2 Procedure Used to Measure Reference Free-Stream Velocities

Reference free-stream velocities at the “centre” of the test section of the tunnel were set using the static pressures,  $p_{cu}$  and  $p_{cd}$ , at the upstream and downstream ends respectively of the tunnel contraction. The contraction had been calibrated previously (unpublished) and it was determined that

$$\bar{U}_{REF} = \left[ \frac{1.04 \times 2(p_{cu} - p_{cd})}{\rho} \right]^{0.5} \quad (1)$$

The empirical factor of 1.04 was the calibration factor for the LSWT that had been determined and used prior to the current measurements. The density of the air in the test section,  $\rho$ , is given by (Reference 3)

$$\rho = \frac{M p_{cd}}{R^* t} \quad (2)$$

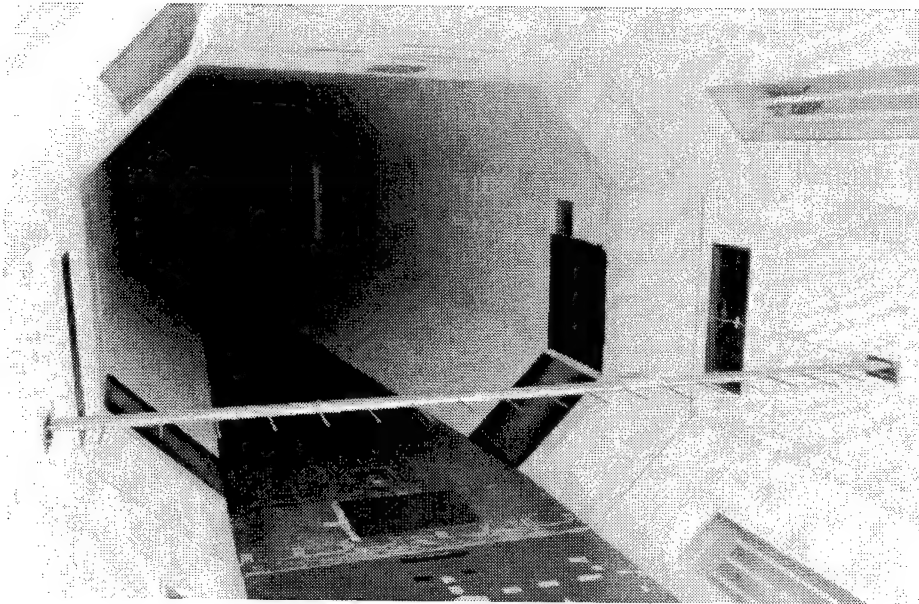
$M$  is the molecular weight of air ( $M = 28.9644$  [dimensionless]),  $R^*$  is the universal gas constant ( $R^* = 8314.32$  J/[K.kg Mol]) and  $t$  is the static temperature of the air in the test section. Equation 1 was used to set the reference free-stream velocity in the test section when the detailed calibration measurements were taken.

## 2.3 Cross-Tunnel Rake

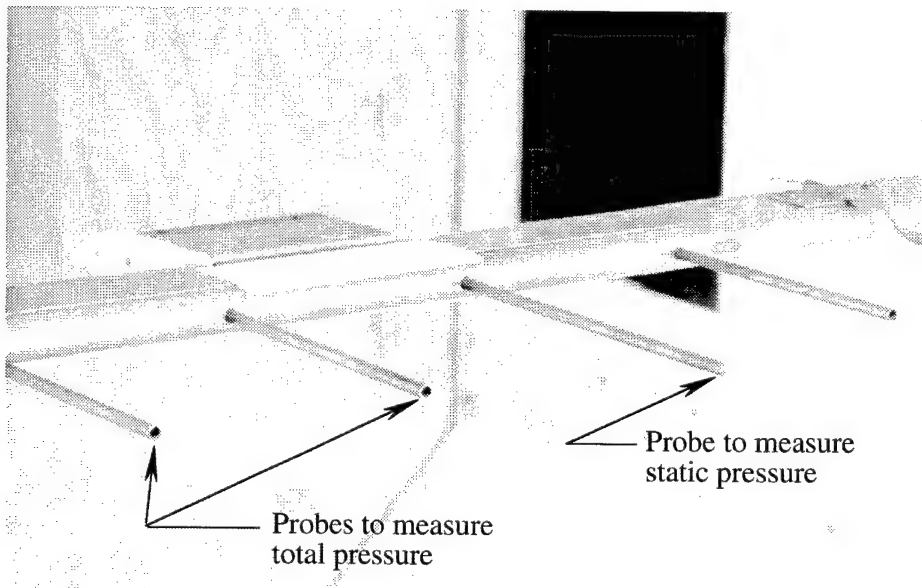
The cross-tunnel rake shown in Figures 3 and 4 was used to measure pressures at the different grid points shown in Figure 2. The rake is made up of a number of sections bolted together and contains 15 total-pressure probes and 4 static-pressure probes, arranged as shown (Figure 4). The total-pressure probes have outer and inner diameters of 6.35 and 4.93 mm respectively and the static-pressure probes have outer diameters of 6.35 mm. For  $z_r/H$  locations of 0.0,  $\pm 0.1$  and  $\pm 0.2$  (Figure 2), the rake contained probes 1 to 19 (Figure 4) and was bolted to the side walls of the test section using mounting brackets. To allow for the corner fillets in the octagonal test section, the length of the rake could be altered by using different end sections which contained probes. For  $z_r/H = \pm 0.3$ , the rake contained probes 2 to 18 and for  $z_r/H = \pm 0.4$ , the rake contained probes 4 to 16. When the rake was shortened, supporting stands were attached to the rake so that it could be bolted to the floor or the roof of the test section.

## 2.4 Procedure Used to Measure Mean Velocities

Longitudinal mean velocities at different grid points were measured using the pressure probes on the cross-tunnel rake. Pressures were measured using a Pressure Systems Incorporated (PSI) 8400 Electronic Measurement System, configured with a single 32



(a) rake mounted in the test section



(b) details of the pressure probes and the enclosure containing the pressure scanner

Figure 3. Cross-tunnel rake.

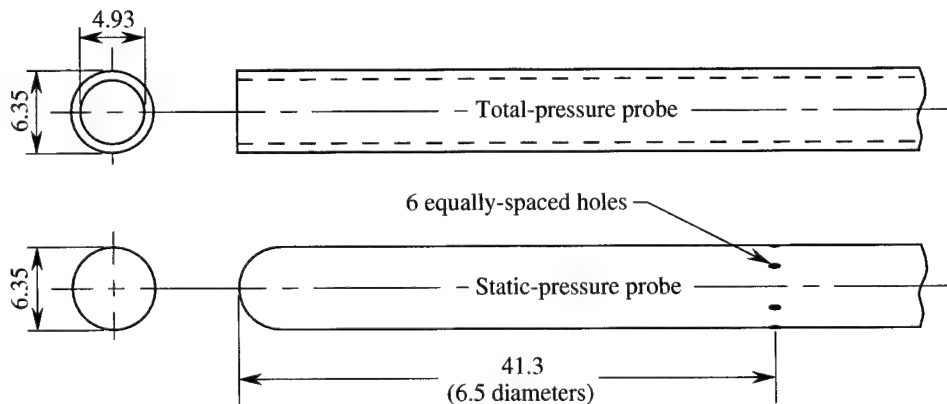
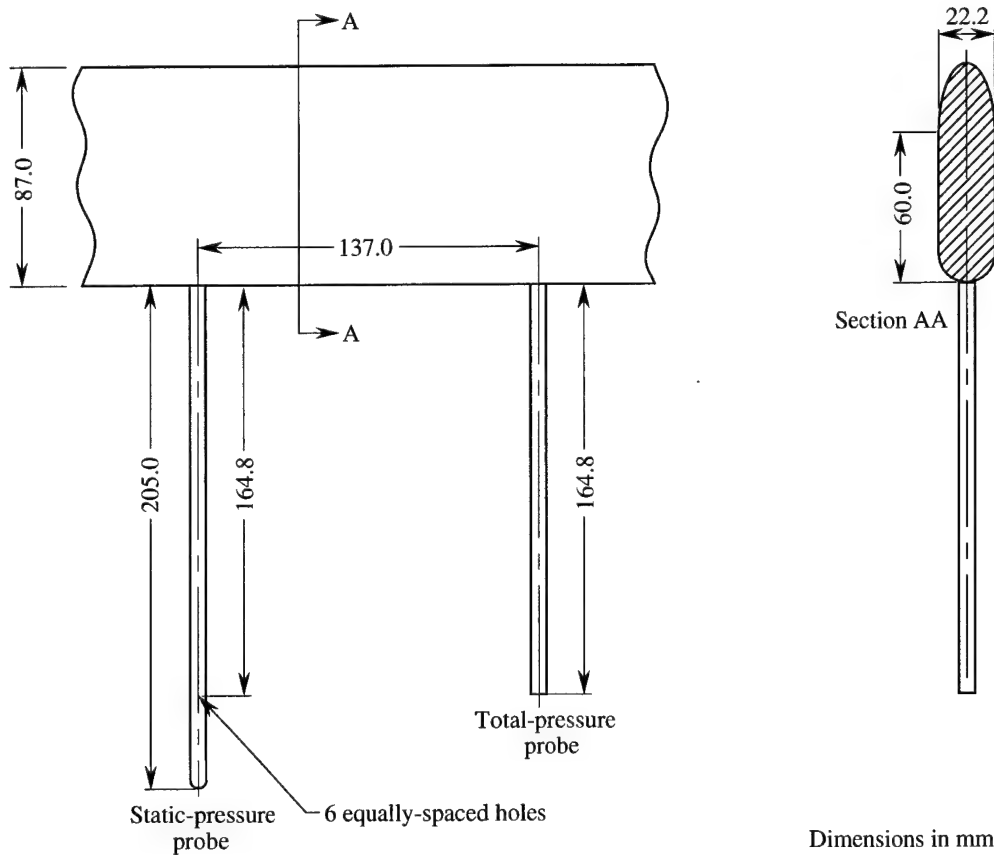
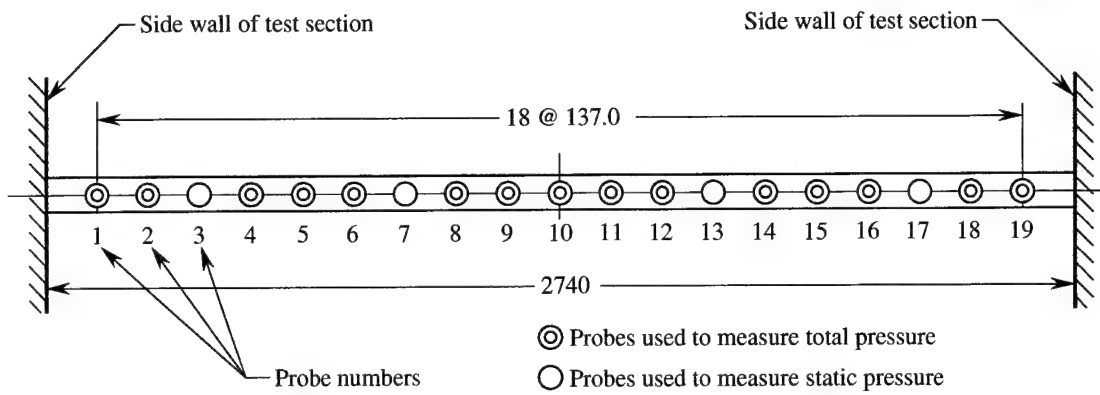


Figure 4. Cross-tunnel rake used to measure mean-flow velocities showing diagrammatic representation of rake (top), cross section of rake (middle) and details of probes (bottom).

port Electronic Pressure Scanner having a range of  $\pm 6895$  Pa ( $\pm 1.0$  psi) and capable of measuring 32 differential pressures<sup>1</sup>. Software used to control and operate the system is located on a PC. The features of the system are described in References 4 and 5.

The total and static pressure ports on the probes on the rake, as well as the static pressure ports in the upstream and downstream ends of the contraction, used when measuring  $p_{cu}$  and  $p_{cd}$  respectively, were connected to ports on the scanner, and all ports were referenced to  $p_{cd}$ . Prior to any given run, the pressure transducers in the scanner were calibrated over the range of pressures likely to be encountered during subsequent measurements. Four different ranges of pressures were used, corresponding to nominal free-stream velocities of 30, 45, 60 and 75 m/s. The accuracy of the calibration was verified by checking that all measured differential pressures were close to zero, as observed graphically on a monitor, when there was no flow in the tunnel.

The software allowed the user to specify sampling controls when acquiring data. The differential pressures corresponding to each of the ports were sampled 50 times at intervals of 65 000  $\mu$ s and then average pressures for each port were calculated and recorded. The 65 000  $\mu$ s interval was the maximum allowable with the system and corresponds to a sampling frequency of 15.4 Hz. The total sampling time for the 50 samples was about 3.2 s. By setting the sampling frequency at the lowest possible value allowed by the equipment, any large scale, slowly varying, pressure oscillations in the tunnel were more likely to be averaged. The above sampling was repeated 10 times with a 5 s time delay between sampling each data set. The differential pressures corresponding to each of the ports were then averaged for the 10 sets of data to obtain overall averages, each of which corresponds to  $50 \times 10 = 500$  individual samples.

As can be seen from Figure 4, the arrangement of the probes on the rake meant that either the total pressure or the static pressure was measured at each grid point. Since it was necessary to know both the static and the total pressure at a given point to calculate the velocity at that point, approximations had to be made when calculating velocities. When calculating velocities at grid points where total pressures were known, nearby static pressures were used. For example, the velocity at point 4 was based upon  $p_4$  (total pressure),  $p_3$  (static pressure) and  $p_7$  (static pressure). A mean velocity denoted by  $\bar{U}_{4A}$  was computed using

$$\bar{U}_{4A} = \left[ \frac{2(p_4 - p_3)}{\rho} \right]^{0.5} \quad (3)$$

and a mean velocity denoted by  $\bar{U}_{4B}$  was computed using

$$\bar{U}_{4B} = \left[ \frac{2(p_4 - p_7)}{\rho} \right]^{0.5} \quad (4)$$

---

<sup>1</sup> Pressure Systems Incorporated, 34 Research Drive, Hampton, VA, 23666, USA.

The mean velocity  $\bar{U}_4$  at position 4 was then determined from  $\bar{U}_{4A}$  and  $\bar{U}_{4B}$  using linear interpolation as follows

$$\bar{U}_4 = 0.75 [\bar{U}_{4A}] + 0.25 [\bar{U}_{4B}] \quad (5)$$

At grid points where static pressures were known, mean velocities were determined using linear interpolation of the calculated adjoining velocities. For example, the mean velocity at point 3 was determined from  $\bar{U}_2$  and  $\bar{U}_4$  using linear interpolation as follows

$$\bar{U}_3 = 0.5 [\bar{U}_2 + \bar{U}_4] \quad (6)$$

The reference free-stream velocity,  $\bar{U}_{REF}$ , determined using equation 1, varied slightly for the different positions of the cross-tunnel rake, due to the practical difficulties of a tunnel operator setting the free-stream velocity at precisely the same value for the different rake positions. To obtain a consistent set of values of  $\bar{U}$  measured with the rake, the values of  $\bar{U}$  were non-dimensionalised with respect to the appropriate value of  $\bar{U}_{REF}$ . To obtain a consistent set of results with respect to a given location in the tunnel, for example at the centre of the test section where  $x_T = 0.0$ ,  $y_T = 0.0$  and  $z_T = 0.0$  m, the results were then normalized with respect to the  $\bar{U}/\bar{U}_{REF}$  ratio at this point.

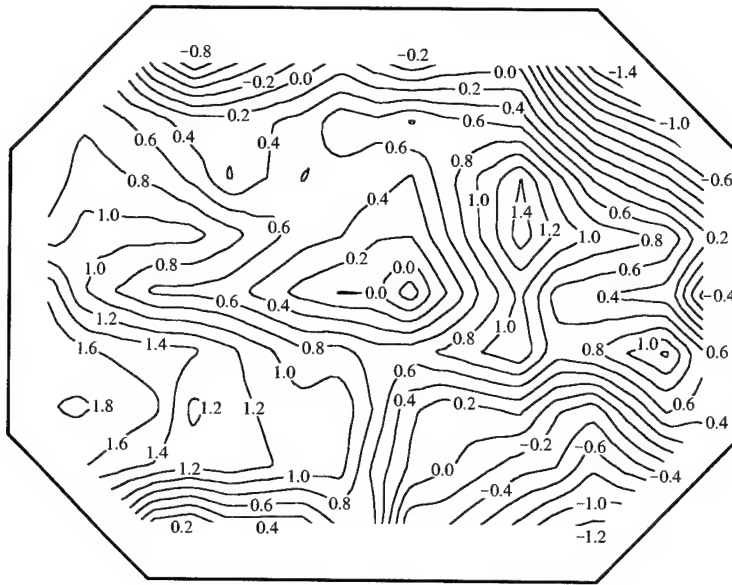
## 2.5 Analysis of Mean Velocities

Longitudinal mean velocities are presented as contours of  $(\bar{U} - \bar{U}_{-1.0})/\bar{U}_{-1.0}$ ,  $(\bar{U} - \bar{U}_{0.0})/\bar{U}_{0.0}$  and  $(\bar{U} - \bar{U}_{1.0})/\bar{U}_{1.0}$  (expressed as a percentage) for different values of  $x_T$  and  $\bar{U}_{NOM}$ .  $\bar{U}_{-1.0}$ ,  $\bar{U}_{0.0}$  and  $\bar{U}_{1.0}$  are the mean velocities in the  $x_T$  direction on the tunnel longitudinal centreline ( $y_T = 0.0$  m and  $z_T = 0.0$  m) at the locations where  $x_T = -1.0$ ,  $0.0$  and  $1.0$  m respectively. Contour plots of mean velocities, as well as contour plots of flow angles and turbulence intensities, are presented with the direction of the flow out of the page.

The most important area of the test section, where models are usually located, is the region comprising approximately the central 0.7 of the width and 0.7 of the height, i.e. approximately the central 50% of the cross-sectional area of the test section. Discussion on the variation of mean velocities, as well as on flow angles and turbulence intensities, will mainly apply to these central regions of flow cross sections.

### 2.5.1 Analysis With Respect to Each Cross Section

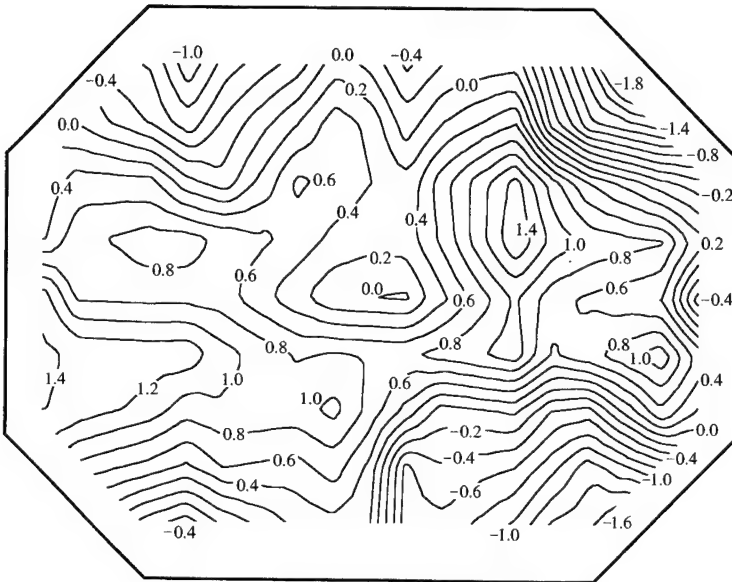
Contours of  $(\bar{U} - \bar{U}_{-1.0})/\bar{U}_{-1.0}$  for  $x_T = -1.0$  m,  $(\bar{U} - \bar{U}_{0.0})/\bar{U}_{0.0}$  for  $x_T = 0.0$  m and  $(\bar{U} - \bar{U}_{1.0})/\bar{U}_{1.0}$  for  $x_T = 1.0$  m, all for  $\bar{U}_{NOM} = 30$  m/s, are shown in Figure 5. Corresponding plots for  $\bar{U}_{NOM} = 45$ ,  $60$  and  $75$  m/s are shown in Figures 6, 7 and 8 respectively. For each of the 12 sets of contours shown in Figures 5 to 8, the



$$\frac{\bar{U} - \bar{U}_{-1.0}}{\bar{U}_{-1.0}} \%$$

$$\bar{U}_{\text{NOM}} = 30 \text{ m/s}$$

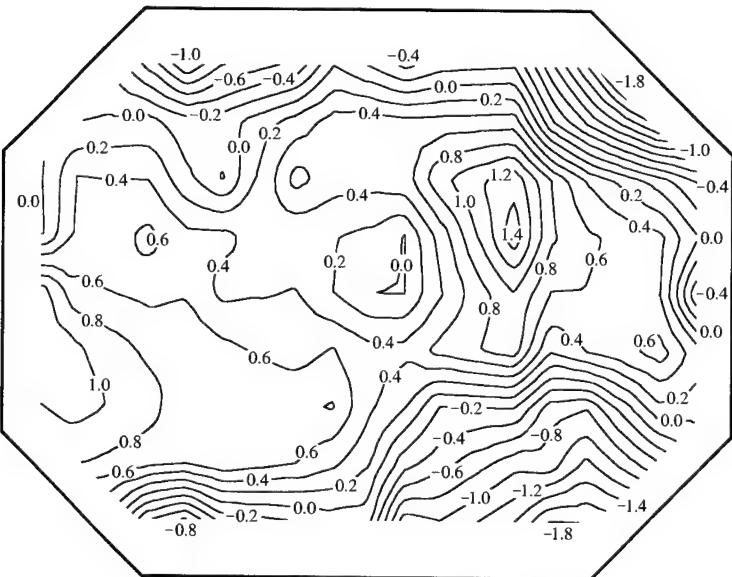
$$x_T = -1.0 \text{ m}$$



$$\frac{\bar{U} - \bar{U}_{0.0}}{\bar{U}_{0.0}} \%$$

$$\bar{U}_{\text{NOM}} = 30 \text{ m/s}$$

$$x_T = 0.0 \text{ m}$$



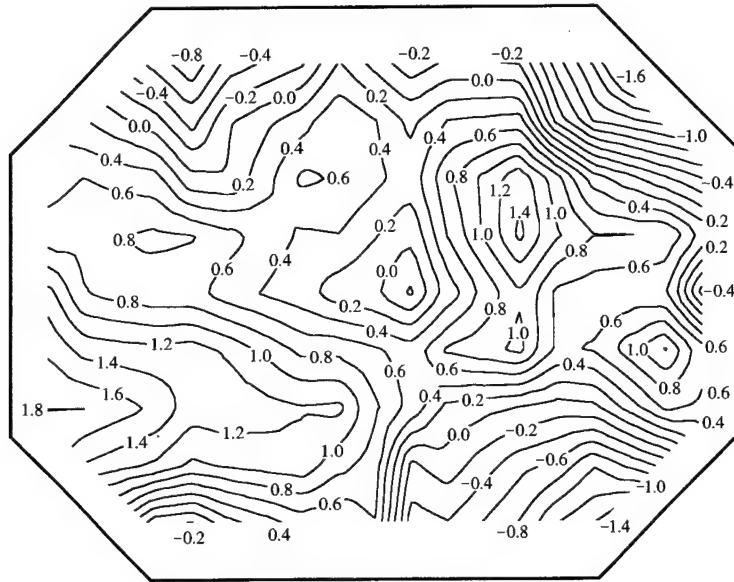
$$\frac{\bar{U} - \bar{U}_{1.0}}{\bar{U}_{1.0}} \%$$

$$\bar{U}_{\text{NOM}} = 30 \text{ m/s}$$

$$x_T = 1.0 \text{ m}$$

Figure 5. Contours of velocity deviation for  $\bar{U}_{\text{NOM}} = 30 \text{ m/s}$  for  $x_T = -1.0, 0.0$  and  $1.0 \text{ m}$ .

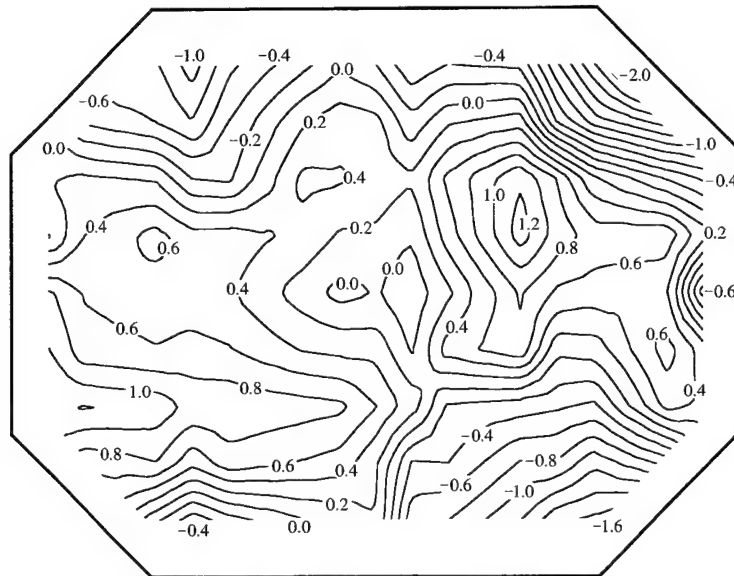
The flow is out of the page.



$$\frac{\bar{U} - \bar{U}_{-1.0}}{\bar{U}_{-1.0}} \%$$

$$\bar{U}_{\text{NOM}} = 45 \text{ m/s}$$

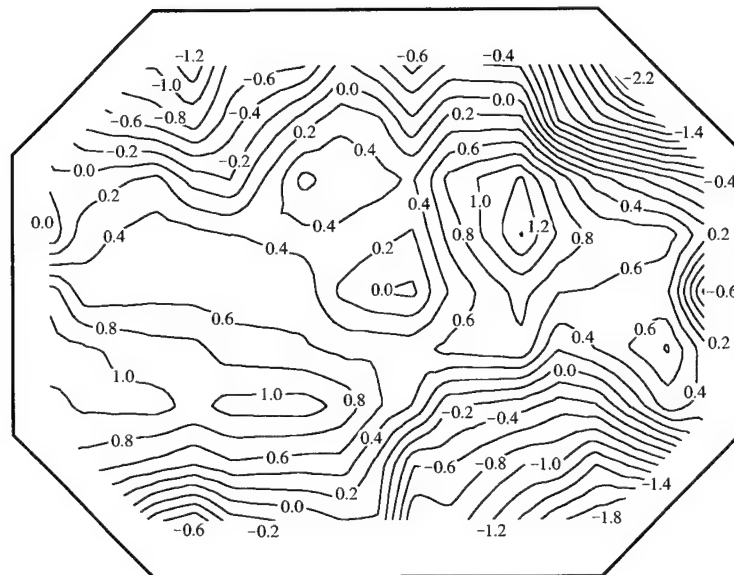
$$x_T = -1.0 \text{ m}$$



$$\frac{\bar{U} - \bar{U}_{0.0}}{\bar{U}_{0.0}} \%$$

$$\bar{U}_{\text{NOM}} = 45 \text{ m/s}$$

$$x_T = 0.0 \text{ m}$$



$$\frac{\bar{U} - \bar{U}_{1.0}}{\bar{U}_{1.0}} \%$$

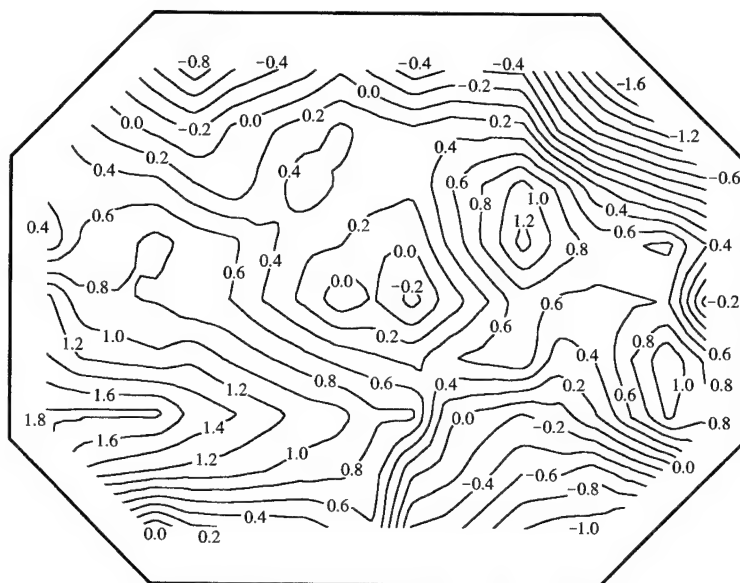
$$\bar{U}_{\text{NOM}} = 45 \text{ m/s}$$

$$x_T = 1.0 \text{ m}$$

Figure 6. Contours of velocity deviation for  $\bar{U}_{\text{NOM}} = 45 \text{ m/s}$  for  $x_T = -1.0, 0.0$  and  $1.0 \text{ m}$ .

The flow is out of the page.

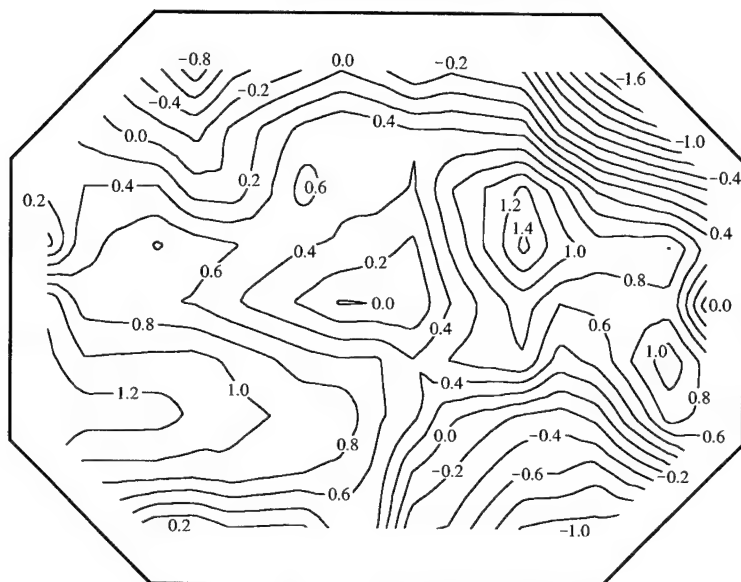




$$\frac{\bar{U} - \bar{U}_{-1.0}}{\bar{U}_{-1.0}} \%$$

$$\bar{U}_{\text{NOM}} = 60 \text{ m/s}$$

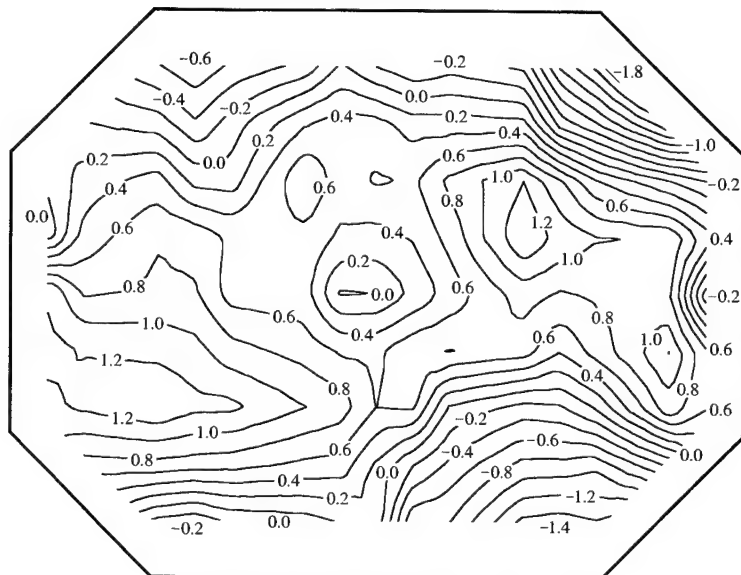
$$x_T = -1.0 \text{ m}$$



$$\frac{\bar{U} - \bar{U}_{0.0}}{\bar{U}_{0.0}} \%$$

$$\bar{U}_{\text{NOM}} = 60 \text{ m/s}$$

$$x_T = 0.0 \text{ m}$$



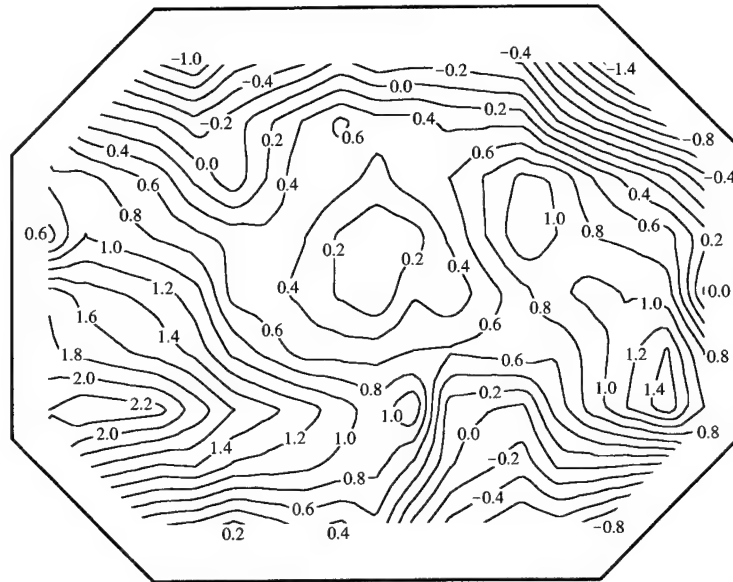
$$\frac{\bar{U} - \bar{U}_{1.0}}{\bar{U}_{1.0}} \%$$

$$\bar{U}_{\text{NOM}} = 60 \text{ m/s}$$

$$x_T = 1.0 \text{ m}$$

Figure 7. Contours of velocity deviation for  $\bar{U}_{\text{NOM}} = 60 \text{ m/s}$  for  $x_T = -1.0, 0.0$  and  $1.0 \text{ m}$ .

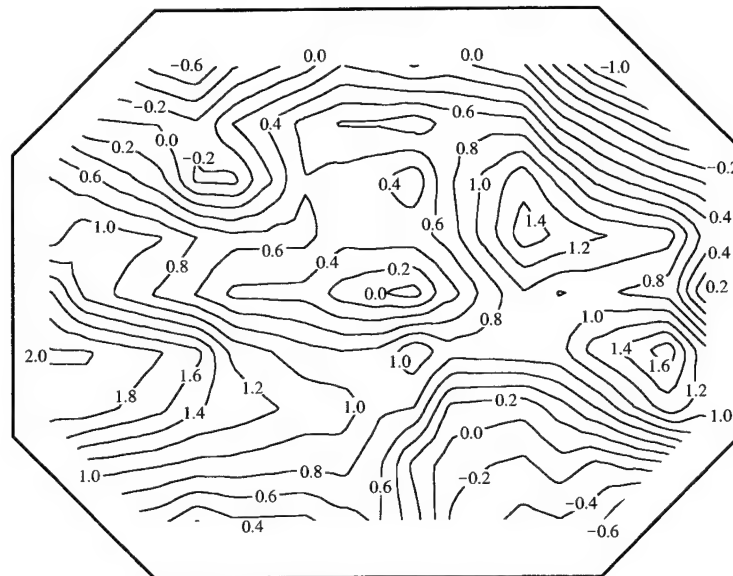
The flow is out of the page.



$$\frac{\bar{U} - \bar{U}_{-1.0}}{\bar{U}_{-1.0}} \%$$

$$\bar{U}_{\text{NOM}} = 75 \text{ m/s}$$

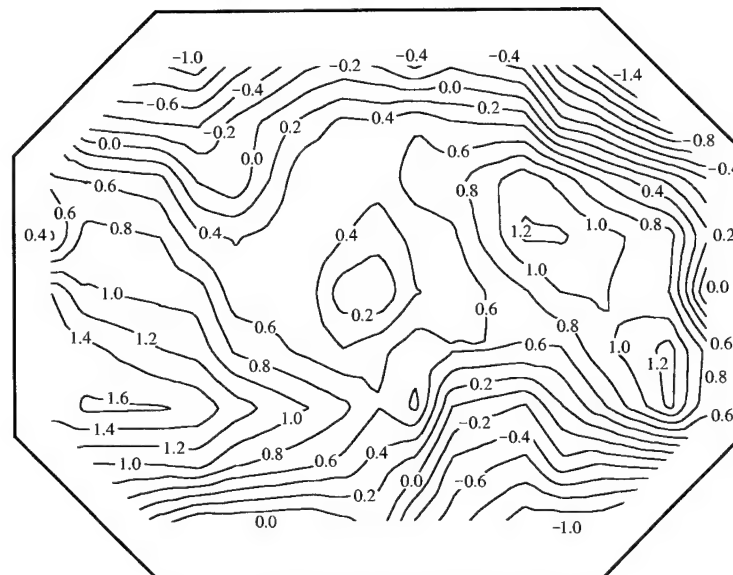
$$x_T = -1.0 \text{ m}$$



$$\frac{\bar{U} - \bar{U}_{0.0}}{\bar{U}_{0.0}} \%$$

$$\bar{U}_{\text{NOM}} = 75 \text{ m/s}$$

$$x_T = 0.0 \text{ m}$$



$$\frac{\bar{U} - \bar{U}_{1.0}}{\bar{U}_{1.0}} \%$$

$$\bar{U}_{\text{NOM}} = 75 \text{ m/s}$$

$$x_T = 1.0 \text{ m}$$

Figure 8. Contours of velocity deviation for  $\bar{U}_{\text{NOM}} = 75 \text{ m/s}$  for  $x_T = -1.0, 0.0$  and  $1.0 \text{ m}$ .

The flow is out of the page.

normalizing velocity, i.e.  $\bar{U}_{-1.0}$ ,  $\bar{U}_{0.0}$  or  $\bar{U}_{1.0}$ , is associated with the  $x_T$  location of the contours, i.e.  $\bar{U}_{-1.0}$  is used for contours at  $x_T = -1.0$  m, and likewise for  $\bar{U}_{0.0}$  and  $\bar{U}_{1.0}$ . For each of the four values of  $\bar{U}_{\text{NOM}}$ , the general pattern of the contours at the three  $x_T$  locations is similar, with little evidence of the flow becoming more uniform as it moves downstream. Regions of high or low mean velocity are simply convected downstream with little transverse movement, indicating that there are no large-scale swirls in the test section. For  $\bar{U}_{\text{NOM}} = 30$  m/s, for  $x_T = -1.0, 0.0$  and  $1.0$  m, longitudinal mean-flow velocities typically deviated between  $-0.6\%$  and  $+1.4\%$  from their values at the centre of each tunnel cross section (Figure 5). Corresponding deviations for  $\bar{U}_{\text{NOM}} = 45, 60$  and  $75$  m/s were  $-0.6\%$  to  $+1.2\%$  (Figure 6),  $-0.4\%$  to  $+1.4\%$  (Figure 7) and  $-0.2\%$  to  $+1.6\%$  (Figure 8) respectively.

### 2.5.2 Analysis With Respect to the Central Cross Section

Contours of  $(\bar{U} - \bar{U}_{0.0})/\bar{U}_{0.0}$  for  $\bar{U}_{\text{NOM}} = 30$  m/s and  $x_T = -1.0, 0.0$  and  $1.0$  m are shown in Figure 9. Corresponding plots for  $\bar{U}_{\text{NOM}} = 45, 60$  and  $75$  m/s are shown in Figures 10, 11 and 12 respectively. For the 12 sets of contours shown in Figures 9 to 12, a single normalizing velocity at the centre of the test section, i.e.  $\bar{U}_{0.0}$ , is used for each value of  $\bar{U}_{\text{NOM}}$ , which means that the normalizing velocity is not always associated with the  $x_T$  location of the contours, e.g.  $\bar{U}_{0.0}$  is used for contours at  $x_T = -1.0$  and  $1.0$  m. The contours in each of Figures 9 to 12 therefore show how mean velocities vary in the longitudinal or  $x_T$  direction. Mean velocities at given values of  $y_T$  and  $z_T$  increase as the flow moves downstream, which is consistent with the fact that the test section has a fixed cross-sectional area in the direction of the flow so that the effective flow area reduces with increasing  $x_T$  as the wall boundary layer thickens after the end of the contraction. For  $\bar{U}_{\text{NOM}} = 30$  m/s (Figure 9), the maximum variation in longitudinal mean velocities between  $x_T = -1.0$  m and  $x_T = +1.0$  m was from  $-0.6\%$  to  $+2.0\%$  respectively from their values at the centre of the test section ( $x_T = 0.0$ ,  $y_T = 0.0$  and  $z_T = 0.0$  m). Corresponding maximum variations for other nominal free-stream velocities were from  $-0.8\%$  to  $+1.6\%$  for  $\bar{U}_{\text{NOM}} = 45$  m/s (Figure 10), from  $-0.6\%$  to  $+1.8\%$  for  $\bar{U}_{\text{NOM}} = 60$  m/s (Figure 11) and from  $-0.2\%$  to  $+2.0\%$  for  $\bar{U}_{\text{NOM}} = 75$  m/s (Figure 12).

### 2.5.3 Longitudinal Velocity Variation

Selected data associated with the contours shown in Figures 9 to 12 have been replotted in Figure 13 to indicate how the mean velocities in the vertical and horizontal longitudinal centreplanes vary in the longitudinal or  $x_T$  direction. Data corresponding to the  $x_T$ - $z_T$  plane that passes through  $y_T = 0.0$  m (i.e. the vertical plane that is aligned with and passes through the tunnel longitudinal axis) are shown for  $z_T/H = 0.0, \pm 0.2$  and  $\pm 0.4$ , where  $H = 2134$  mm is the height of the test section of the LSWT (Figure 2). Similarly, data corresponding to the  $x_T$ - $y_T$  plane that passes through  $z_T = 0.0$  m (i.e. the horizontal plane that is aligned with and passes through the tunnel longitudinal axis) are shown for  $y_T/W = 0.0, \pm 0.15, \pm 0.30$  and  $\pm 0.45$ , where  $W = 2743$  mm is the width of the test section of the LSWT (Figure 2). In Figure 13, data corresponding to the longitudinal centreline of the tunnel are represented by thick lines. The longitudinal

mean velocities increase slightly in the  $x_T$  direction, for reasons given above. However, the changes in longitudinal mean velocities are not quite the same for the different values of  $\bar{U}_{\text{NOM}}$ , since the boundary layers on the walls of the test section develop differently for each of the values of  $\bar{U}_{\text{NOM}}$ . As for the contour plots, the asymmetry of the flow is apparent, as shown for example in Figure 13 (d).

#### 2.5.4 Effect of Change in Nominal Free-Stream Velocity

Contours of  $(\bar{U} - \bar{U}_{0.0})/\bar{U}_{0.0}$  for  $x_T = 0.0$  m and  $\bar{U}_{\text{NOM}} = 30, 45, 60$  and  $75$  m/s are shown in Figure 14 to indicate how the flow at a fixed  $x_T$  location changes as  $\bar{U}_{\text{NOM}}$  increases. The pattern of the contours and the magnitudes of the velocity deviations are approximately the same in each case, indicating that the distribution of the flow variations does not change significantly with  $\bar{U}_{\text{NOM}}$ .

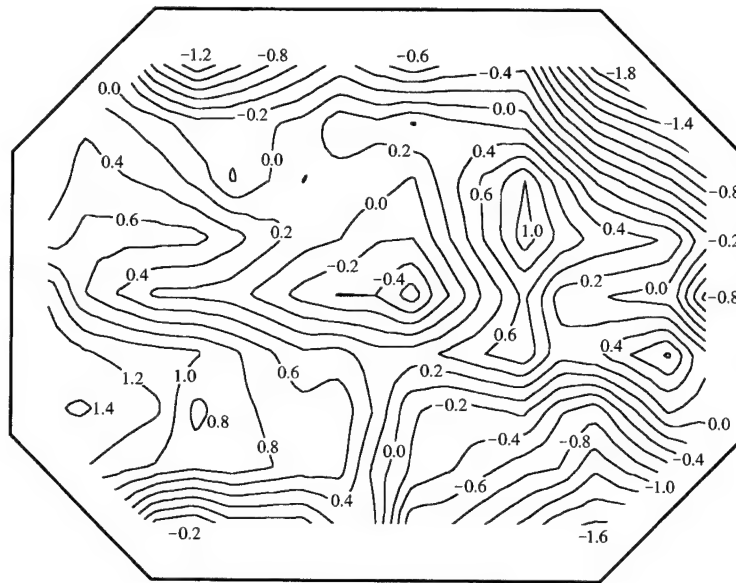
#### 2.5.5 Effect of Probe Misalignment With Respect to the Flow

The probability that the flow in the tunnel may be at a slight angle to the longitudinal axes of the probes on the cross-tunnel rake (Section 2.3) will not affect the test results significantly. In Reference 6 it is shown that, for total-pressure and static-pressure probes similar to those used on the cross-tunnel rake (see Figure 4), errors in measured total pressures and static pressures due to misalignment of the probes with the flow are negligible for flows whose angle of incidence is within  $\pm 5^\circ$  of the longitudinal axis of a total-pressure probe and within  $\pm 1^\circ$  of the longitudinal axis of a static-pressure probe. The angularity of the flow in the test section is generally less than  $1^\circ$  (see Section 3.7), so that errors in the dynamic pressure and hence the velocity will be small, and although strictly speaking the contours shown in Figures 5 to 12 and Figure 14 depict slightly inclined velocities, they can be considered to represent longitudinal velocities.

General discussion on the possible causes of the flow non-uniformities in the test section of the LSWT and suggested ways of improving the flow are given in Section 7.

## 2.6 Errors in Measured Mean Velocities

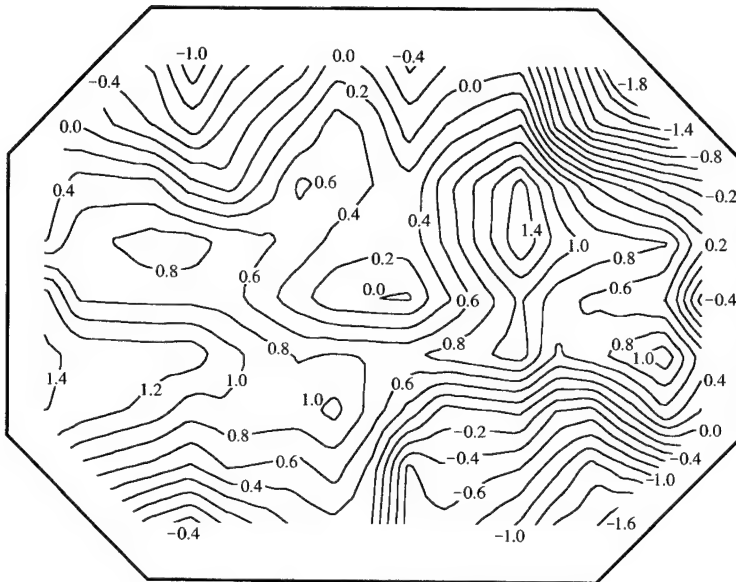
There are small errors in the velocity deviations, such as  $(\bar{U} - \bar{U}_{0.0})/\bar{U}_{0.0}$ , due to instrumentation errors. It was necessary to measure air temperatures and differential air pressures when determining mean velocities. Errors in the measured temperatures did not affect the velocity deviations as they are expressed as non-dimensional velocity ratios. The indicated readings of the scanners used to measure the differential pressures were accurate to within  $\pm 0.05\%$  of their full-scale reading. Two different types of scanners were used when measuring pressures and their ranges were  $159$  kPa ( $23.0$  psi) and  $\pm 6895$  Pa ( $\pm 1.0$  psi). For  $\bar{U}_{\text{NOM}} = 30, 45, 60$  and  $75$  m/s, errors in velocity deviations (e.g.  $(\bar{U} - \bar{U}_{0.0})/\bar{U}_{0.0}$ ) were about  $\pm 0.7, \pm 0.3, \pm 0.2$  and  $\pm 0.1$  percentage points respectively.



$$\frac{\bar{U} - \bar{U}_{0.0}}{\bar{U}_{0.0}} \%$$

$$\bar{U}_{\text{NOM}} = 30 \text{ m/s}$$

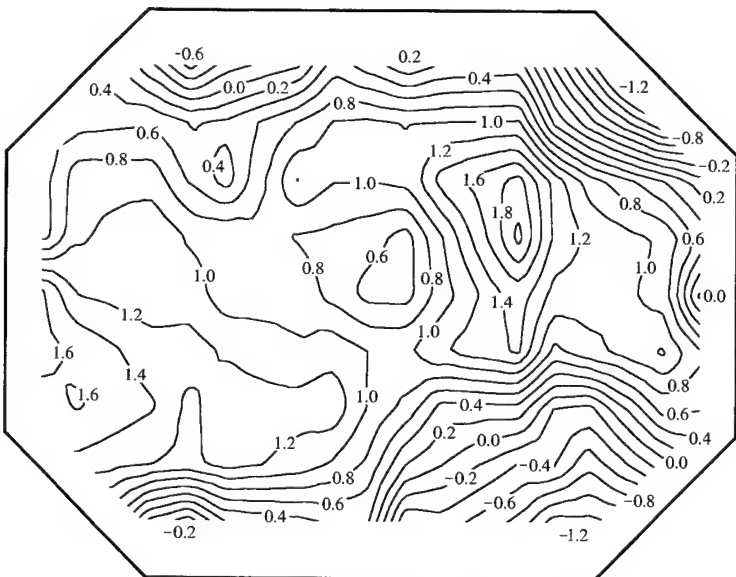
$$x_T = -1.0 \text{ m}$$



$$\frac{\bar{U} - \bar{U}_{0.0}}{\bar{U}_{0.0}} \%$$

$$\bar{U}_{\text{NOM}} = 30 \text{ m/s}$$

$$x_T = 0.0 \text{ m}$$



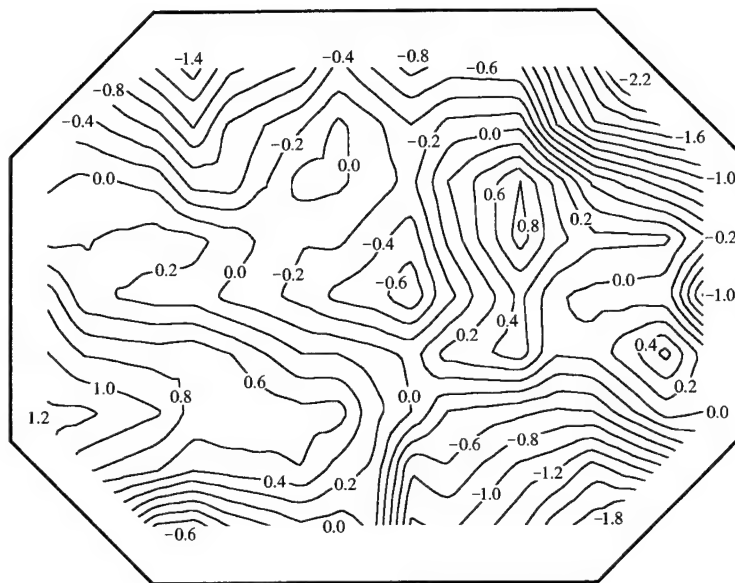
$$\frac{\bar{U} - \bar{U}_{0.0}}{\bar{U}_{0.0}} \%$$

$$\bar{U}_{\text{NOM}} = 30 \text{ m/s}$$

$$x_T = 1.0 \text{ m}$$

Figure 9. Contours of velocity deviation for  $\bar{U}_{\text{NOM}} = 30 \text{ m/s}$  for  $x_T = -1.0, 0.0$  and  $1.0 \text{ m}$ .

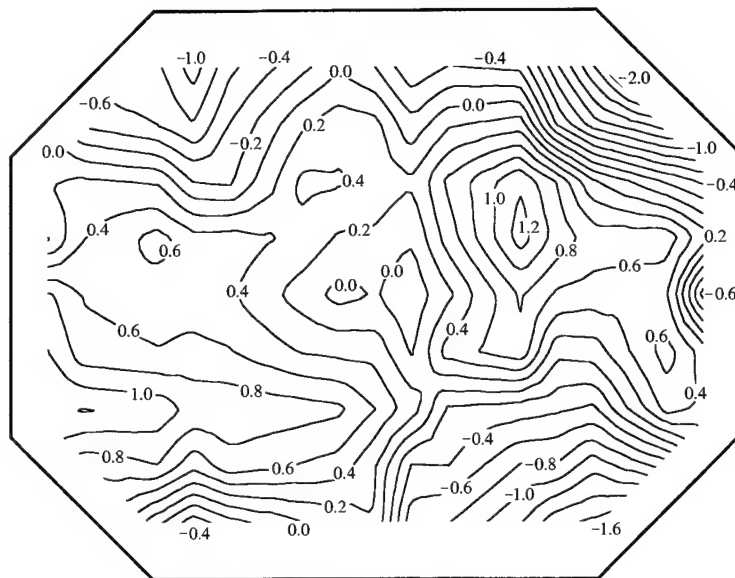
The flow is out of the page.



$$\frac{\bar{U} - \bar{U}_{0.0}}{\bar{U}_{0.0}} \%$$

$$\bar{U}_{\text{NOM}} = 45 \text{ m/s}$$

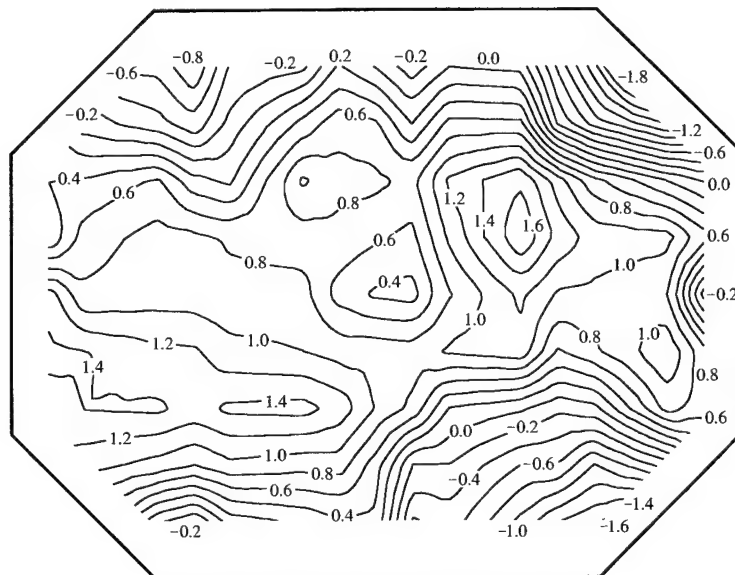
$$x_T = -1.0 \text{ m}$$



$$\frac{\bar{U} - \bar{U}_{0.0}}{\bar{U}_{0.0}} \%$$

$$\bar{U}_{\text{NOM}} = 45 \text{ m/s}$$

$$x_T = 0.0 \text{ m}$$



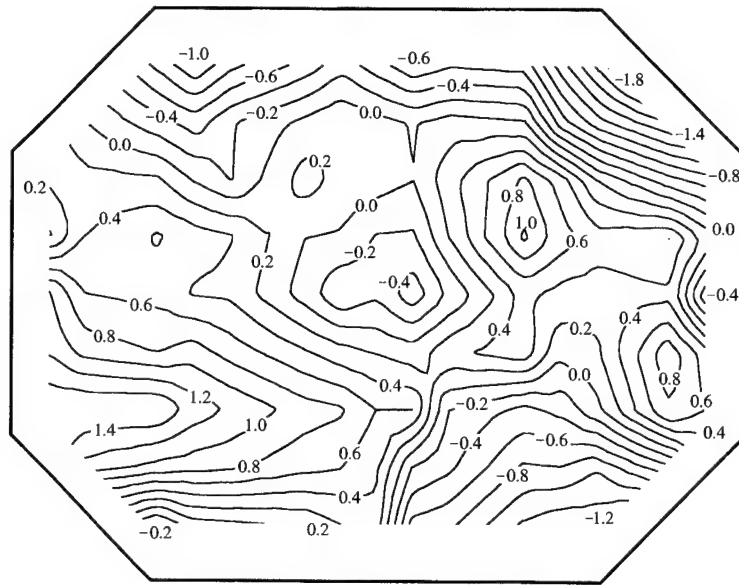
$$\frac{\bar{U} - \bar{U}_{0.0}}{\bar{U}_{0.0}} \%$$

$$\bar{U}_{\text{NOM}} = 45 \text{ m/s}$$

$$x_T = 1.0 \text{ m}$$

Figure 10. Contours of velocity deviation for  $\bar{U}_{\text{NOM}} = 45 \text{ m/s}$  for  $x_T = -1.0, 0.0$  and  $1.0 \text{ m}$ .

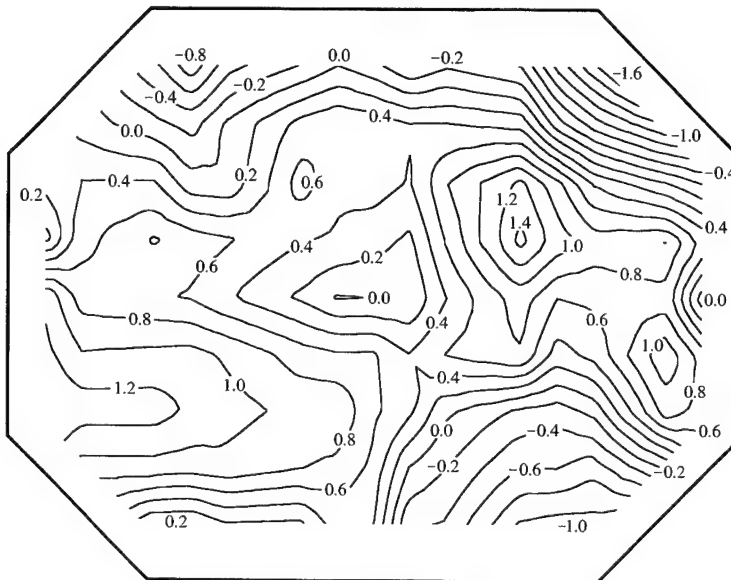
The flow is out of the page.



$$\frac{\bar{U} - \bar{U}_{0.0}}{\bar{U}_{0.0}} \%$$

$$\bar{U}_{\text{NOM}} = 60 \text{ m/s}$$

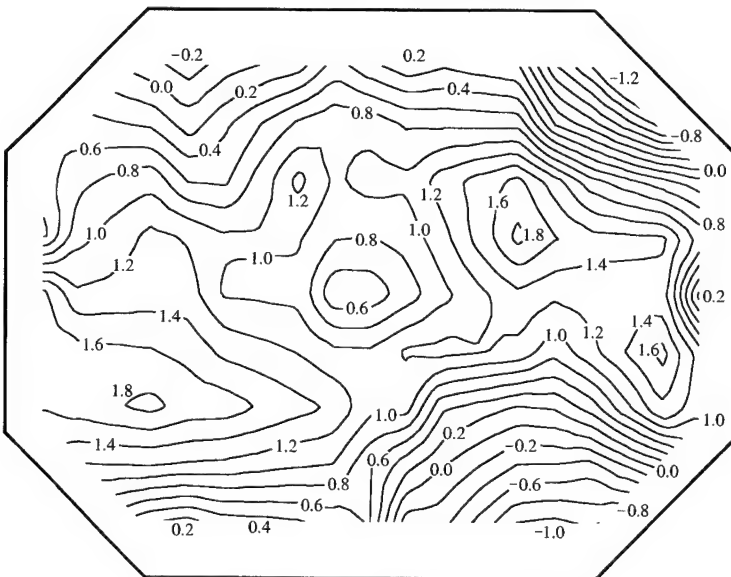
$$x_T = -1.0 \text{ m}$$



$$\frac{\bar{U} - \bar{U}_{0.0}}{\bar{U}_{0.0}} \%$$

$$\bar{U}_{\text{NOM}} = 60 \text{ m/s}$$

$$x_T = 0.0 \text{ m}$$



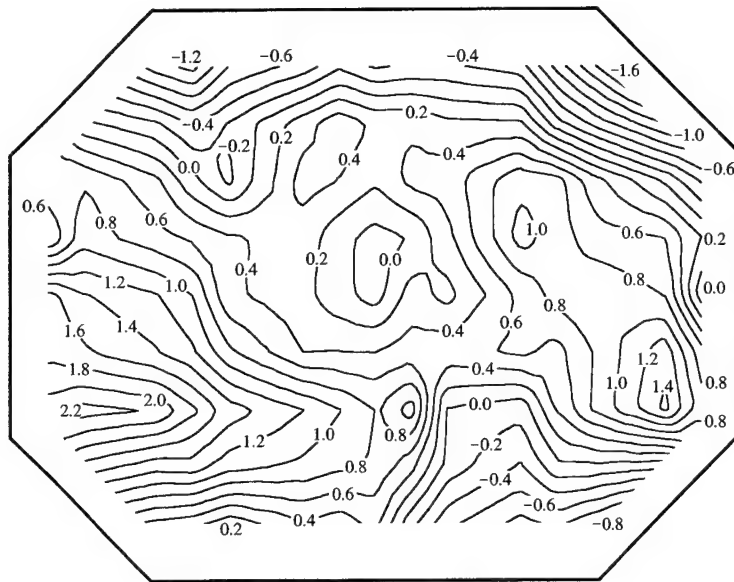
$$\frac{\bar{U} - \bar{U}_{0.0}}{\bar{U}_{0.0}} \%$$

$$\bar{U}_{\text{NOM}} = 60 \text{ m/s}$$

$$x_T = 1.0 \text{ m}$$

Figure 11. Contours of velocity deviation for  $\bar{U}_{\text{NOM}} = 60 \text{ m/s}$  for  $x_T = -1.0, 0.0$  and  $1.0 \text{ m}$ .

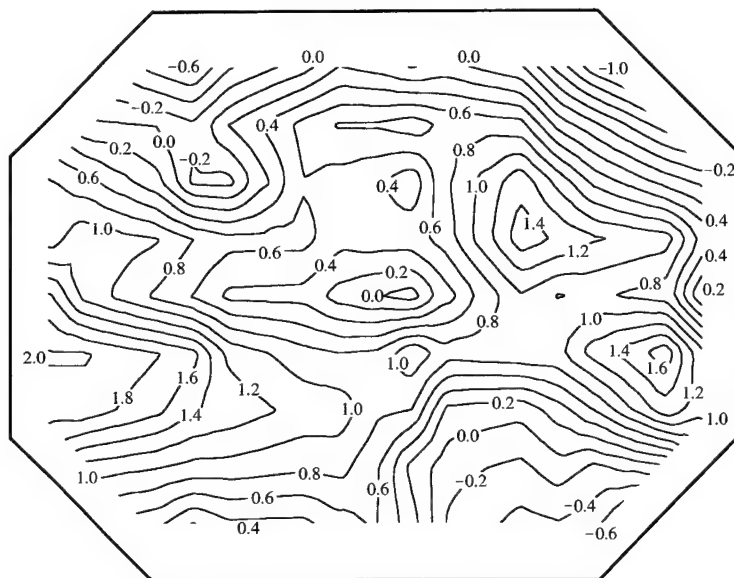
The flow is out of the page.



$$\frac{\bar{U} - \bar{U}_{0.0}}{\bar{U}_{0.0}} \%$$

$$\bar{U}_{\text{NOM}} = 75 \text{ m/s}$$

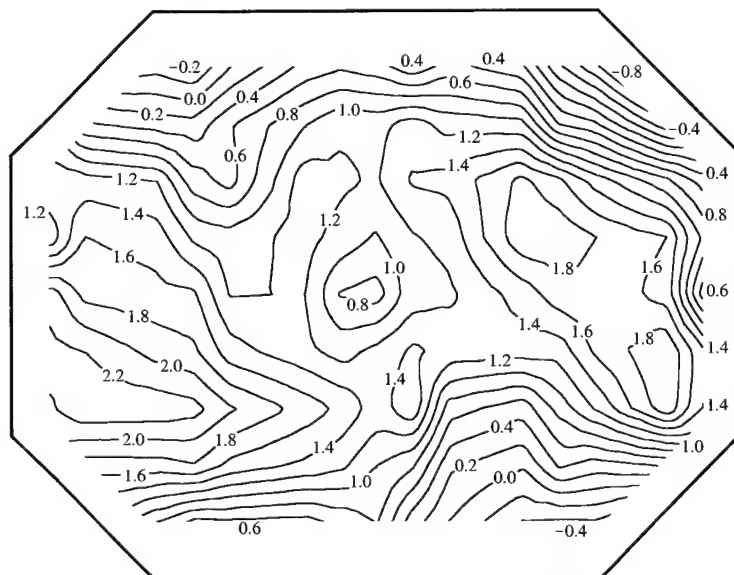
$$x_T = -1.0 \text{ m}$$



$$\frac{\bar{U} - \bar{U}_{0.0}}{\bar{U}_{0.0}} \%$$

$$\bar{U}_{\text{NOM}} = 75 \text{ m/s}$$

$$x_T = 0.0 \text{ m}$$



$$\frac{\bar{U} - \bar{U}_{0.0}}{\bar{U}_{0.0}} \%$$

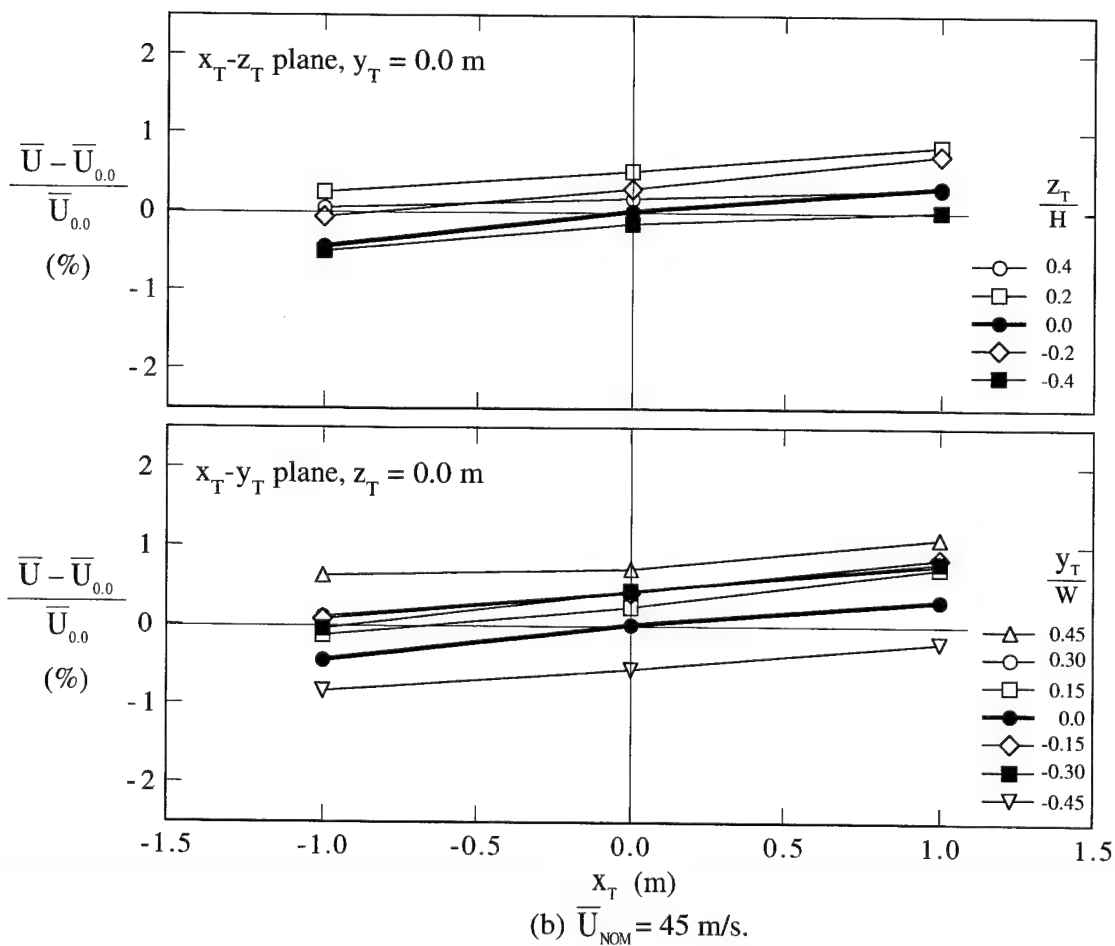
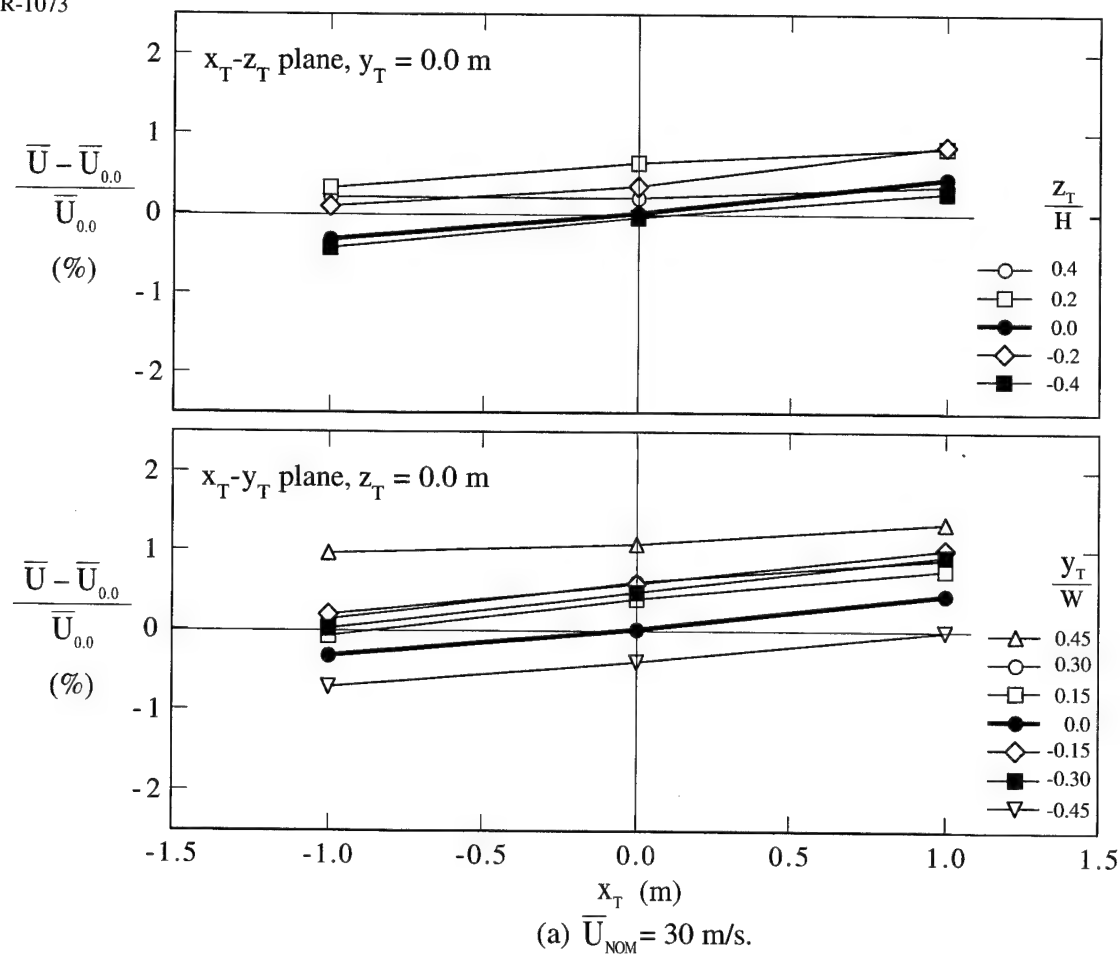
$$\bar{U}_{\text{NOM}} = 75 \text{ m/s}$$

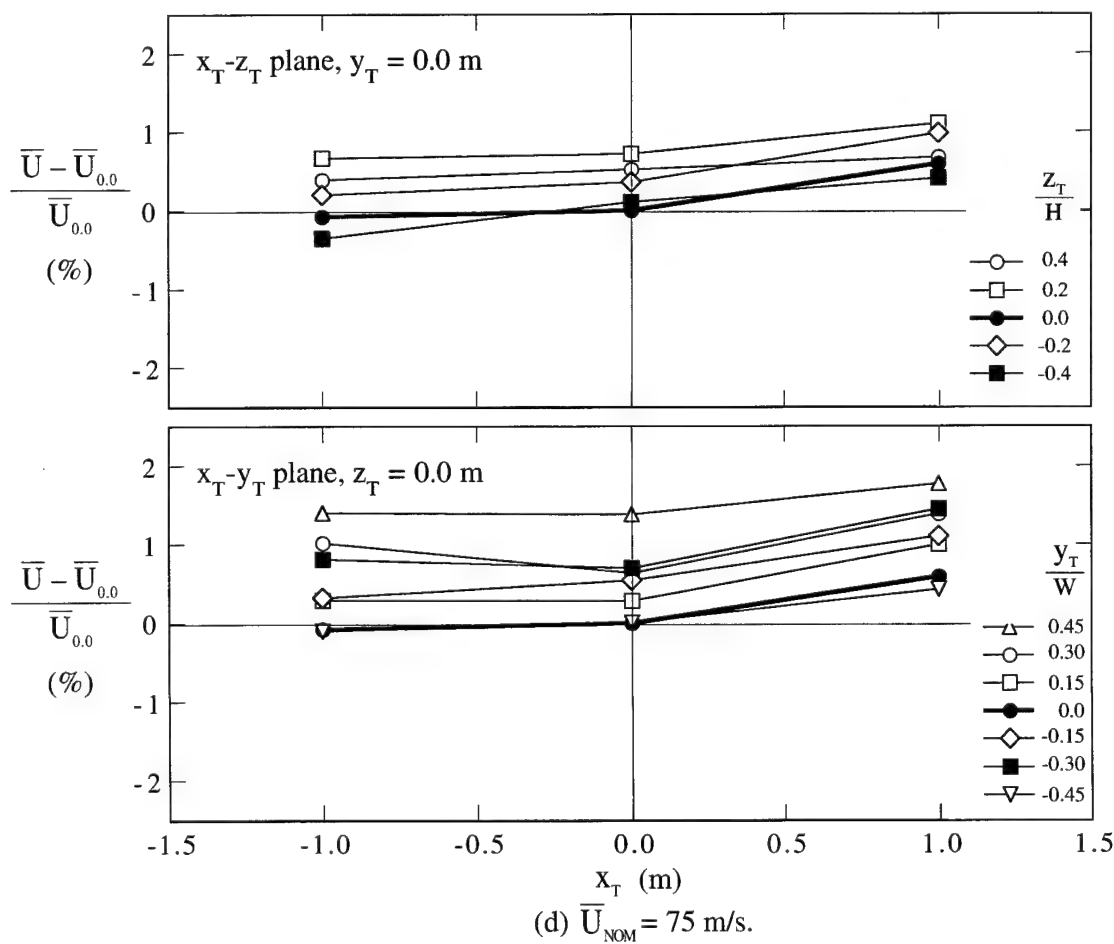
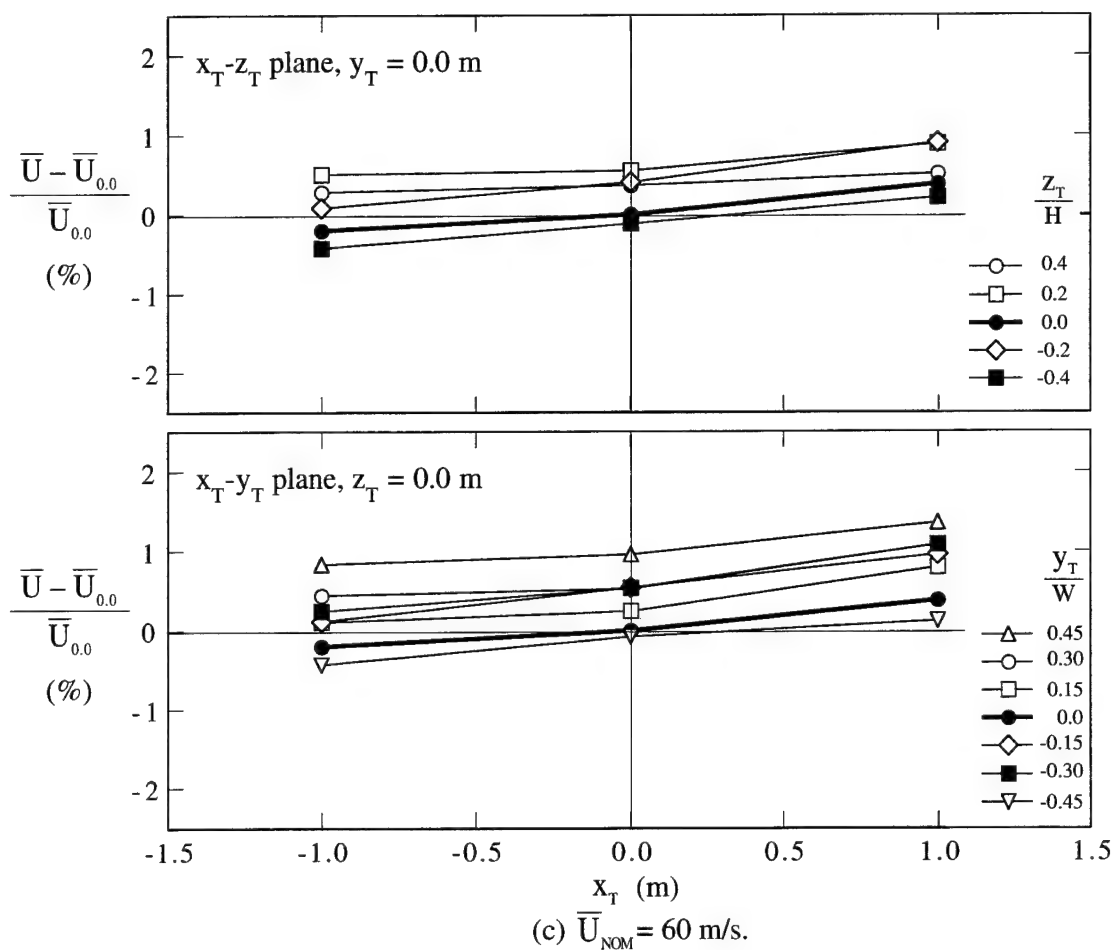
$$x_T = 1.0 \text{ m}$$

Figure 12. Contours of velocity deviation for  $\bar{U}_{\text{NOM}} = 75 \text{ m/s}$  for  $x_T = -1.0, 0.0$  and  $1.0 \text{ m}$ .

The flow is out of the page.



Figure 13. Velocity deviations in the  $x_T$  direction for  $\bar{U}_{\text{NOM}} = 30, 45, 60$  and  $75$  m/s.

Figure 13 cont'd. Velocity deviations in the  $x_T$  direction for  $\bar{U}_{NOM} = 30, 45, 60$  and  $75$  m/s.

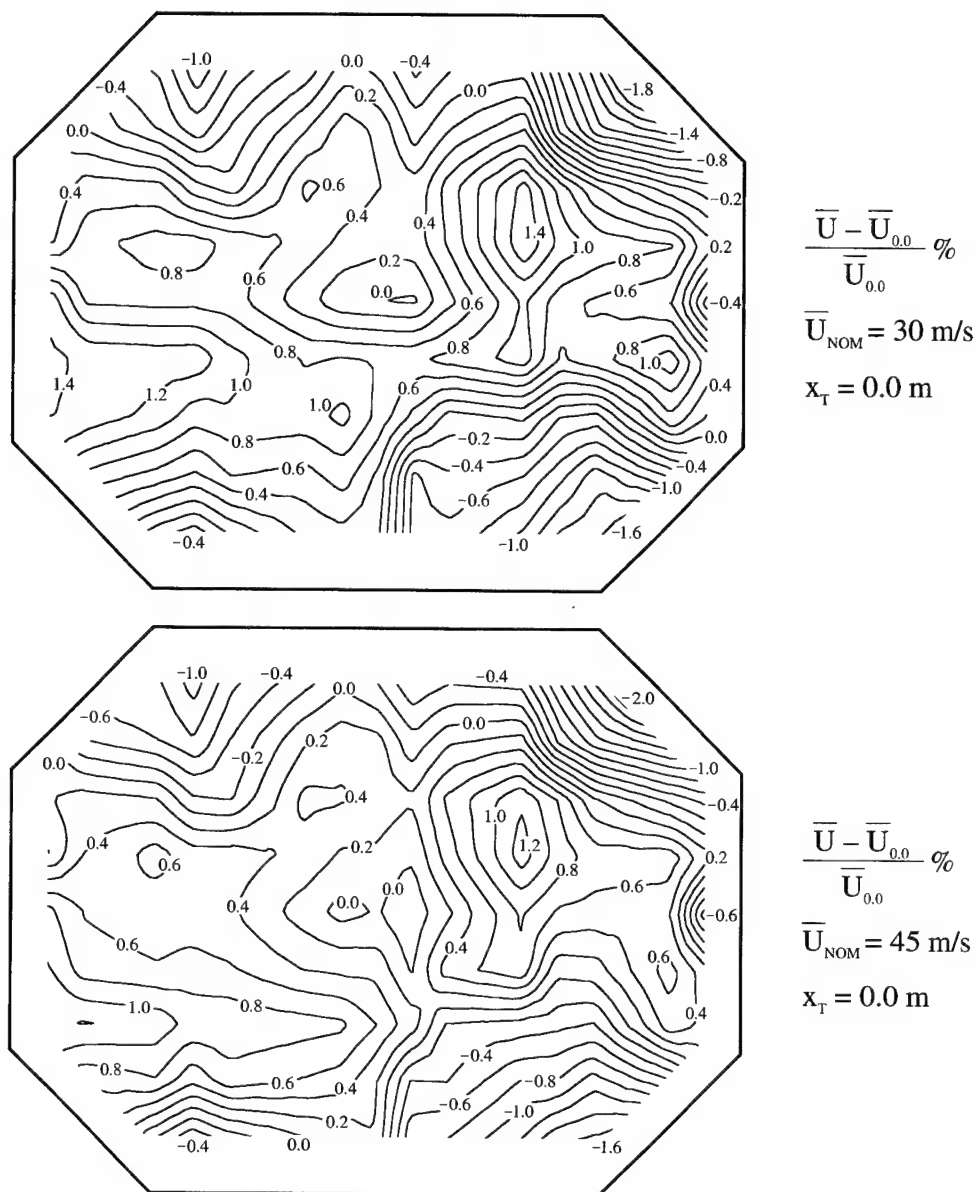
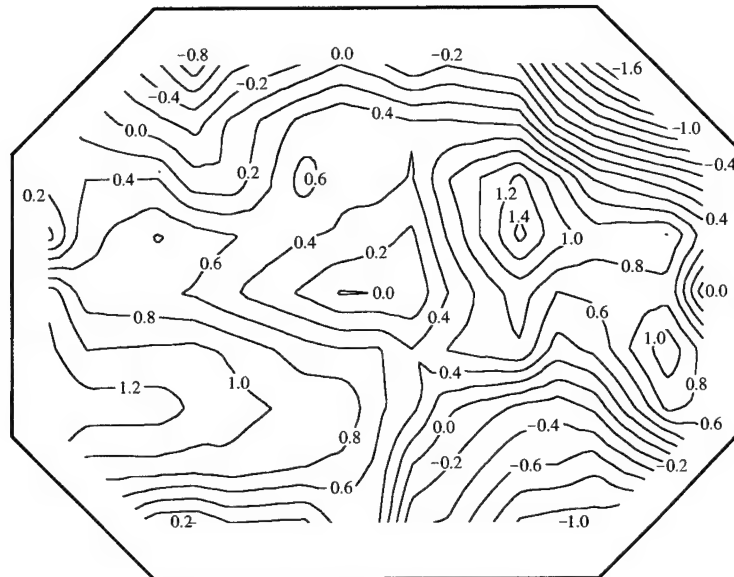


Figure 14. Contours of velocity deviation for  $\bar{U}_{\text{NOM}} = 30, 45, 60$  and  $75 \text{ m/s}$  for  $x_T = 0.0 \text{ m}$ .

(a)  $\bar{U}_{\text{NOM}} = 30$  and  $45 \text{ m/s}$ .

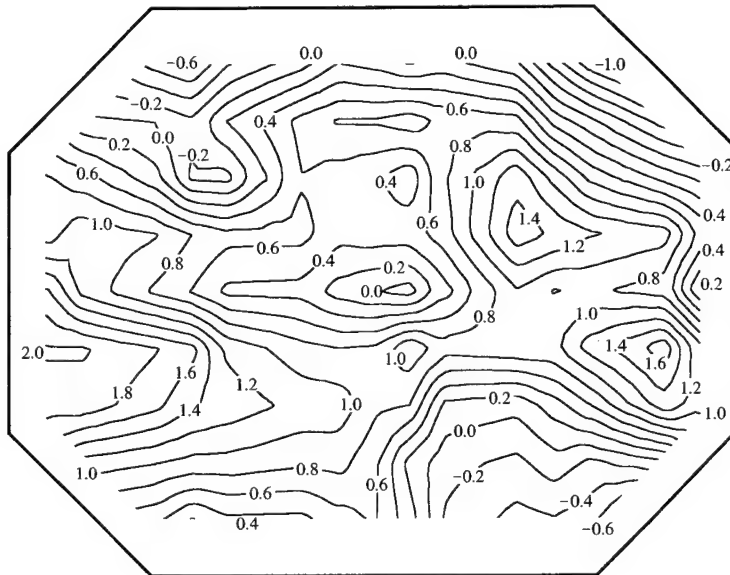
The flow is out of the page.



$$\frac{\bar{U} - \bar{U}_{0.0}}{\bar{U}_{0.0}} \%$$

$$\bar{U}_{\text{NOM}} = 60 \text{ m/s}$$

$$x_T = 0.0 \text{ m}$$



$$\frac{\bar{U} - \bar{U}_{0.0}}{\bar{U}_{0.0}} \%$$

$$\bar{U}_{\text{NOM}} = 75 \text{ m/s}$$

$$x_T = 0.0 \text{ m}$$

Figure 14 cont'd. Contours of velocity deviation for  $\bar{U}_{\text{NOM}} = 30, 45, 60$  and  $75 \text{ m/s}$  for  $x_T = 0.0 \text{ m}$ .

(b)  $\bar{U}_{\text{NOM}} = 60$  and  $75 \text{ m/s}$ .

The flow is out of the page.

### 3. Flow-Angle Measurements

#### 3.1 Test Schedule

Flow angles were measured in the test section at the 155 grid points shown in Figure 2 for  $x_T = -1.0, 0.0$  and  $1.0$  m and for  $\bar{U}_{\text{NOM}} = 30$  and  $60$  m/s.

#### 3.2 Six-Hole Probe

A six-hole hemispherical head yawmeter, designed and calibrated by Melbourne & Griss (Reference 7), was used to measure magnitudes of mean velocities and corresponding flow angles at the different grid points. The probe is depicted diagrammatically in Figure 15. Holes 1 to 5 are located in the hemispherical head of the probe as shown and the series of 20 interconnected holes, designated hole 6, are equally spaced around the circumference of the probe and are located  $22.2$  mm ( $3.5$  probe diameters) from the probe tip. Each of holes 1 to 6 is connected internally to ports at the rear of the probe to enable the individual pressures to be measured. A datum line scribed on the probe body near hole 1 and contained in the plane passing through holes 1, 3 and 5, was used to differentiate the holes and to set the probe roll angle in the tunnel (Section 3.4).

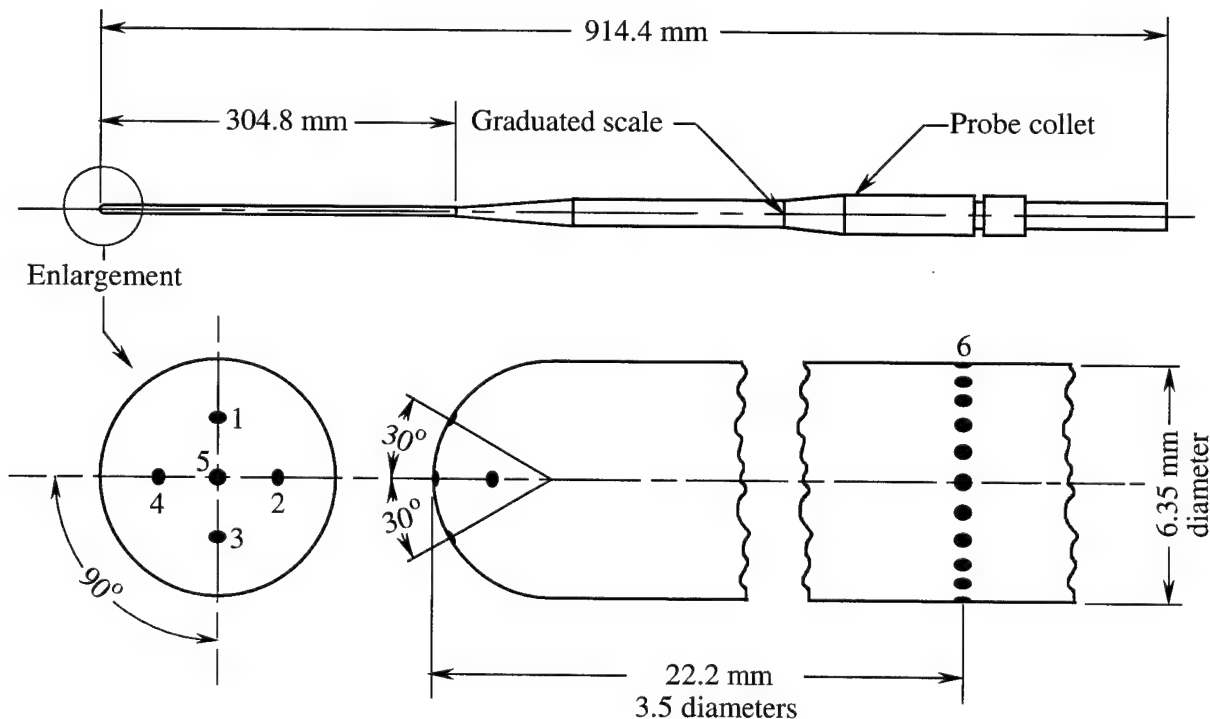


Figure 15. Six-hole probe (based on a diagram given in Reference 7).

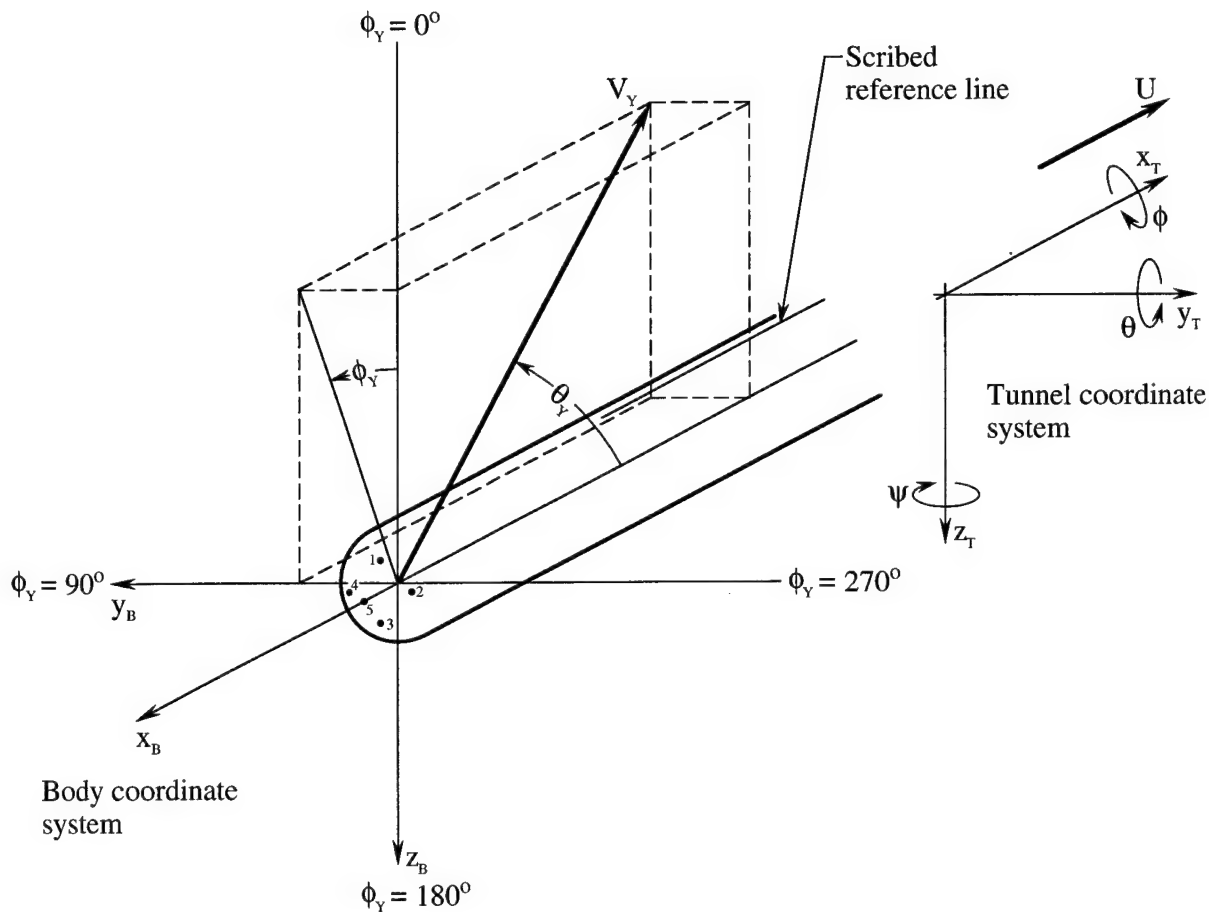


Figure 16. Six-hole probe showing velocity vector, flow angles and coordinate systems (based on a diagram given in Reference 7).

The direction of the velocity vector,  $V_y$ , relative to the probe body coordinate system,  $x_B y_B z_B$ , is defined in terms of flow angles  $\theta_y$  and  $\phi_y$ , as shown in Figure 16. The coordinate system remains fixed with respect to the probe and its origin is located at the centre of the hemisphere which forms the tip of the probe. The  $x_B$  axis is along the probe longitudinal axis, the  $y_B$  axis is in the plane passing through holes 2, 4 and 5 and the  $z_B$  axis is in the plane passing through holes 1, 3 and 5. The positive directions of the axes are as shown and the axes form a right-handed orthogonal system. The axes convention is the same as that used by Fairlie (Reference 8). The tunnel coordinate system,  $x_T y_T z_T$ , introduced in Section 2.1, is also shown in Figure 16. The relationship between the two coordinate systems is given in Section 3.3.

The probe can be used in either the stationary or the null-sensing mode. In the stationary mode, the probe is given a known orientation with respect to the wind tunnel and by measuring the pressures in the six holes the velocity  $V_y$  and the flow angles  $\theta_y$  and  $\phi_y$  can be determined using calibration relationships. Velocities and flow angles relative to the tunnel coordinate system can then be determined (Section 3.5). In the null-sensing mode, the probe is oriented so that the pressures in holes 1 to 4 are equal, which signifies that the velocity vector is parallel to the probe longitudinal axis. The magnitude of the velocity vector can then be determined in the conventional manner using the total and static pressures measured in holes 5 and 6 respectively, i.e.  $V_y = [2(p_s - p_6)/\rho]^{0.5}$ , and the direction of the velocity vector can be determined by measuring the orientation of the probe relative to the tunnel coordinate system. The null-sensing mode of operation is cumbersome and time consuming, whereas the stationary mode is straightforward and it was the method used for the current measurements.

Melbourne & Griss (Reference 7) calibrated the probe in the LSWT for free-stream velocities of 100 and 200 ft/s (30.5 and 61.0 m/s respectively) and obtained expressions relating  $V_y$ ,  $\theta_y$  and  $\phi_y$  to measured pressures,  $p_1$  to  $p_6$ . From their calibration measurements, they found that

$$\theta_y = 1.983 R^3 - 2.105 R^2 + 16.917 R \quad (7)$$

for a free-stream velocity of 100 ft/s (30.5 m/s) and

$$\theta_y = -0.050 R^3 + 2.686 R^2 + 14.013 R \quad (8)$$

for a free-stream velocity of 200 ft/s (61.0 m/s). In these two expressions,  $R$  is given by

$$R = \left\{ (C_{p_3} - C_{p_1})^2 + (C_{p_2} - C_{p_4})^2 \right\}^{0.5} \quad (9)$$

where the pressure coefficients,  $C_{p_n}$ , ( $n = 1$  to  $4$ ) are given by

$$C_{p_n} = \frac{(p_n - p_{\text{ref}})}{0.5 \rho V_y^2} \quad (10)$$

Melbourne & Griss also found that

$$C_{p_5} - C_{p_6} = \frac{(p_5 - p_6)}{0.5 \rho V_y^2} = -0.000493 \theta_y^2 + 0.004472 \theta_y + 1.003 \quad (11)$$

for a free-stream velocity of 100 ft/s (30.5 m/s) and

$$C_{p_5} - C_{p_6} = \frac{(P_5 - P_6)}{0.5 \rho V_Y^2} = -0.000535 \theta_Y^2 + 0.005854 \theta_Y + 1.014 \quad (12)$$

for a free-stream velocity of 200 ft/s (61.0 m/s). Equations 7, 8, 11 and 12 were determined using the method of least squares to fit data.

The flow angle,  $\phi_Y$ , is related to pressure coefficients by the following relationship:

$$\phi_Y = \tan^{-1} \left( \frac{C_{p_2} - C_{p_4}}{C_{p_3} - C_{p_1}} \right) \quad (13)$$

If  $\theta_Y$  is very small, the values of  $C_{p_1}$ ,  $C_{p_2}$ ,  $C_{p_3}$  and  $C_{p_4}$  will be approximately the same so that equation 13 will be ill-conditioned and may break down.

In the above calibration relationships (equations 7 to 13),  $V_Y$ ,  $\theta_Y$  and  $\phi_Y$  are not given explicitly in terms of measured pressures,  $p_1$  to  $p_6$ , and it was necessary to determine the three variables iteratively. The procedure used is discussed in Section 3.5.

In the current investigation, the probe calibration applicable to a free-stream velocity of 100 ft/s (30.5 m/s) was only used for flow-angle measurements at  $\bar{U}_{\text{NOM}} = 30$  m/s and similarly the calibration applicable to a velocity of 200 ft/s (61.0 m/s) was only used for measurements at  $\bar{U}_{\text{NOM}} = 60$  m/s.

### 3.3 Transformation of Coordinates

The orientation of one set of axes relative to any other set can be given by three angles, which are the consecutive rotations about the (right-handed) axes  $z$ ,  $y$  and  $x$  in that order that carry one set of axes into coincidence with the other (Reference 8). In Figure 16, the angles that rotate the tunnel axes,  $x_T$ ,  $y_T$  and  $z_T$ , into coincidence with the body axes,  $x_B$ ,  $y_B$  and  $z_B$ , are referred to as the yaw angle,  $\psi$ , the pitch angle,  $\theta$ , and the roll angle,  $\phi$ . The positive directions of  $\psi$ ,  $\theta$  and  $\phi$  conform to the conventional right-hand screw rule about the relevant axes, as shown in Figure 16. For the orientation of the tunnel and body axes shown in Figure 16,  $\psi$  is  $180.0^\circ$ ,  $\theta$  is  $0.0^\circ$  and  $\phi$  is  $0.0^\circ$ .

The velocity vector,  $V_Y$ , shown in Figure 16, can be resolved into three components of velocity in the body coordinate system to give  $\bar{U}_B$ ,  $\bar{V}_B$  and  $\bar{W}_B$ , corresponding to the  $x_B$ ,  $y_B$  and  $z_B$  directions respectively. For arbitrary values of  $\psi$ ,  $\theta$  and  $\phi$ , components of velocity in the tunnel coordinate system,  $\bar{U}_T$ ,  $\bar{V}_T$  and  $\bar{W}_T$ , can be determined from components of velocity in the body coordinate system,  $\bar{U}_B$ ,  $\bar{V}_B$  and  $\bar{W}_B$ , using



$$\begin{bmatrix} \bar{U}_T \\ \bar{V}_T \\ \bar{W}_T \end{bmatrix} = [\lambda]_{TB} \begin{bmatrix} \bar{U}_B \\ \bar{V}_B \\ \bar{W}_B \end{bmatrix} \quad (14)$$

where  $[\lambda]_{TB}$  is a matrix of direction cosines that is used to transform velocities from the body coordinate system to the tunnel coordinate system. The matrix  $[\lambda]_{TB}$  is given by

$$[\lambda]_{TB} = \begin{bmatrix} \cos \theta \cos \psi & \sin \phi \sin \theta \cos \psi & \cos \phi \sin \theta \cos \psi \\ & -\cos \phi \sin \psi & +\sin \phi \sin \psi \\ \cos \theta \sin \psi & \sin \phi \sin \theta \sin \psi & \cos \phi \sin \theta \sin \psi \\ & +\cos \phi \cos \psi & -\sin \phi \cos \psi \\ -\sin \theta & \sin \phi \cos \theta & \cos \phi \cos \theta \end{bmatrix} \quad (15)$$

which is the transpose of  $[\lambda]_{BT}$ , given for example in Reference 8.

### 3.4 Traversing Mechanism

A specially designed traversing mechanism was used to support the six-hole probe and to position it at different vertical locations in the tunnel when measuring velocities and flow angles. A photograph of the mechanism mounted in the tunnel is given in Figure 17 and a plan cross section assembly drawing of the mechanism showing the main features is given in Figure 18. Photographs of components of the mechanism are given in Figure 19. The probe is mounted on a carriage which can move up or down (into and out of the paper in Figure 18) between two linear-motion rails, and the carriage is connected to the linear-motion rails using three low-friction linear-motion bearings –see Figure 19 (b). A stepping motor is connected to a lead screw which passes through the carriage and instructions can be sent to the motor from a computer to rotate the lead screw and move the probe to a specified  $z_T$  location –see Figure 19 (c). Limit switches are installed near the top and near the bottom of the downstream linear-motion rail to prevent the carriage moving beyond acceptable lower and upper limits of travel –see Figure 19. An electric brake, which is activated when the switch to the stepping motor is off or when the power to the motor fails, was installed on the lead screw to prevent it from rotating under these conditions –see Figure 19 (a). Without the brake, the weight of the carriage and the components attached would cause the lead screw to rotate and the carriage would move down when there was no power to the motor. A dummy probe is attached to the traversing mechanism to counteract possible twisting of the mechanism that would arise from aerodynamic loads on a single probe. The active and dummy probes can be swapped as required by simply transferring the

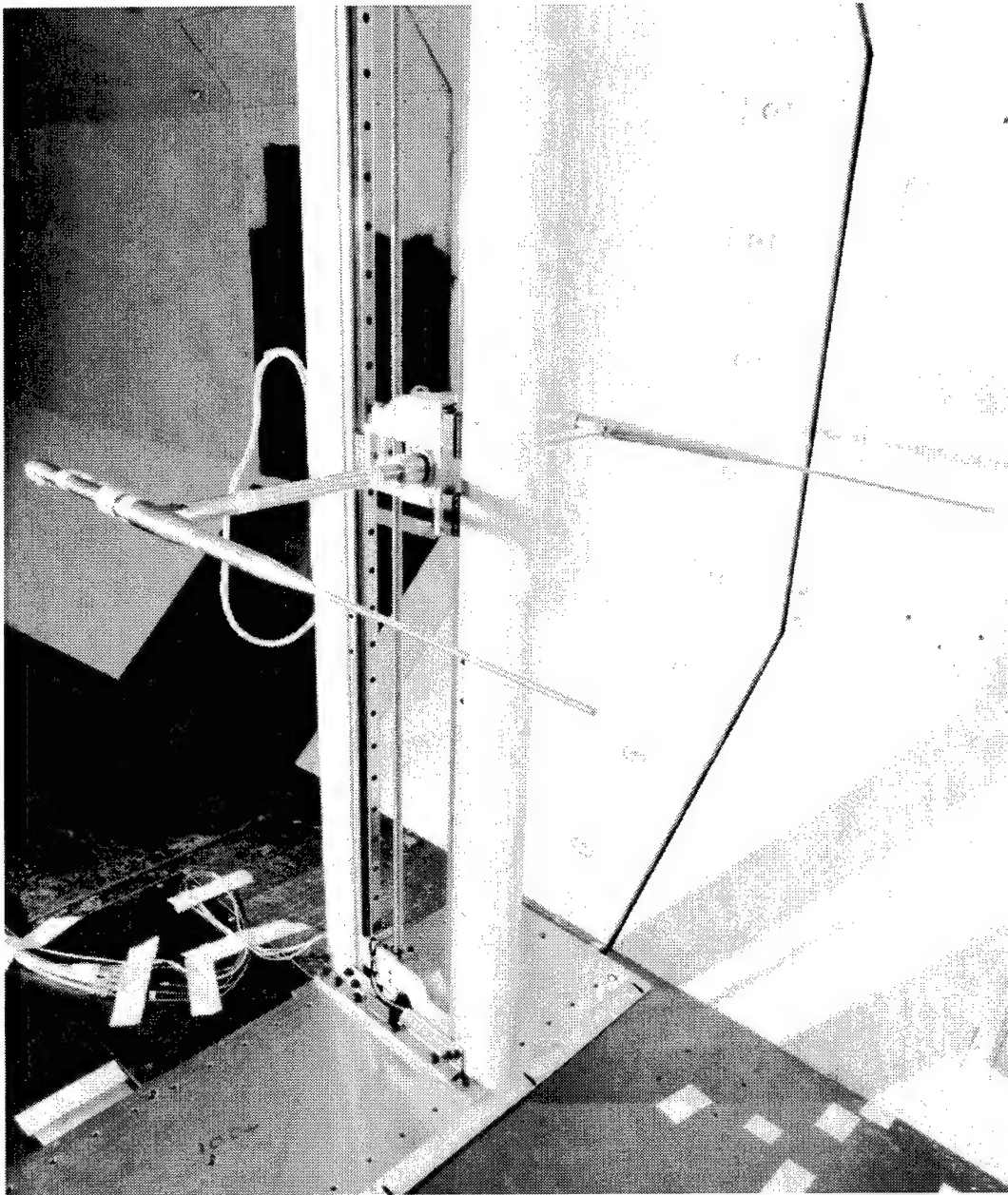


Figure 17. Traversing mechanism, with probes attached, mounted in the low-speed wind tunnel.

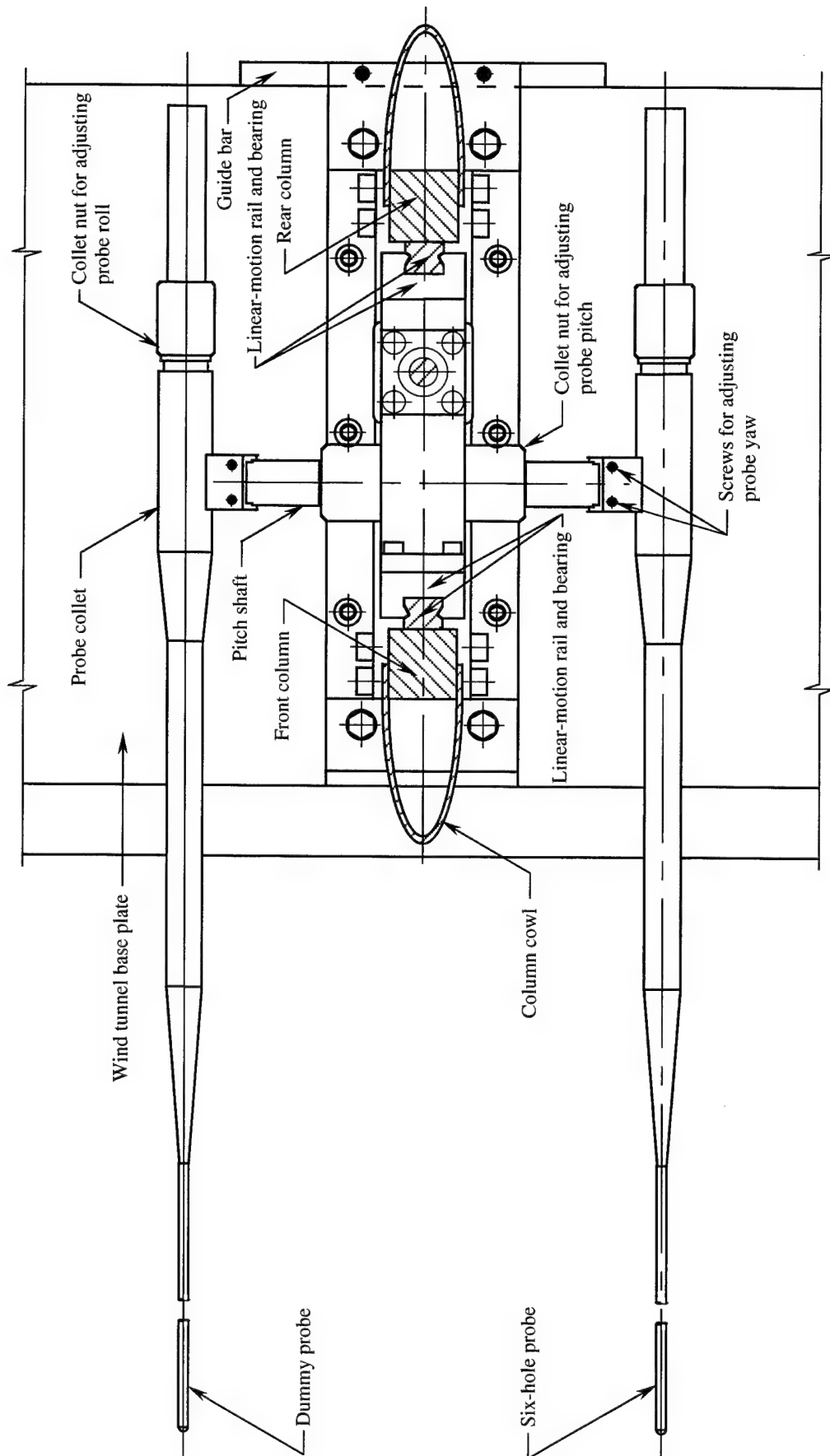
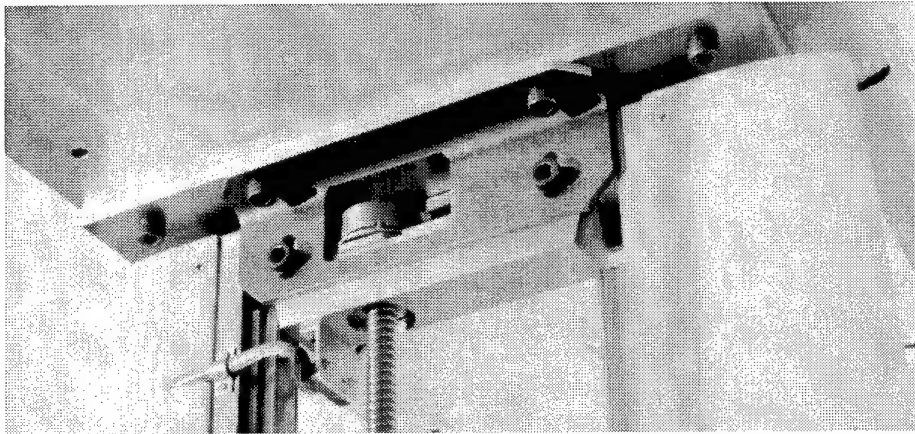
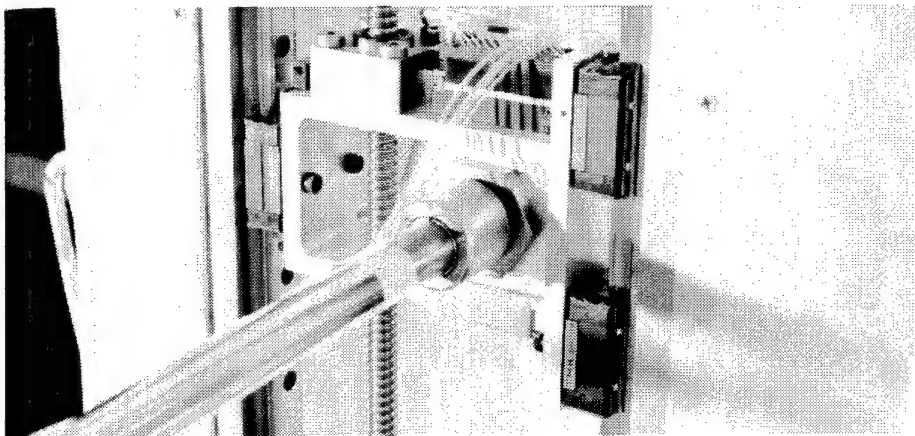


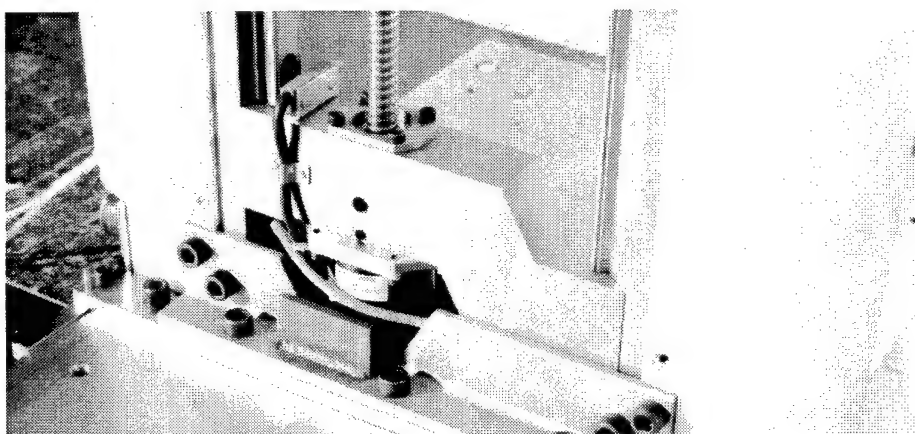
Figure 18. Assembly drawing of the traversing mechanism and probes.



(a) top part showing electric brake



(b) carriage



(c) bottom part showing stepping motor

Figure 19. Components of the traversing mechanism.

probes from one collet to the other (Figure 18), without changing the yaw, pitch and roll angles of the probes. The horizontal arm holding the probes is interchangeable with arms of different lengths, thereby enabling measurements to be taken at different  $y_T$  locations without changing the lateral position of the rig.

The traversing mechanism was bolted to two rectangular plates, one of which was bolted to the floor and the other to the roof of the test section. The plates were 0.4 m long and 1.6 m wide and occupied most of the width of the floor (or roof) not counting the fillets (the lower plate is shown in Figure 17). The lower plate was installed first and it was fixed to the floor of the test section so that its trailing edge was parallel to the  $y_T$  direction and so that the tip of the six-hole probe would be located at the required  $x_T$  position when the mechanism was bolted between the plates. The lower plate was aligned accurately by first ensuring that the midpoint of its trailing edge was positioned on the longitudinal centreline of the floor of the tunnel. If necessary, the yaw angle of the plate was then adjusted slightly so that the distances from each of the two extremities of the trailing edge to an upstream or downstream reference mark (at least 2.0 m from the trailing edge) on the longitudinal centreline of the floor of the tunnel were the same. Using this technique, the error in the setting of the yaw angle of the plate could be kept to less than about  $\pm 0.1^\circ$ . The alignment of the trailing edge of the plate with the  $y_T$  direction was critical since probe yaw angles were referenced to the plate trailing edge. The fore/aft location of the lower plate did not have to be precise, since the probe could be adjusted axially (by up to about 45 cm) through the probe collet (Figure 18). A special alignment frame, shown in Figure 20, was used to ensure that the upper plate was located directly above the lower plate. The frame was bolted firmly to the lower plate, using dowel pins for alignment. The top plate was then mounted on four blocks attached to the frame, using dowel pins for alignment. Four set screws on the frame were used to lift the blocks and the top plate until the plate came into contact with the roof of the test section. Guide pins minimized lateral movement of the top plate while it was being raised. The top plate was then bolted to the roof of the test section and the frame was removed from the tunnel. The traversing mechanism was then positioned on the lower plate, using a guide bar at the foot of the mechanism (Figure 18) to ensure that the base of the mechanism was not twisted relative to the trailing edge of the lower plate. The traversing mechanism was then bolted to the lower plate so that the probe tip was located at the required  $y_T$  position. The two vertical linear-motion rails on the mechanism (Figure 18) were positioned so that they were less than  $0.05^\circ$  from the vertical, as measured with an inclinometer on two adjacent sides of each rail, and the mechanism was then bolted to the upper plate.

There is provision on the mechanism to change the orientation of the six-hole probe (and the dummy probe). The yaw angle,  $\psi$ , pitch angle,  $\theta$ , and roll angle,  $\phi$ , can all be altered independently (see Figure 18 for adjustment mechanisms). On the mechanism,  $\psi$  could be varied by about  $\pm 15^\circ$ ,  $\theta$  by  $360^\circ$  and  $\phi$  by  $360^\circ$ . It would have been relatively difficult to set values of  $\psi$  to the accuracy needed when the probe longitudinal axis was horizontal (i.e.  $\theta = 0^\circ$ ), but by rotating the pitch shaft (Figure 18) so that the probe longitudinal axis was temporarily approximately vertical, and then adjusting the

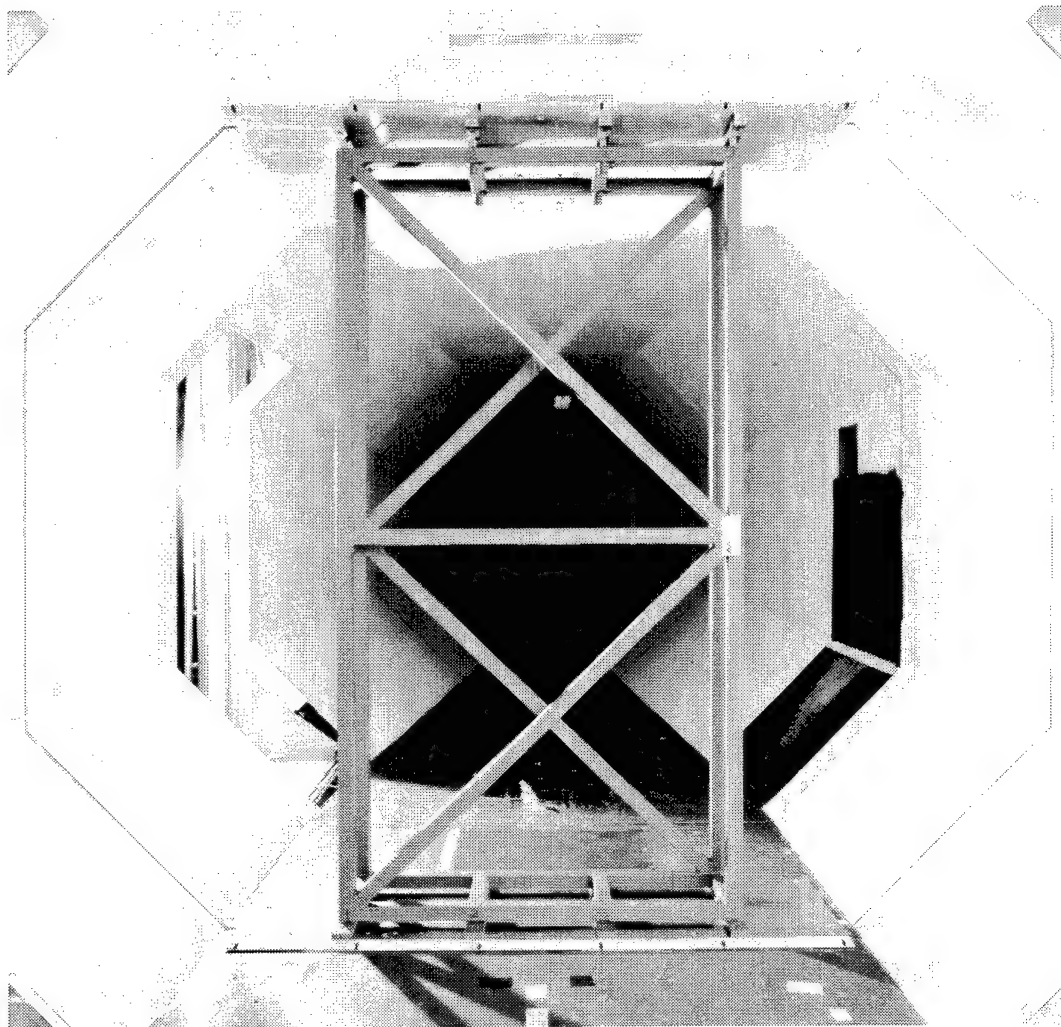


Figure 20. Alignment frame used when locating the upper plate of the traversing mechanism on the test section roof with respect to the lower plate on the floor.

yaw screws to set the probe vertical in the  $y_T$ - $z_T$  plane, using an inclinometer on the probe body, and then returning the probe to the horizontal position, values of  $\psi$  could be set to  $0.0^\circ$  to an accuracy of about  $\pm 0.02^\circ$ . An inclinometer was also used to set values of  $\theta$  to an accuracy of about  $\pm 0.02^\circ$ . Values of  $\phi$  were set by rolling the probe until the scribed reference line on the body of the probe (Figure 16) matched the appropriate scribed line on the graduated scale on the collet (Figure 15). A microscope was used when matching the scribed lines and values of  $\phi$  were set to an accuracy of about  $\pm 0.2^\circ$ .

The traversing mechanism is a precision device and was manufactured to high accuracy. However, as with any practical device, the individual components on the mechanism all had manufacturing tolerances. Checks were done and it was found that the possible error in the setting of the yaw angle of the six-hole probe due to these effects could be up to  $\pm 0.1^\circ$ . This would occur if components had been manufactured to the limits of their tolerances (either maximum or minimum limits) and then assembled so that the effects of the inbuilt imperfections were maximized, i.e. the worst possible case.

It was found that the engraved scales on both of the probe collets (Figure 15) are rolled slightly from the true zero position and these offsets have to be allowed for when setting probe roll angles. The engraved scale on the port collet has a zero error of  $+2.10^\circ$  and the scale on the starboard collet has a zero error of  $+1.35^\circ$ , i.e. the engraved scales are both rolled clockwise when looking in the direction from the rear of the probe to the hemispherical tip of the probe (Figure 15).

The movement of the probe was controlled using software program WINDRIG located on a PC. Initially the user must enter the current  $z_T$  position of the probe relative to the floor of the test section. This initial setting is used as a reference for subsequent positioning of the probe. The user must then enter the lower and upper  $z_T$  limits corresponding to the permissible probe movement. These limits are independent of the limits set by the limit switches (see above) and would be used, for example, if the probe was being traversed between the corner fillets in the octagonal test section. To minimize the possibility of damaging the probe and the traversing mechanism, the program has been written so that it is not possible to move the probe using the program unless these limits have been entered. Finally, the user must enter the destination value of  $z_T$  and the mechanism then moves the probe as required. The smallest permissible probe movement from a given location is 0.1 mm and the probe can be positioned to an accuracy of 0.1 mm relative to its initial setting.

### 3.5 Procedure Used to Measure Flow Angles

When measuring velocities and flow angles, the probe was positioned in the tunnel so that the origin of the body coordinate system,  $x_B, y_B, z_B$  (Figure 16), was located at the grid point at which measurements were to be taken. For all of the current measurements, the probe orientation angles,  $\psi, \theta$  and  $\phi$ , were set at  $180.0^\circ, -1.0^\circ$  and  $0.0^\circ$  respectively (Figure 16). The probe vertical movement was restricted by the brake (at the top of the mechanism) and by the stepping motor (at the bottom of the mechanism) and it was necessary to set  $\theta$  at  $-1.0^\circ$  to enable measurements to be taken at both the upper and lower grid points at given  $y_T$  locations.

To determine  $V_y, \theta_y$  and  $\phi_y$  (Figure 16), it was first necessary to measure probe pressures,  $p_1$  to  $p_6$ . These pressures were measured using the same electronic manometer system and data sampling format that were used to measure the pressures for the mean velocities, as described in Section 2.4. However, for the flow angle



measurements, a PSI Electronic Pressure Scanner having a full-scale range of  $\pm 2490$  Pa ( $\pm 10.0$  inches of water) was used.

Once  $p_1$  to  $p_6$  had been measured,  $V_y$ ,  $\theta_y$  and  $\phi_y$  were determined using the probe calibration (equations 7 to 13). As indicated in Section 3.2, the calibration relationships do not give  $V_y$ ,  $\theta_y$  and  $\phi_y$  explicitly in terms of measured pressures,  $p_1$  to  $p_6$ , and it was necessary to determine the three variables iteratively. The following procedure was used.

1. As a first approximation, the value of  $V_y$  was set below its known value (e.g.  $V_y$  was initially set at 27 m/s when the free-stream velocity at which the measurements were taken was known to be about 30 m/s).
2. Using this first approximation of  $V_y$ , first approximations of  $C_{p_n}$  ( $n = 1$  to 4),  $R$  and  $\theta_y$  were made using equations 10, 9 and 7 (or 8) respectively.
3. Using the first approximation of  $\theta_y$ , a second approximation of  $V_y$  was made using equation 11 (or 12).
4. Successive approximations of  $V_y$  were made and steps 1 to 3 were repeated until the velocities converged to within 0.001 m/s. At this stage,  $V_y$ ,  $\theta_y$ ,  $C_{p_1}$ ,  $C_{p_2}$ ,  $C_{p_3}$  and  $C_{p_4}$  were determined to an acceptable accuracy.
5. Once values of  $C_p$  were known,  $\phi_y$  was calculated using equation 13.

$V_y$  was resolved into  $\bar{U}_B$ ,  $\bar{V}_B$  and  $\bar{W}_B$ , the components of velocity in the  $x_B$ ,  $y_B$  and  $z_B$  directions respectively in the body coordinate system, and these velocities were transposed, using equation 14, into  $\bar{U}_T$ ,  $\bar{V}_T$  and  $\bar{W}_T$ , the components of velocity in the  $x_T$ ,  $y_T$  and  $z_T$  directions respectively in the tunnel coordinate system. Horizontal and vertical flow angles,  $\epsilon_H$  and  $\epsilon_V$  respectively, relative to the  $x_T$  axis as shown in Figure 21, were then calculated. All iterative calculations and data reduction were carried out using the program ANGLE located on a PC.

### 3.6 Corrections to Flow Angles to Allow for Probe Support Interference

The traversing mechanism used to position the six-hole probe in the tunnel when measuring flow angles was made to be reasonably rigid (Figures 17 and 18). The vertical column on the mechanism is 46 mm wide and extends from the floor to the roof of the test section, so that the ratio of the cross-sectional area of the column to the total transverse cross-sectional area of the test section is 0.019:1, i.e. 1.9%. Although such a value of blockage is significantly less than the value 7.5%, quoted in Reference 9 as being the upper limit of blockage acceptable for wind-tunnel testing, interference caused by the column nevertheless had a noticeable effect on measured flow angles. When the six-hole probe was supported on the port side of the vertical column, flow angles measured at given  $z_T$  locations on the vertical centreplane in the test section were



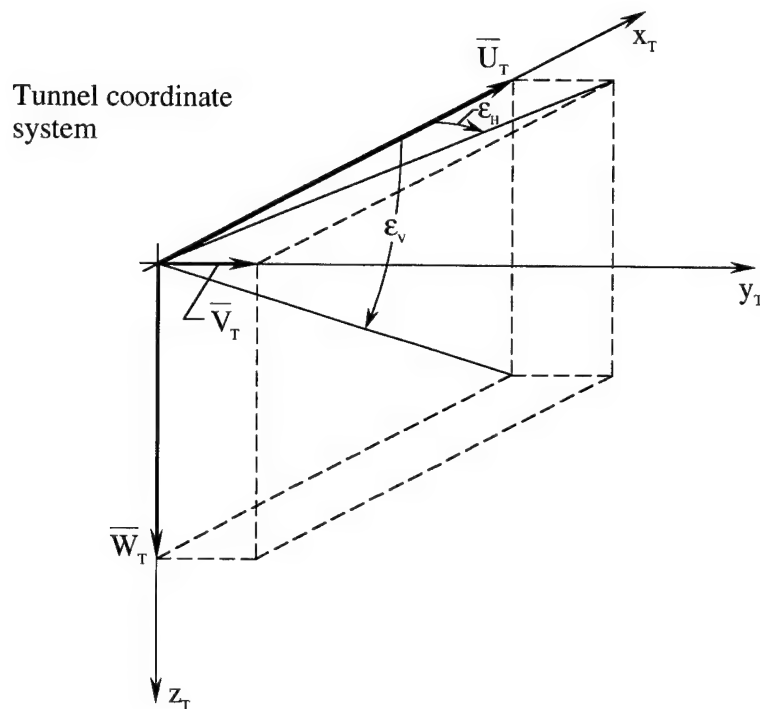


Figure 21. Velocities and flow angles in the tunnel coordinate system.

found to be noticeably different (see below) from those measured at the same locations when the probe was supported on the starboard side of the vertical column. Note that the vertical column on the traversing mechanism had to be moved from one side of the test section to the other side to obtain the two sets of measurements.

Experiments were undertaken to determine the corrections to be applied to measured flow angles to allow for the effects of the interference caused by the traversing mechanism. To determine a typical interference correction, the six-hole probe was mounted in a specially-designed thin supporting column (width of thin column is 16 mm), so that the tip of the probe was directly upstream of the column and the probe yaw, pitch and roll angles were set close to their values for normal operation. Flow angles were then measured for  $\bar{U}_{\text{NOM}} = 30$  and 60 m/s. The traversing mechanism was not in the test section for these measurements. The traversing mechanism was then positioned in the test section on either the port side of the probe or on the starboard side of the probe, but not actually attached to the probe, and flow angles were measured again. The vertical column on the traversing mechanism was located at the same lateral distance from the probe as it would be during normal operation, when the probe was attached to the mechanism. A typical experimental setup is shown in Figure 22 for the case when the thin column and the traversing mechanism are both in the test section. The interference corrections were then determined as the differences in corresponding

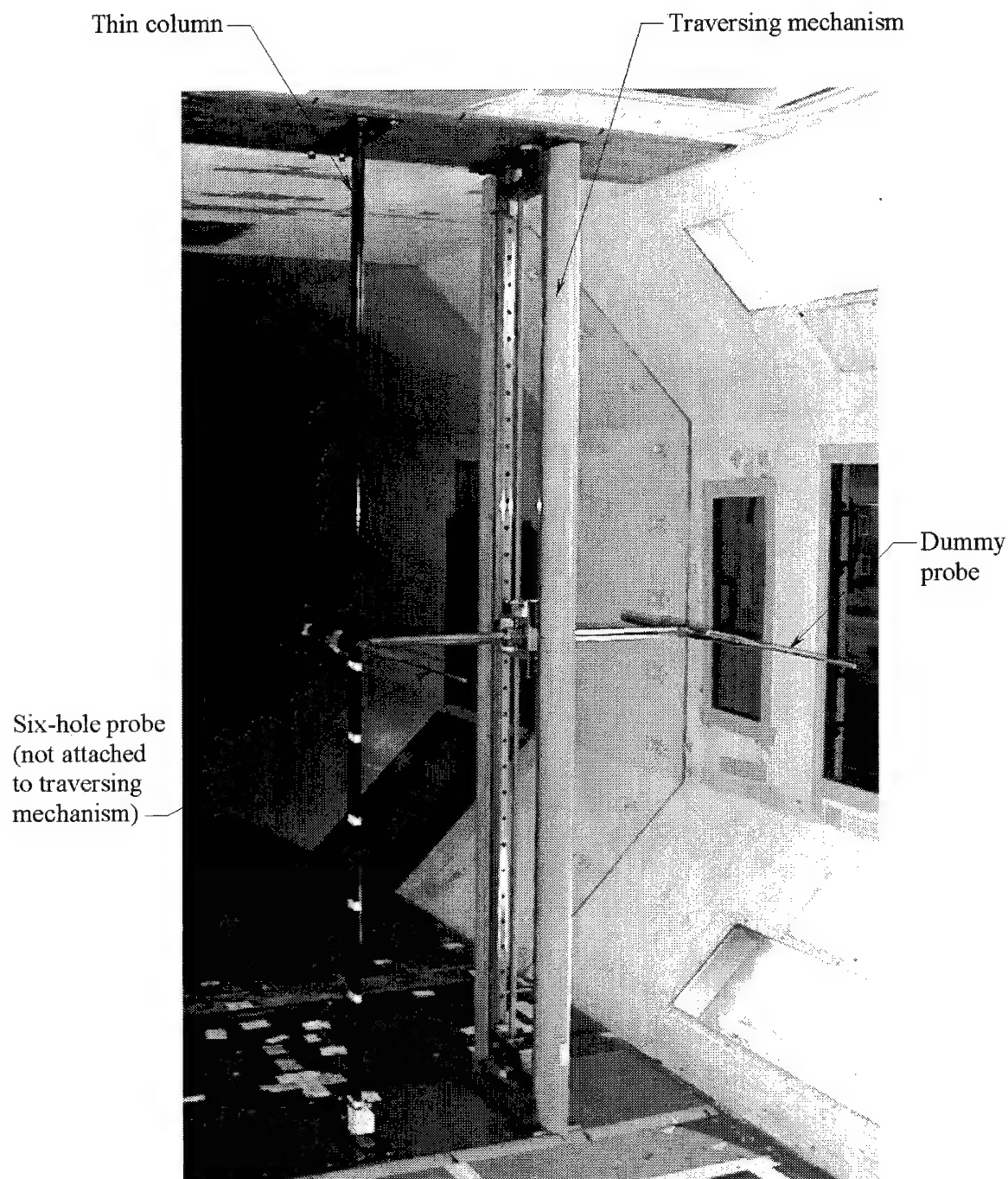


Figure 22. Traversing mechanism and thin column (supporting the six-hole probe) mounted in the test section of the low-speed wind tunnel.

flow angles measured both with the traversing mechanism in the tunnel and with the mechanism out of the tunnel.

When the six-hole probe was mounted on the thin column to assess probe support interference, it did not have to be set precisely at the yaw, pitch and roll angles used when the probe was attached to the traversing mechanism during normal operation. When determining interference corrections, the important measurements were the differences in flow angles measured when the traversing mechanism was in the tunnel and when it was not in the tunnel, rather than the absolute values of flow angles.

Interference corrections were determined in the  $x_T = 0.0$  m transverse plane of the test section for  $y_T/W = 0.0, \pm 0.15$  and  $\pm 0.3$ , and  $z_T/H = 0.0$  and  $\pm 0.3$ , where  $W = 2743$  mm and  $H = 2134$  mm are the width and height respectively of the test section of the LSWT (Figure 2). It was necessary to use three different thin supporting columns to support the six-hole probe at the three different  $z_T$  locations in the test section. The three columns were essentially the same, but had the probe attachment sleeve located at a different height ( $z_T$  location). Altogether, interference corrections were obtained for 15 locations, and corrections at other locations at which flow angles were measured were obtained by linear interpolation. The interference corrections varied depending on the location in the test section. For  $\bar{U}_{\text{NOM}} = 30$  and 60 m/s, average values of corrections for  $\epsilon_H$  were about  $0.4^\circ$  and those for  $\epsilon_V$  were about  $0.0^\circ$ . The corrections determined for the  $x_T = 0.0$  m transverse plane were applied to flow angles measured in this plane as well as in the  $x_T = -1.0$  and  $1.0$  m transverse planes. The overlapping results at the vertical centreplane were effectively the same after the corrections had been applied.

### 3.7 Analysis of Flow Angles

Contours of  $\epsilon_H$  for  $\bar{U}_{\text{NOM}} = 30$  m/s for  $x_T = -1.0, 0.0$  and  $1.0$  m are shown in Figure 23. Corresponding plots for  $\epsilon_V$  are shown in Figure 24. The corresponding  $\epsilon_H$  and  $\epsilon_V$  plots for  $\bar{U}_{\text{NOM}} = 60$  m/s are shown in Figures 25 and 26 respectively. As for the mean velocities, Figures 23 to 26 each indicate how the flow angles change as the flow moves downstream. For the two values of  $\bar{U}_{\text{NOM}}$ , the general pattern of the  $\epsilon_H$  contours at the three  $x_T$  locations is similar (Figures 23 and 25), with little evidence of the flow becoming more uniform as it moves downstream, and likewise for the corresponding  $\epsilon_V$  contours (Figures 24 and 26). In the central 50% of the cross-sectional area of the test section, between  $x_T = -1.0$  and  $+1.0$  m, for  $\bar{U}_{\text{NOM}} = 30$  m/s, horizontal flow angles varied from  $-0.8^\circ$  to  $+0.6^\circ$  (Figure 23) and vertical flow angles varied from  $-0.8^\circ$  to  $+0.4^\circ$  (Figure 24). For  $\bar{U}_{\text{NOM}} = 60$  m/s, horizontal flow angles varied from  $-0.4^\circ$  to  $+0.8^\circ$  (Figure 25) and vertical flow angles varied from  $-1.0^\circ$  to  $+0.4^\circ$  (Figure 26). There is a pocket of flow in the lower starboard corner of the test section which has significantly larger values of vertical flow angles which range up to  $-1.4^\circ$  (Figure 26). Figures 23 and 24, for  $\bar{U}_{\text{NOM}} = 30$  m/s, and Figures 25 and 26, for  $\bar{U}_{\text{NOM}} = 60$  m/s, indicate that regions of high or low horizontal flow angles are not necessarily associated with corresponding regions of high or low vertical flow angles.

Selected data associated with the contours shown in Figures 23 to 26 have been replotted in Figure 27 to indicate how horizontal and vertical flow angles in the horizontal and vertical centreplanes vary in the longitudinal or  $x_T$  direction. The method of plotting the data is similar to that used in Section 2.5 for the mean velocities. Data corresponding to the  $x_T$ - $z_T$  plane that passes through  $y_T = 0.0$  m (i.e. the vertical plane that is aligned with and passes through the tunnel longitudinal axis) are shown for  $z_T/H = 0.0, \pm 0.2$  and  $\pm 0.4$ . Similarly, data corresponding to the  $x_T$ - $y_T$  plane that passes through  $z_T = 0.0$  m (i.e. the horizontal plane that is aligned with and passes through the tunnel longitudinal axis) are shown for  $y_T/W = 0.0, \pm 0.15, \pm 0.30$  and  $\pm 0.45$ . In Figure 27, data corresponding to the longitudinal centreline of the tunnel are represented by thick lines. Horizontal and vertical flow angles for the chosen locations remain approximately constant over the  $x_T$  range, except sometimes for locations near the sides of the test section of the tunnel, where  $y_T/W = +0.45$  (Figure 27 b-d).

### 3.8 Errors in Measured Flow Angles

There are small errors in the measured horizontal and vertical flow angles,  $\epsilon_H$  and  $\epsilon_V$  respectively, due to (1) instrumentation errors and (2) probe setup errors. The probe setup errors occur because the six-hole probe is not set at precisely the required yaw, pitch and roll angles, relative to the tunnel coordinate system, when measuring flow angles.

#### 3.8.1 Instrumentation Errors

Considering firstly instrumentation errors, it was necessary to measure air temperatures and air pressures when determining flow angles. The sensing devices used to measure temperatures were only accurate to within  $\pm 0.5^\circ$  C and the indicated readings of the scanners used to measure the pressures were only accurate to within  $\pm 0.05\%$  of their full-scale reading. Two different types of scanners were used when measuring pressures to determine flow angles and their ranges were 159 kPa (23.0 psi) and  $\pm 2490$  Pa ( $\pm 10.0$  inches of water). The possible errors in measured values of  $\epsilon_H$  and  $\epsilon_V$  corresponding to these instrumentation errors were determined. For  $\bar{U}_{\text{NOM}} = 30$  m/s, errors in  $\epsilon_H$  were about  $\pm 0.08^\circ$  and errors in  $\epsilon_V$  were about  $\pm 0.08^\circ$ . Corresponding errors for  $\bar{U}_{\text{NOM}} = 60$  m/s were about  $\pm 0.02^\circ$  for  $\epsilon_H$  and about  $\pm 0.02^\circ$  for  $\epsilon_V$ .

#### 3.8.2 Probe Setup Errors

Considering probe setup errors, it is indicated in Section 3.4 that the possible errors in setting the yaw, pitch and roll angles of the six-hole probe are  $\pm 0.02^\circ$ ,  $\pm 0.02^\circ$  and  $\pm 0.2^\circ$  respectively. The  $\pm 0.02^\circ$  probe setup error given for the yaw angle corresponds to the possible misalignment of the probe relative to the traversing mechanism, and not the misalignment of the probe relative to the tunnel. It is also indicated in Section 3.4 that an additional error of  $\pm 0.1^\circ$  in probe yaw angle may exist since the traversing mechanism itself can only be set to an accuracy of  $0.1^\circ$  in yaw angle, due to difficulties

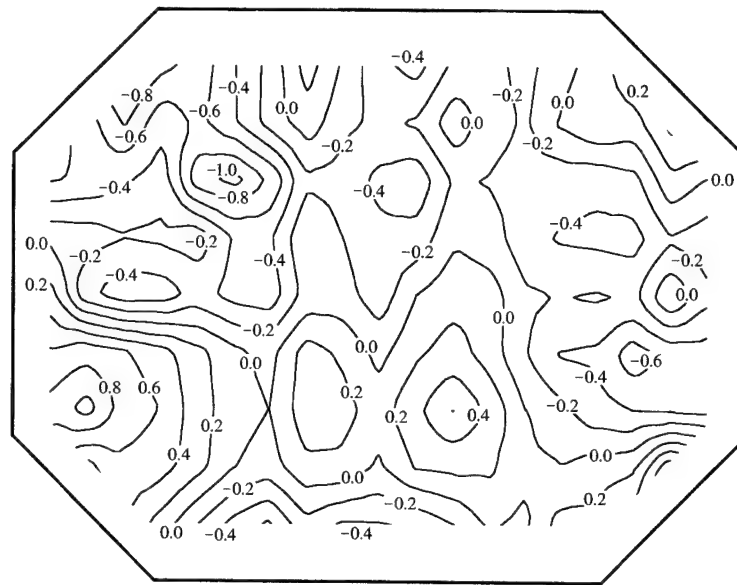
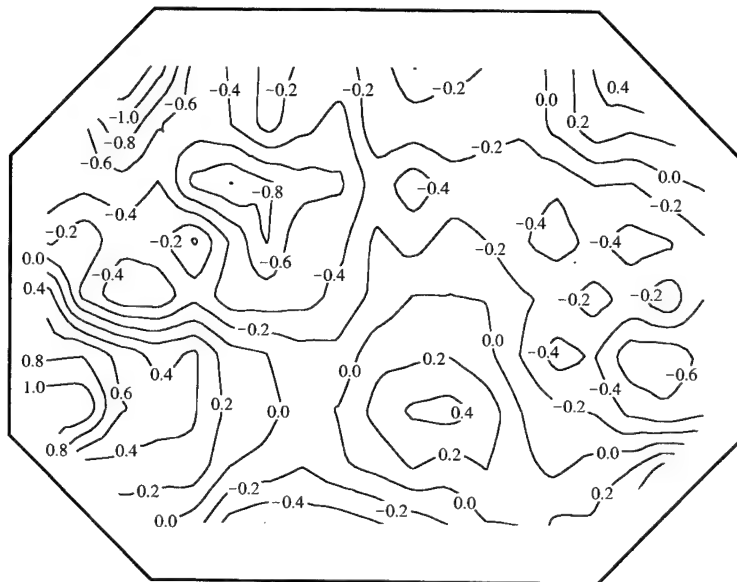
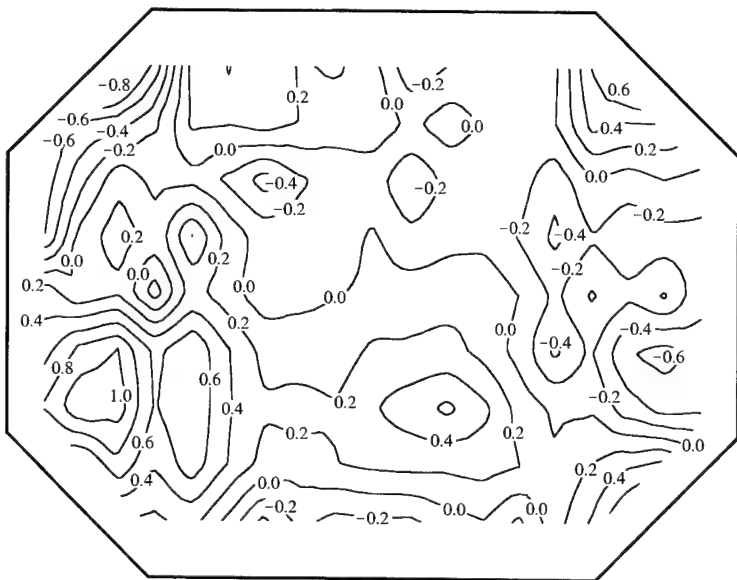
 $\epsilon_H$  deg $\bar{U}_{\text{NOM}} = 30$  m/s $x_T = -1.0$  m $\epsilon_H$  deg $\bar{U}_{\text{NOM}} = 30$  m/s $x_T = 0.0$  m $\epsilon_H$  deg $\bar{U}_{\text{NOM}} = 30$  m/s $x_T = 1.0$  m

Figure 23. Contours of horizontal flow angle for  $\bar{U}_{\text{NOM}} = 30$  m/s for  $x_T = -1.0, 0.0$  and  $1.0$  m.

The flow is out of the page.

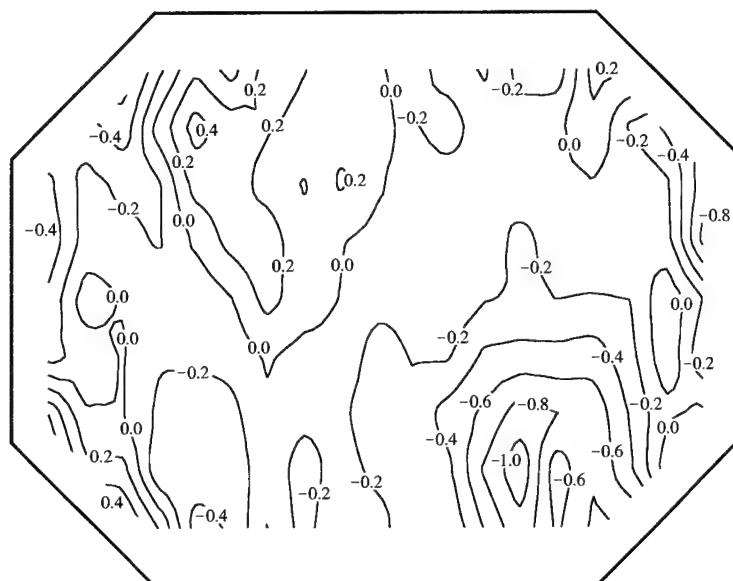
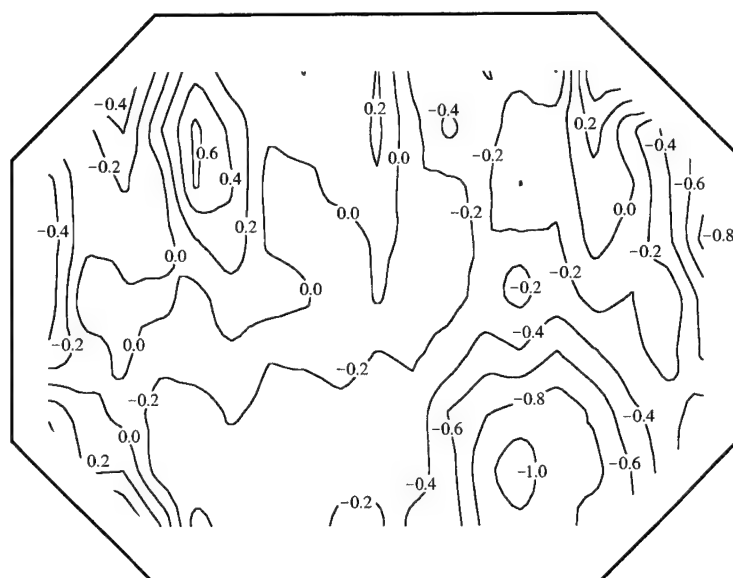
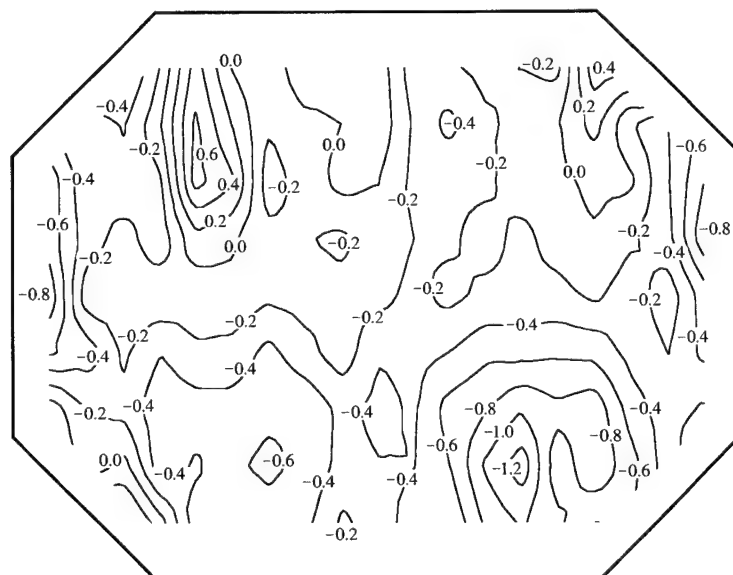
 $\epsilon_v$  deg $\bar{U}_{\text{NOM}} = 30$  m/s $x_T = -1.0$  m $\epsilon_v$  deg $\bar{U}_{\text{NOM}} = 30$  m/s $x_T = 0.0$  m $\epsilon_v$  deg $\bar{U}_{\text{NOM}} = 30$  m/s $x_T = 1.0$  m

Figure 24. Contours of vertical flow angle for  $\bar{U}_{\text{NOM}} = 30$  m/s for  $x_T = -1.0, 0.0$  and  $1.0$  m.

The flow is out of the page.

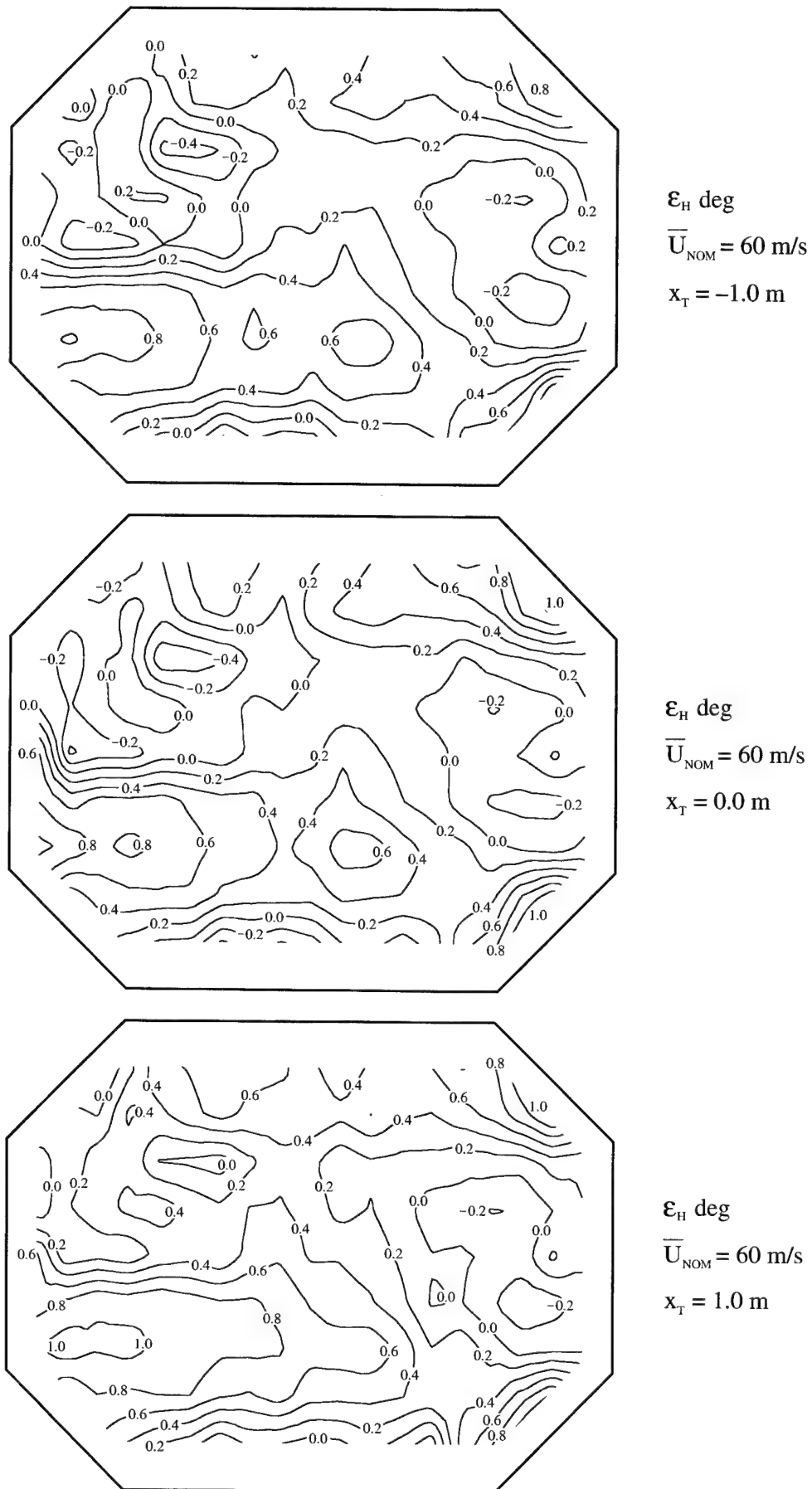


Figure 25. Contours of horizontal flow angle for  $\bar{U}_{\text{NOM}} = 60 \text{ m/s}$  for  $x_T = -1.0, 0.0$  and  $1.0 \text{ m}$ .

The flow is out of the page.

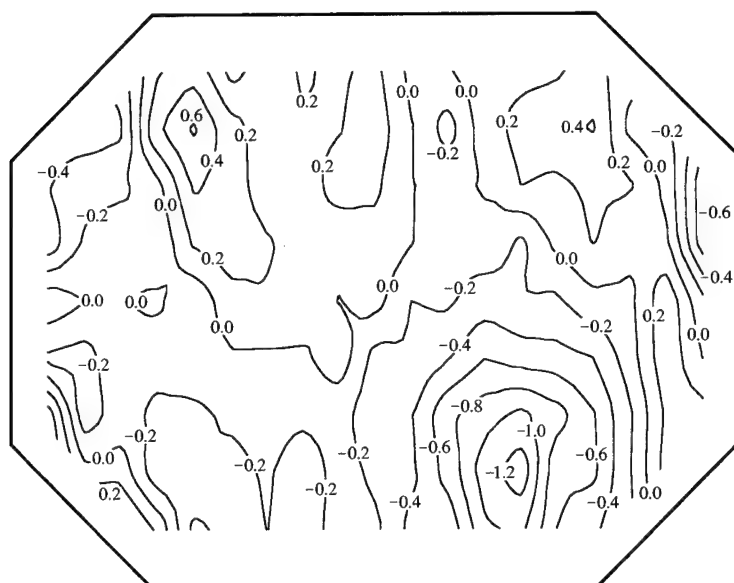
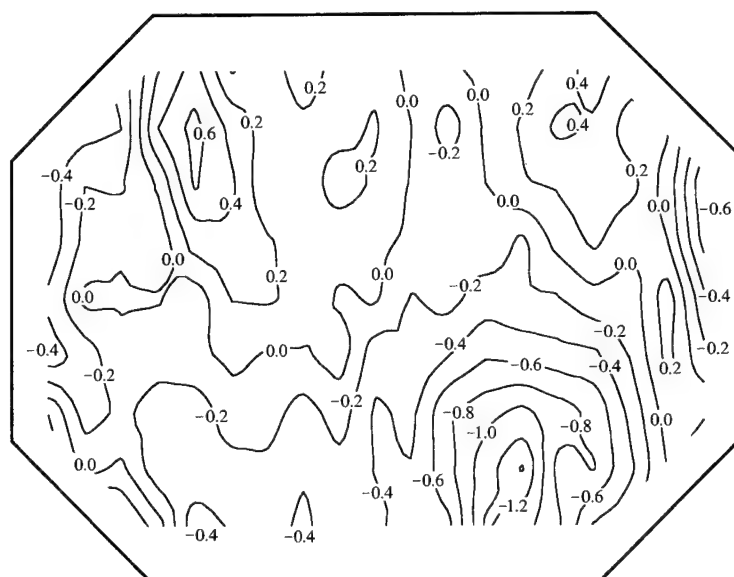
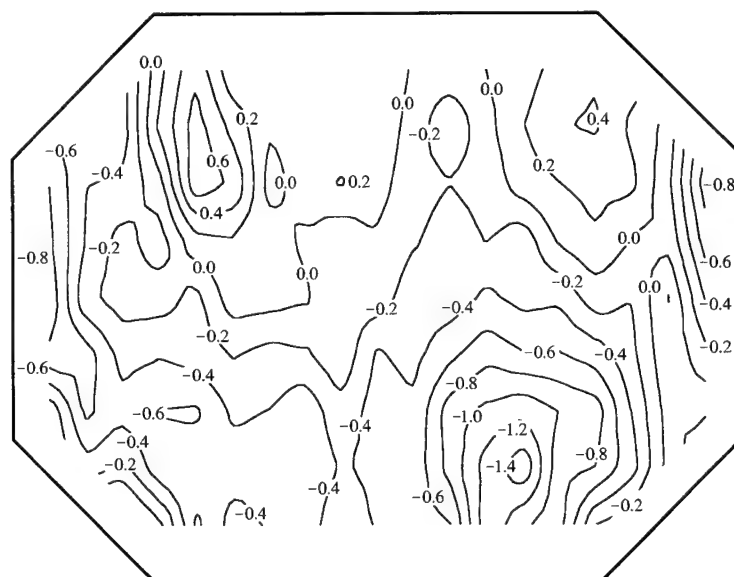
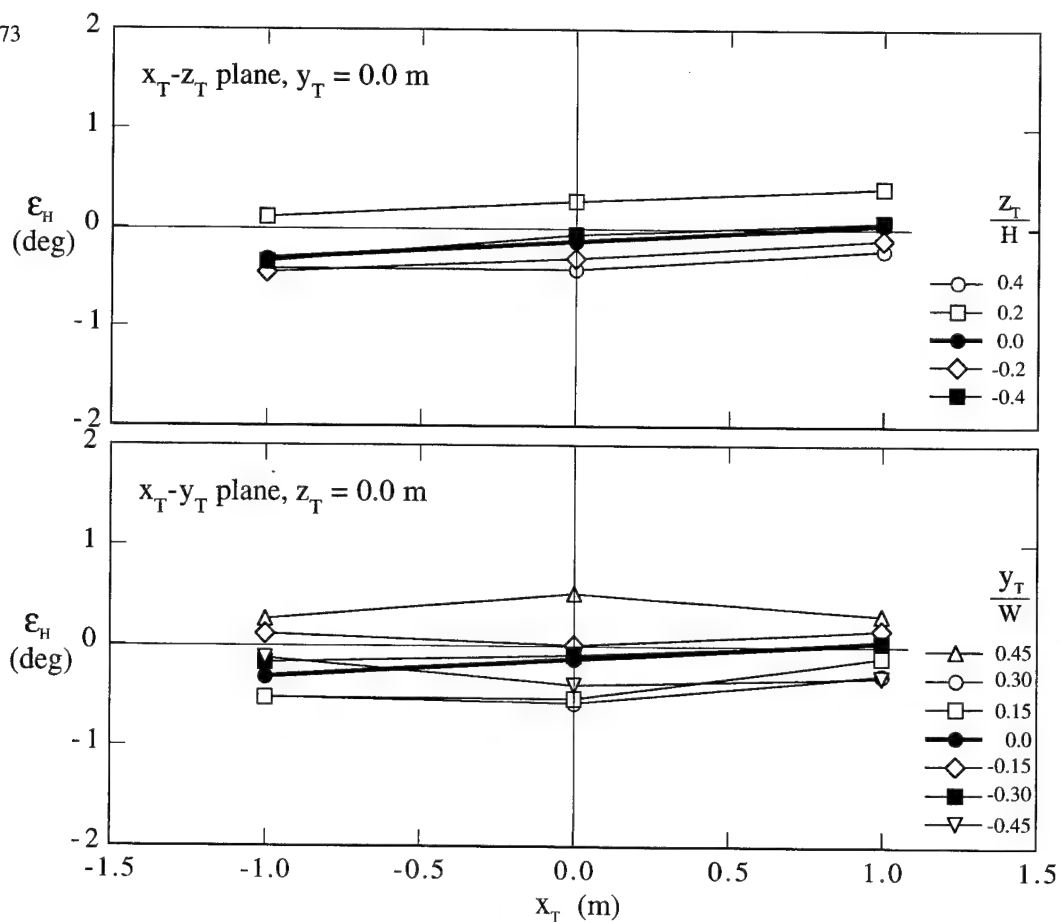
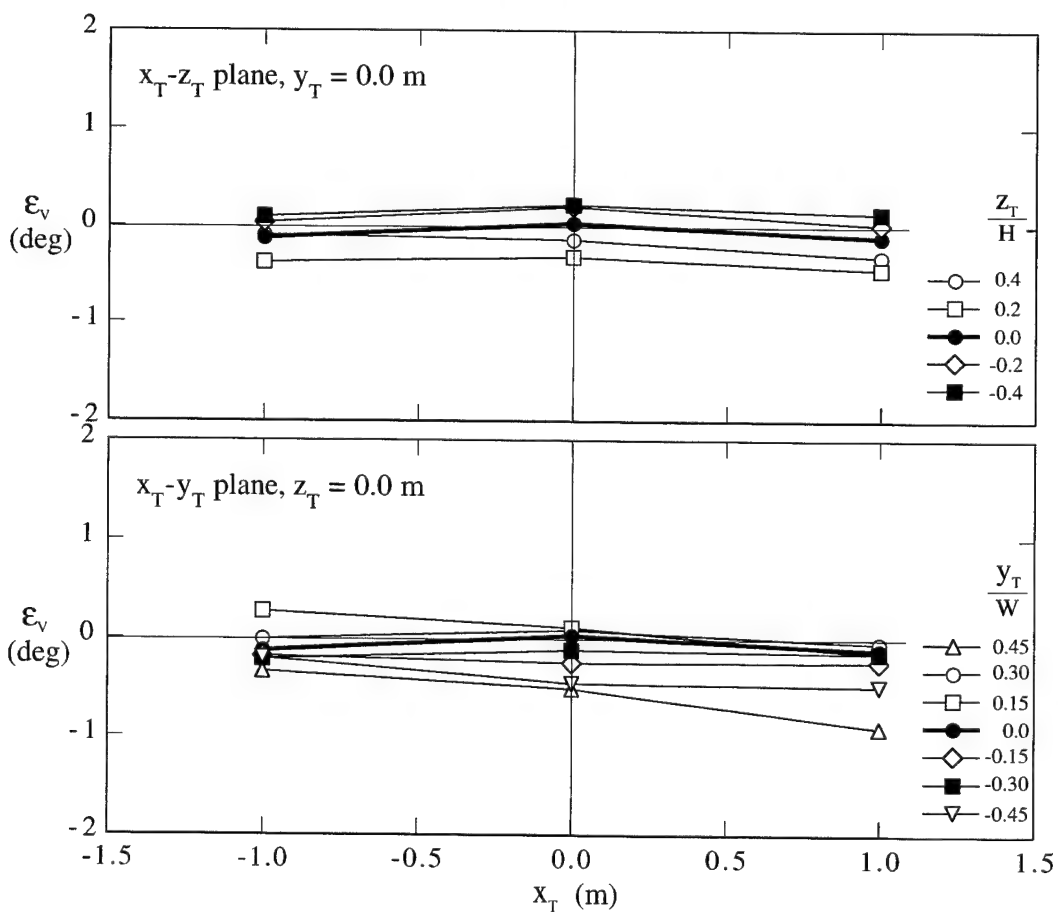
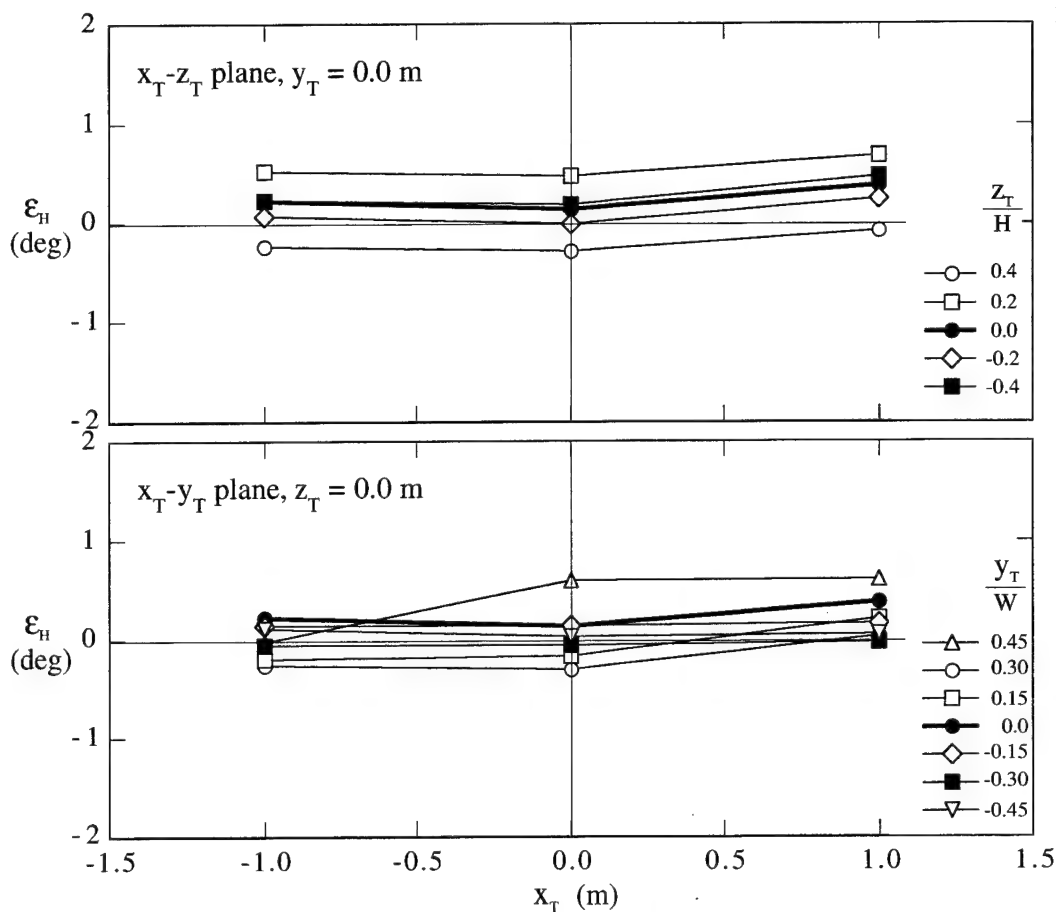
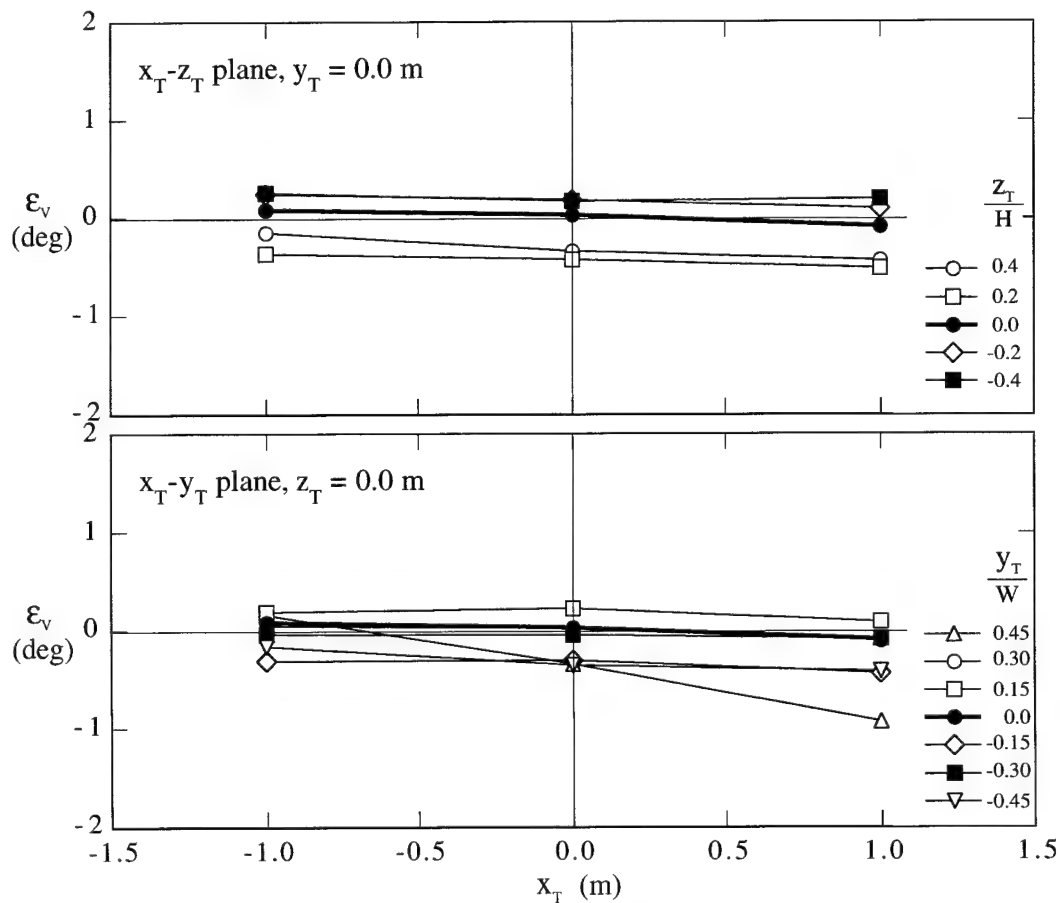
 $\epsilon_v$  deg $\bar{U}_{\text{NOM}} = 60$  m/s $x_T = -1.0$  m $\epsilon_v$  deg $\bar{U}_{\text{NOM}} = 60$  m/s $x_T = 0.0$  m $\epsilon_v$  deg $\bar{U}_{\text{NOM}} = 60$  m/s $x_T = 1.0$  m

Figure 26. Contours of vertical flow angle for  $\bar{U}_{\text{NOM}} = 60$  m/s for  $x_T = -1.0, 0.0$  and  $1.0$  m.

The flow is out of the page.



(a) Horizontal flow angles,  $\bar{U}_{NOM} = 30$  m/s.(b) Vertical flow angles,  $\bar{U}_{NOM} = 30$  m/s.Figure 27. Horizontal and vertical flow angles in the  $x_T$  direction for  $\bar{U}_{NOM} = 30$  and 60 m/s.

(c) Horizontal flow angles,  $\bar{U}_{NOM} = 60$  m/s.(d) Vertical flow angles,  $\bar{U}_{NOM} = 60$  m/s.

in accurately positioning the lower plate which is used to align the mechanism. It is further indicated that an additional error of  $\pm 0.1^\circ$  in probe yaw angle may exist due to possible twisting of the mechanism relative to the lower plate, resulting from imperfect manufacture and assembly of the mechanism. Possible errors in measured values of  $\epsilon_h$  and  $\epsilon_v$  corresponding to the probe setup errors given above were determined. It was found that errors in  $\epsilon_h$  were about  $\pm 0.02^\circ$  and errors in  $\epsilon_v$  were about  $\pm 0.05^\circ$ . The setup error of  $\pm 0.1^\circ$  in probe yaw angle, due to the positioning the lower plate, results in an  $0.1^\circ$  increase or decrease in the possible error in  $\epsilon_h$ , and similarly for the setup error of  $0.1^\circ$  in probe yaw angle due to the twisting of the mechanism. These latter two setup errors in yaw angle have negligible effect on errors in measured values of  $\epsilon_v$ .

### 3.8.3 Accumulation of Errors

All possible errors in  $\epsilon_h$  and  $\epsilon_v$  given above are additive. However, since the lower plate is not moved during any set of measurements at a given  $x_T$  location, any errors due to the positioning of the lower plate will affect all measured values of  $\epsilon_h$  equally at that  $x_T$  location, i. e. all measured values of  $\epsilon_h$  for a particular cross section of the flow may be high or low by up to  $0.1^\circ$  due to this effect. Similarly, since the traversing mechanism was not dismantled after initial assembly, any errors due to the twisting of the mechanism will affect all measured values of  $\epsilon_h$  equally for the entire set of angle measurements, i. e. all measured values of  $\epsilon_h$  for the entire experimental program may be high or low by up to an additional  $0.1^\circ$ .

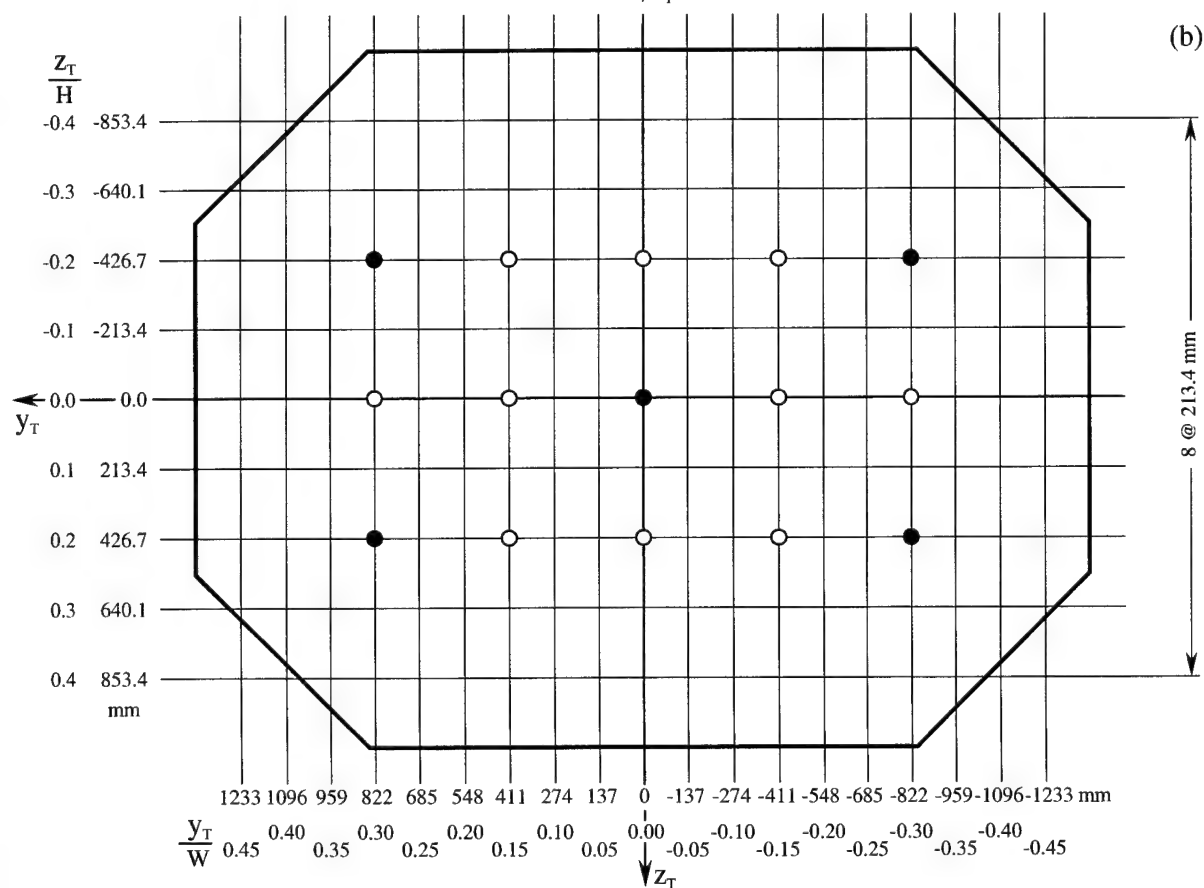
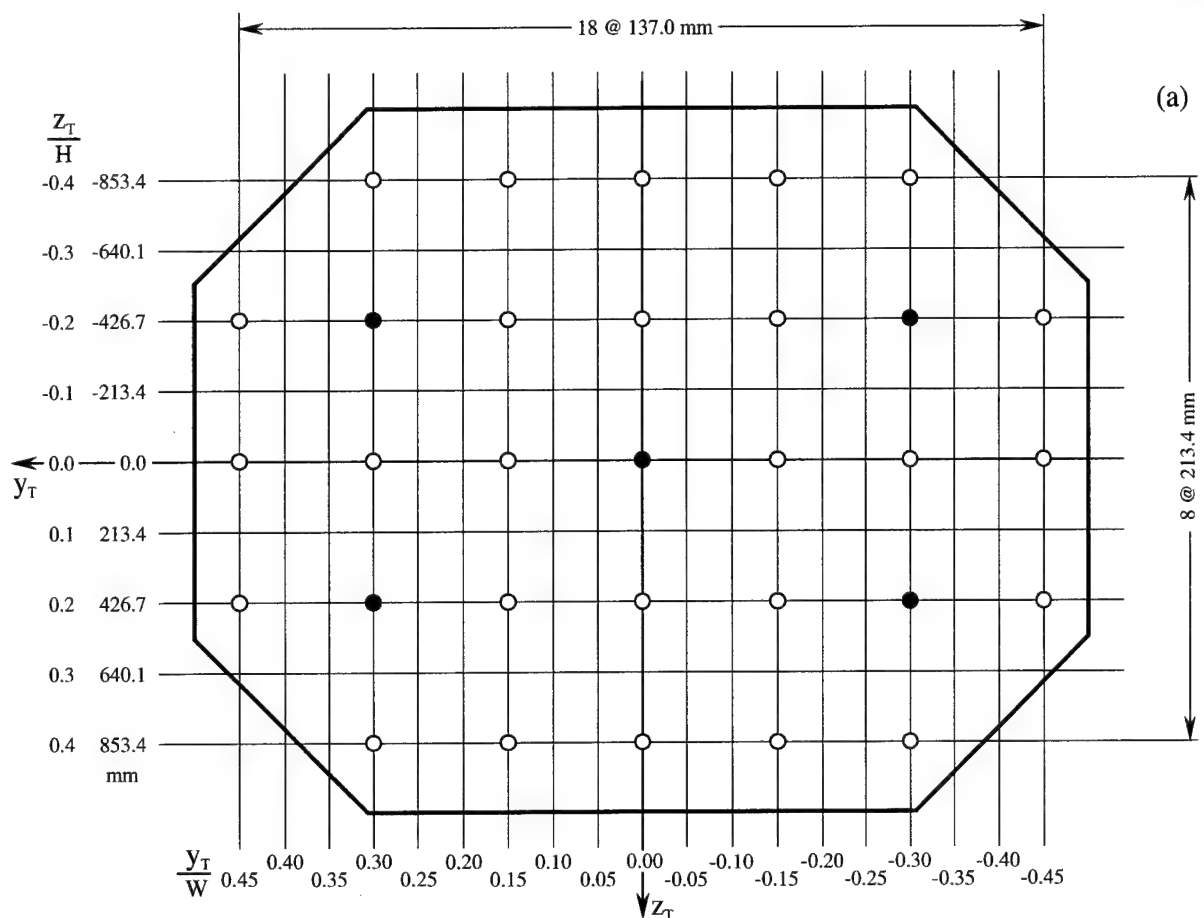
## 4. Turbulence-Intensity Measurements

### 4.1 Test Schedule

Turbulence intensities,  $(\overline{u^2})^{0.5}/\overline{U}_{0.0}$ ,  $(\overline{v^2})^{0.5}/\overline{U}_{0.0}$  and  $(\overline{w^2})^{0.5}/\overline{U}_{0.0}$ , were measured in the test section at the 31 grid points shown in Figure 28 (a) for  $x_T = 0.0$  m as well as at the 15 grid points shown in Figure 28 (b) for  $x_T = -1.0$  and  $1.0$  m. Intensities were measured for  $\overline{U}_{\text{NOM}} = 30$  and  $60$  m/s. The symbols  $u$ ,  $v$  and  $w$  denote the fluctuating components of velocity in the  $x_T$ ,  $y_T$  and  $z_T$  directions respectively. (Note that in a fluctuating flow,  $U$ , the instantaneous velocity in the  $x_T$  direction, is related to the mean and fluctuating components of velocity in that direction by  $U = \overline{U} + u$ , and likewise for the  $y_T$  and  $z_T$  directions).

### 4.2 Modified Cross-Tunnel Rake

For the intensity measurements, the cross-tunnel rake (Section 2.3) was modified by removing some of the pressure probes and replacing them with posts, which were used to attach a hot-wire probe.



The flow and the  $x_T$  axis are out of the page

Figure 28. Grid points at which turbulence intensities (unfilled plus filled circles) and spectra (filled circles) were measured. (a)  $x_T = 0.0$  m, (b)  $x_T = -1.0$  and  $1.0$  m.

### 4.3 Procedure Used to Measure Turbulence Intensities

The turbulence intensities were measured using the AMRL constant-temperature hot-wire anemometer system described in Reference 10. The system includes four anemometers, a matching box, a dynamic calibrator, four low-pass filters, a data-acquisition system (based on a PC) and software for calibrating the hot wires and for acquiring and reducing the data. For the current measurements, a DANTEC<sup>2</sup> 55P51 crossed-wire probe and corresponding leads were used, but the platinum-plated tungsten wires on the probe were removed and replaced with Wollaston wires. Although platinum-plated tungsten wires are stronger, Wollaston wires were used because the existing hot-wire anemometers had been optimized for use with this type of wire. Wollaston wires also have a more stable temperature calibration than platinum-plated tungsten wires (see Reference 10).

The procedures used to replace the hot wires, set the operating resistances of the wires, set the frequency responses of the anemometers, electronically match the wires, calibrate the wires using the dynamic calibrator, sample the wire voltages using the data-acquisition system and reduce the data to obtain the required turbulence terms, are described in Reference 10.

On the modified cross-tunnel rake (Section 4.2), only one hot-wire probe was used for the intensity measurements and it was necessary to roll the probe on its post or move the probe from post to post to enable the complete set of measurements to be taken. After measuring intensities for the  $u$  and  $v$  components of the turbulence, the probe was rolled  $90^\circ$  to measure intensities for the  $u$  and  $w$  components of the turbulence. At each probe location, the  $u$ -component intensities were determined by averaging the two measured intensities corresponding to the two roll angles of the probe. The difference between the results for the two roll angles was small for  $\bar{U}_{\text{NOM}} = 30$  and  $60$  m/s, being typically of the order of 0.02 and 0.06 percentage points respectively. The tunnel had to be stopped each time the probe was rolled or relocated. It would have been preferable to use the traversing mechanism (Section 3.4) to position the hot-wire probe to different  $z_r$  locations, but the mechanism had not been built when the intensities were measured.

When measuring intensities, each hot-wire voltage was sampled 30 000 times at a sampling frequency of 200 Hz and the low-pass filters were set at 10 kHz. These sampling parameters have been shown to be satisfactory for the measurement of intensities in the free-stream of the LSWT (Reference 10). Since the root-mean-square intensities were known to be much less than 10% at all locations in the flow, hot-wire non-linearity was neglected and intensities were evaluated by processing measured hot-wire voltages rather than by processing velocities determined from voltages (Reference 11). The hot wires were calibrated at both  $\bar{U}_{\text{NOM}} = 30$  and  $60$  m/s and hot-wire sensitivities were evaluated at these two velocities. The turbulence intensities were then determined using these sensitivities. Since sensitivities were only required at either  $\bar{U}_{\text{NOM}} = 30$  or  $60$  m/s,

<sup>2</sup> DANTEC Elektronik, Tonsbakken 16-18, DK-2740, Skovlunde, Denmark.

it was not necessary to carry out a complete dynamic calibration to obtain calibration equations covering a range of free-stream velocities.

For each position of the hot-wire probe, values of  $(\overline{u^2})^{0.5}$ ,  $(\overline{v^2})^{0.5}$  and  $(\overline{w^2})^{0.5}$  were measured and at the same time corresponding longitudinal mean velocities,  $\overline{U}$ , in the vicinity of the probe were also measured using total and static probes. In general, the measured values of  $\overline{U}$  varied slightly across the cross section. Turbulence intensities,  $(\overline{u^2})^{0.5}/\overline{U}$ ,  $(\overline{v^2})^{0.5}/\overline{U}$  and  $(\overline{w^2})^{0.5}/\overline{U}$ , were then computed at each point in the grid, using the appropriate value of  $\overline{U}$  for that location as the normalizing velocity. The calculated intensities were then corrected very slightly so that they were defined using  $\overline{U}_{0.0}$ , the mean velocity at the centre of the test section.

#### 4.4 Analysis of Turbulence Intensities

Contours of  $(\overline{u^2})^{0.5}/\overline{U}_{0.0}$  for  $\overline{U}_{\text{NOM}} = 30$  m/s at  $x_T = -1.0, 0.0$  and  $1.0$  m are shown in Figure 29. Corresponding plots for  $(\overline{v^2})^{0.5}/\overline{U}_{0.0}$  and  $(\overline{w^2})^{0.5}/\overline{U}_{0.0}$  are shown in Figures 30 and 31 respectively. Figures 32, 33 and 34 show contours for  $\overline{U}_{\text{NOM}} = 60$  m/s and these correspond to Figures 29, 30 and 31 respectively for  $\overline{U}_{\text{NOM}} = 30$  m/s. Each of Figures 29 to 34 have been plotted to indicate how the contours change as the flow moves downstream, i.e.  $x_T$  changes. For the two values of  $\overline{U}_{\text{NOM}}$ , the contours of  $(\overline{u^2})^{0.5}/\overline{U}_{0.0}$  at the three  $x_T$  locations (Figures 29 and 32) have the same general features, as far as it is possible to tell from the limited data at  $x_T = -1.0$  and  $1.0$  m, and likewise for the corresponding contours of  $(\overline{v^2})^{0.5}/\overline{U}_{0.0}$  (Figures 30 and 33 respectively) and  $(\overline{w^2})^{0.5}/\overline{U}_{0.0}$  (Figures 31 and 34 respectively). This indicates that regions of a given turbulence intensity are convected downstream with little lateral spreading and there does not appear to be any significant decay of the turbulence as the flow moves downstream. The most important result is the value of  $(\overline{u^2})^{0.5}/\overline{U}_{0.0}$ , which is a measure of the turbulence level in the tunnel. In the central 50% of the cross-sectional area of the test section, for  $\overline{U}_{\text{NOM}} = 30$  and  $60$  m/s,  $(\overline{u^2})^{0.5}/\overline{U}_{0.0}$  is generally below about 0.4%, at  $x_T = -1.0, 0.0$  and  $1.0$  m, whereas corresponding values of  $(\overline{v^2})^{0.5}/\overline{U}_{0.0}$  and  $(\overline{w^2})^{0.5}/\overline{U}_{0.0}$  are generally below about 0.7% (Figures 29 to 34). The strongest gradients of intensity occur on the starboard side of the test section where the intensities attain their maximum values.

Contours of  $(\overline{u^2})^{0.5}/\overline{U}_{0.0}$ ,  $(\overline{v^2})^{0.5}/\overline{U}_{0.0}$  and  $(\overline{w^2})^{0.5}/\overline{U}_{0.0}$  for  $x_T = 0.0$  m and  $\overline{U}_{\text{NOM}} = 30$  m/s are shown in Figure 35 to indicate the relationship between the three types of intensity at a fixed value of  $x_T$  and a fixed value of  $\overline{U}_{\text{NOM}}$ . Corresponding contours for  $\overline{U}_{\text{NOM}} = 60$  m/s are shown in Figure 36. For both values of  $\overline{U}_{\text{NOM}}$ , the general pattern of the contours for the three components of intensity is the same, but the intensity levels for the longitudinal (u) component of the turbulence are about two thirds those for the lateral (v and w) components. This non-isotropic behaviour is common in wind-tunnel flows since the longitudinal vorticity component is reduced and the lateral components are increased by the contraction (Reference 12).

A comparison of the results in Figures 35 and 36 indicates that corresponding intensities at  $x_T = 0.0$  m for  $\overline{U}_{\text{NOM}} = 30$  and  $60$  m/s are very similar, as for the mean velocities.

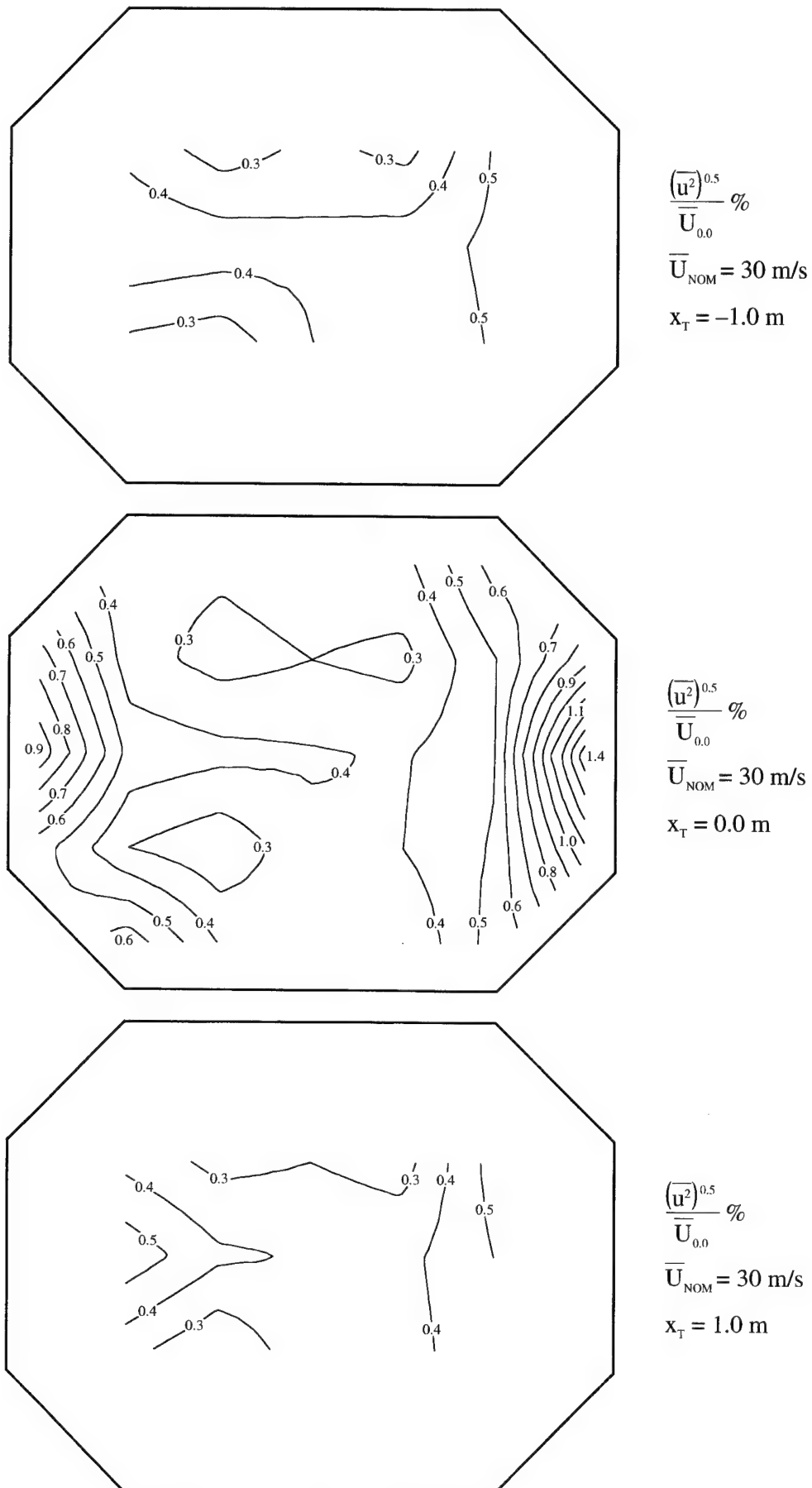
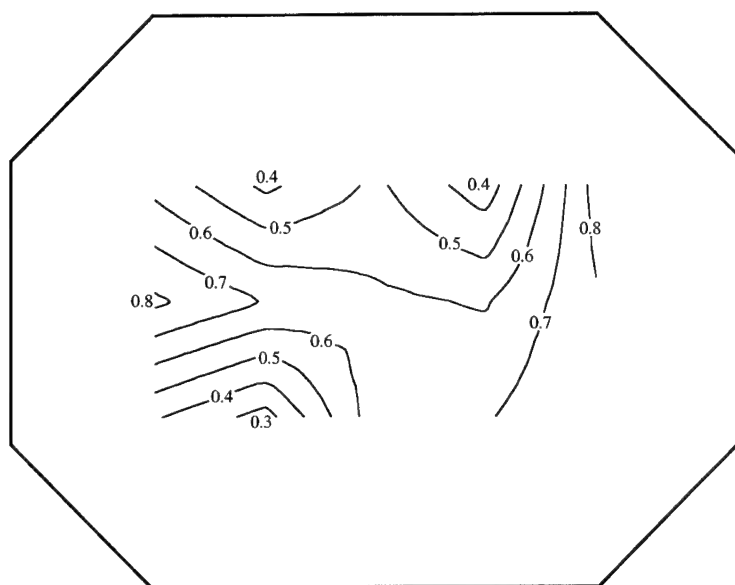


Figure 29. Contours of u-component intensity for  $\overline{U}_{\text{NOM}} = 30$  m/s for  $x_T = -1.0, 0.0$  and  $1.0$  m.

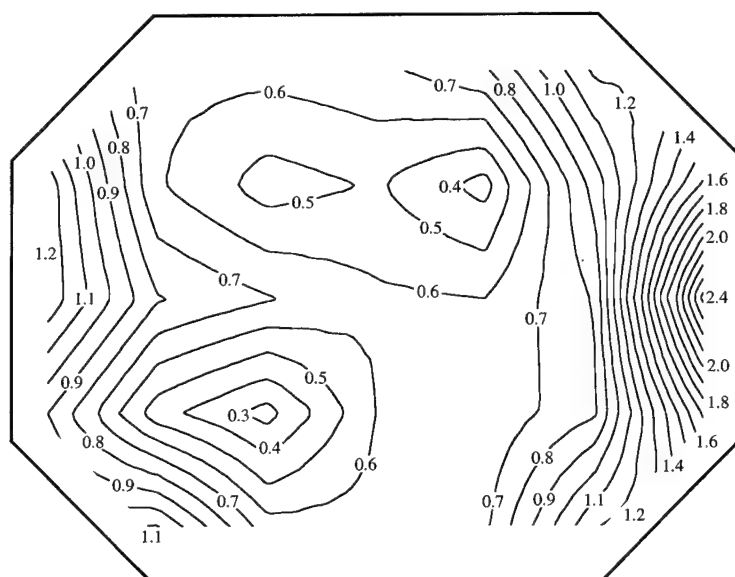
The flow is out of the page.



$$\frac{(\overline{v^2})^{0.5}}{\overline{U}_{0.0}} \%$$

$$\overline{U}_{\text{NOM}} = 30 \text{ m/s}$$

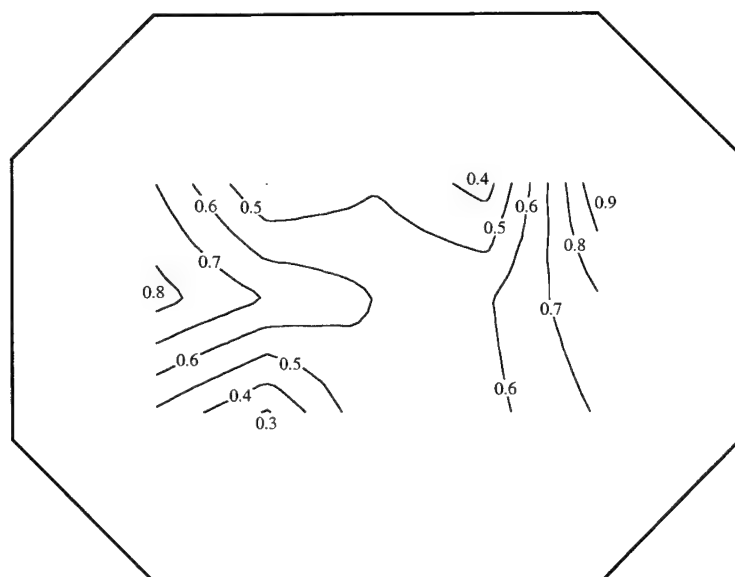
$$x_T = -1.0 \text{ m}$$



$$\frac{(\overline{v^2})^{0.5}}{\overline{U}_{0.0}} \%$$

$$\overline{U}_{\text{NOM}} = 30 \text{ m/s}$$

$$x_T = 0.0 \text{ m}$$



$$\frac{(\overline{v^2})^{0.5}}{\overline{U}_{0.0}} \%$$

$$\overline{U}_{\text{NOM}} = 30 \text{ m/s}$$

$$x_T = 1.0 \text{ m}$$

Figure 30. Contours of  $v$ -component intensity for  $\overline{U}_{\text{NOM}} = 30 \text{ m/s}$  for  $x_T = -1.0, 0.0$  and  $1.0 \text{ m}$ .

The flow is out of the page.



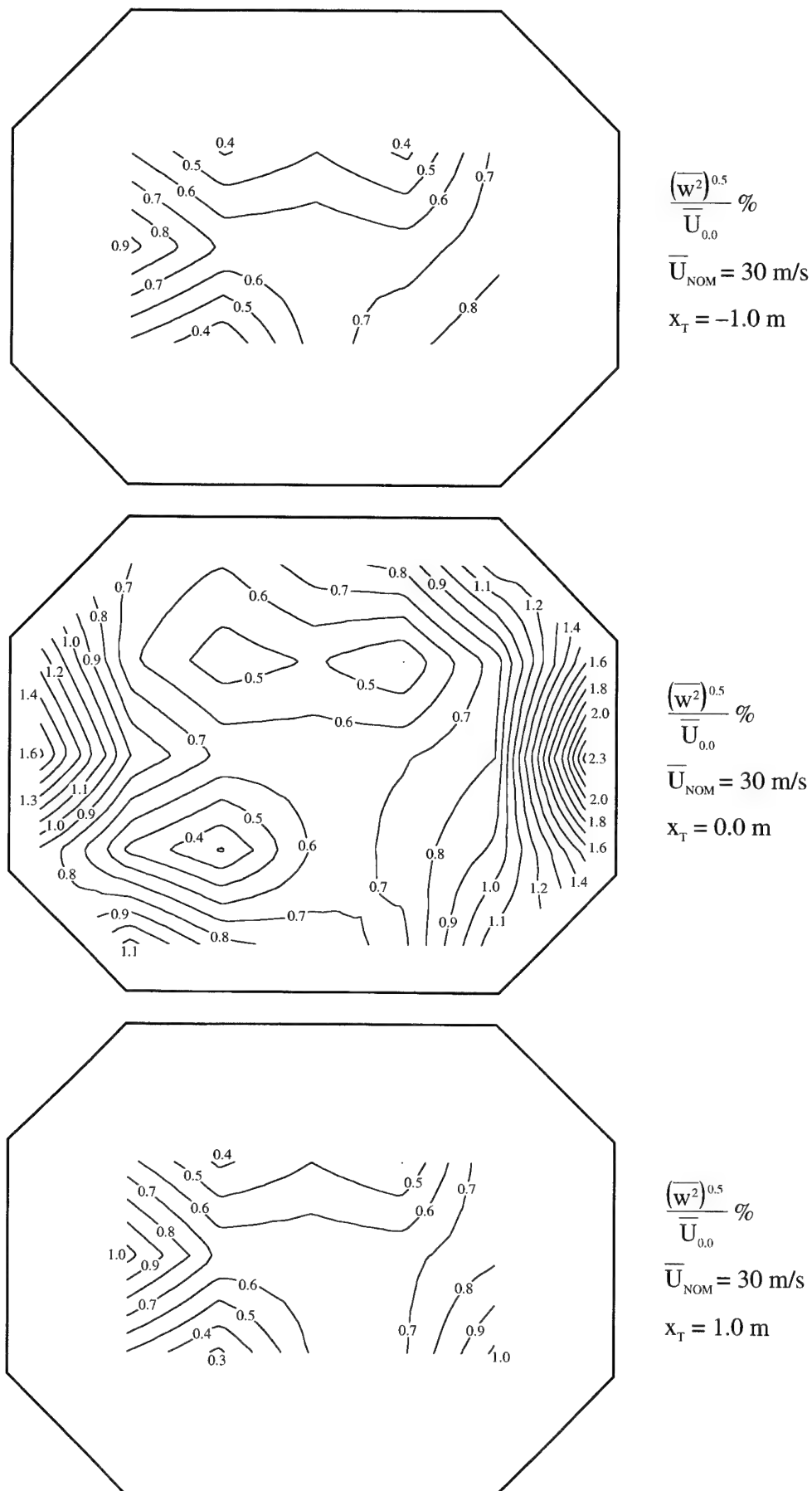


Figure 31. Contours of w-component intensity for  $\overline{U}_{\text{NOM}} = 30$  m/s for  $x_T = -1.0, 0.0$  and  $1.0$  m.

The flow is out of the page.

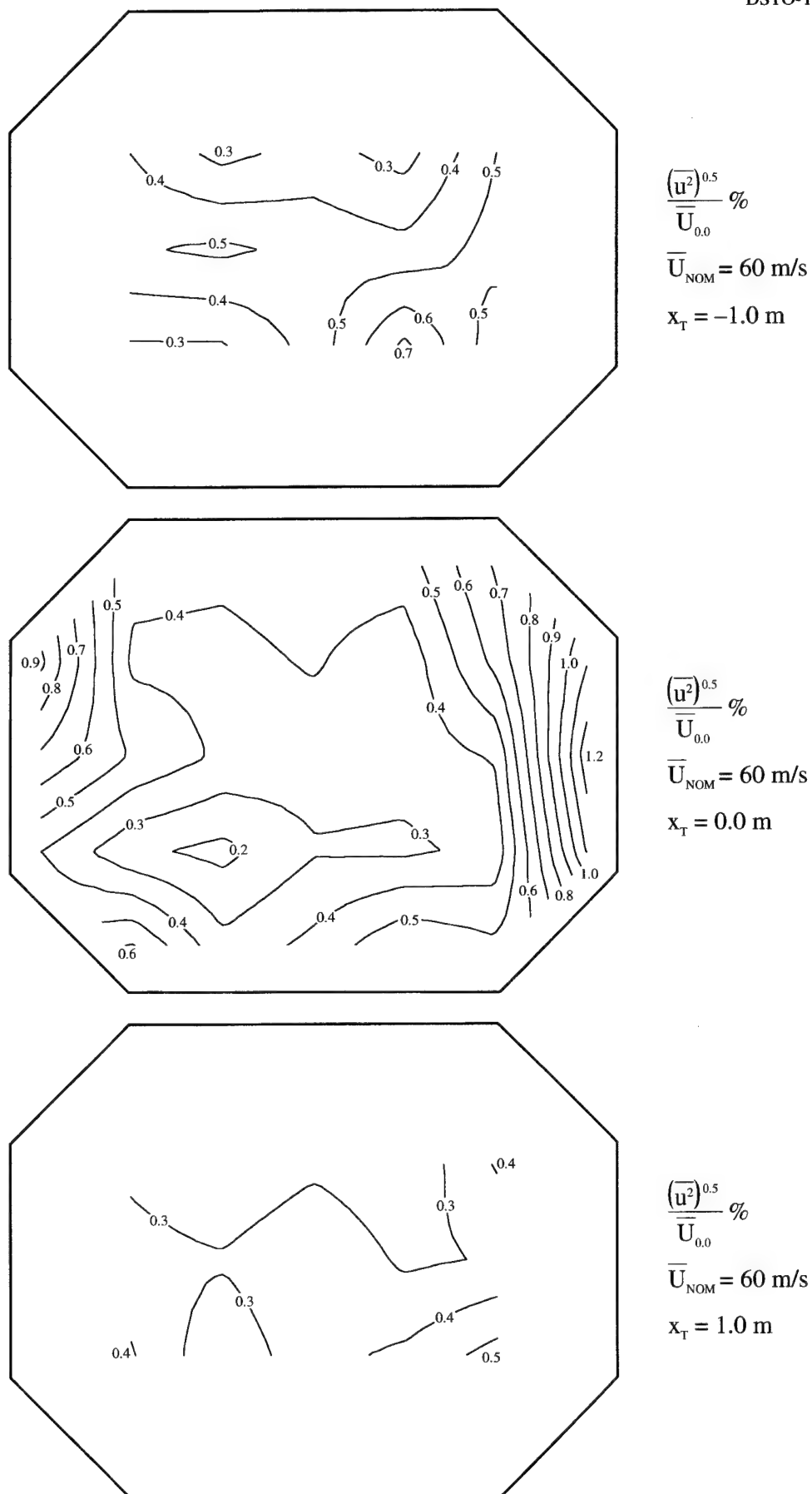
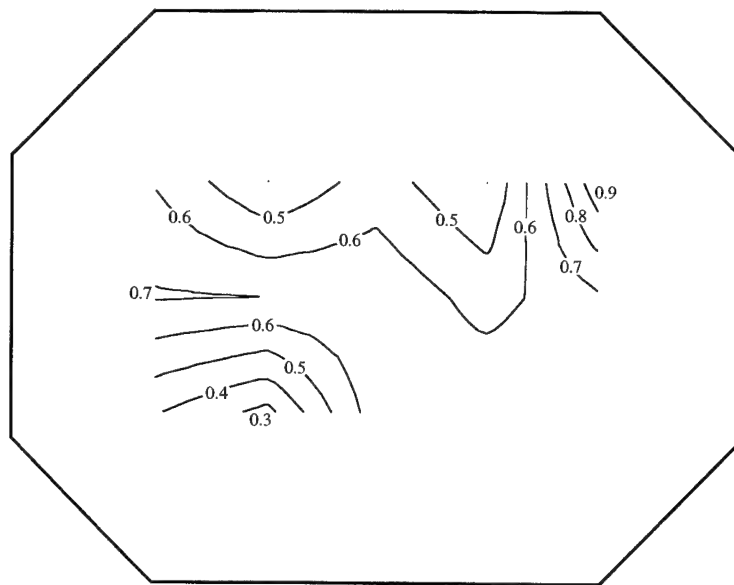


Figure 32. Contours of u-component intensity for  $\overline{U}_{\text{NOM}} = 60 \text{ m/s}$  for  $x_T = -1.0, 0.0$  and  $1.0 \text{ m}$ .

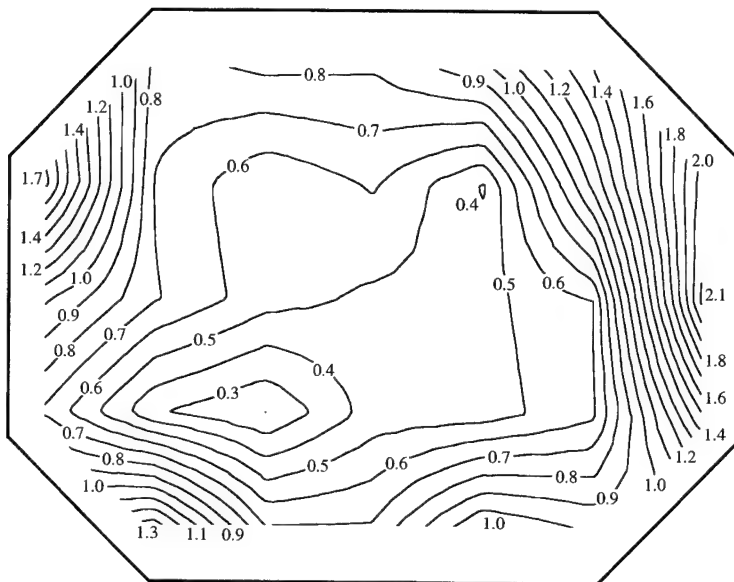
The flow is out of the page.



$$\frac{(\overline{v^2})^{0.5}}{\overline{U}_{0.0}} \%$$

$$\overline{U}_{\text{NOM}} = 60 \text{ m/s}$$

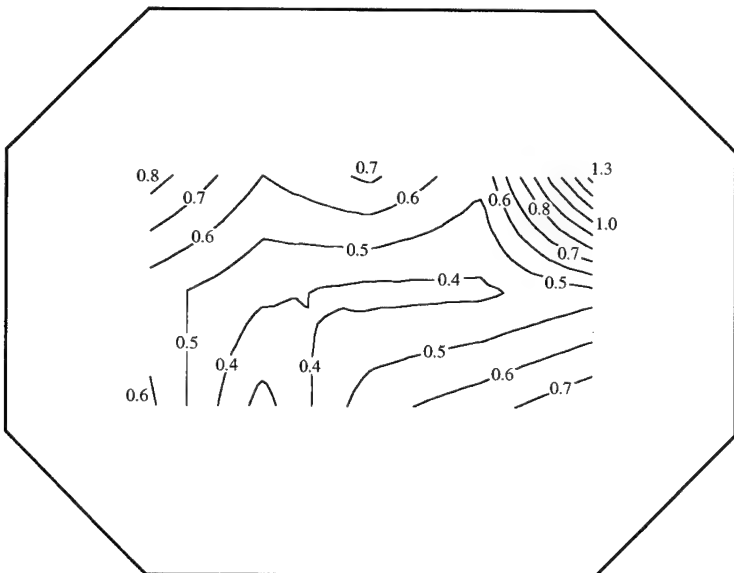
$$x_T = -1.0 \text{ m}$$



$$\frac{(\overline{v^2})^{0.5}}{\overline{U}_{0.0}} \%$$

$$\overline{U}_{\text{NOM}} = 60 \text{ m/s}$$

$$x_T = 0.0 \text{ m}$$



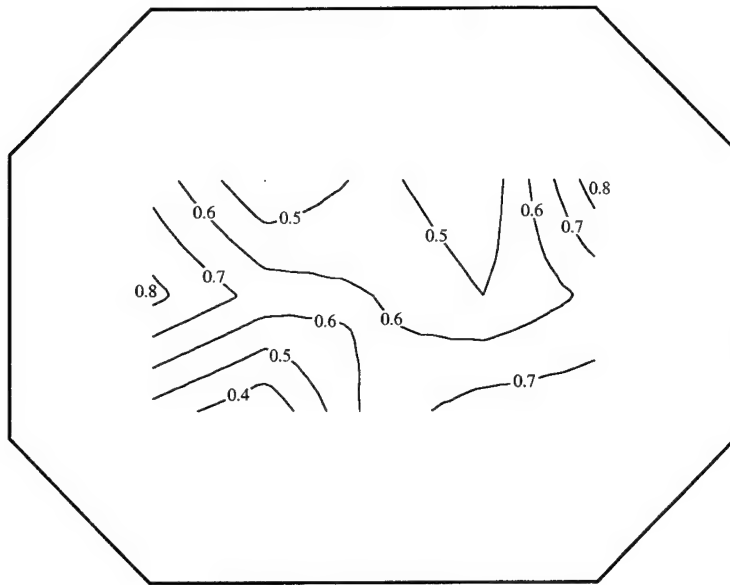
$$\frac{(\overline{v^2})^{0.5}}{\overline{U}_{0.0}} \%$$

$$\overline{U}_{\text{NOM}} = 60 \text{ m/s}$$

$$x_T = 1.0 \text{ m}$$

Figure 33. Contours of v-component intensity for  $\overline{U}_{\text{NOM}} = 60 \text{ m/s}$  for  $x_T = -1.0, 0.0$  and  $1.0 \text{ m}$ .

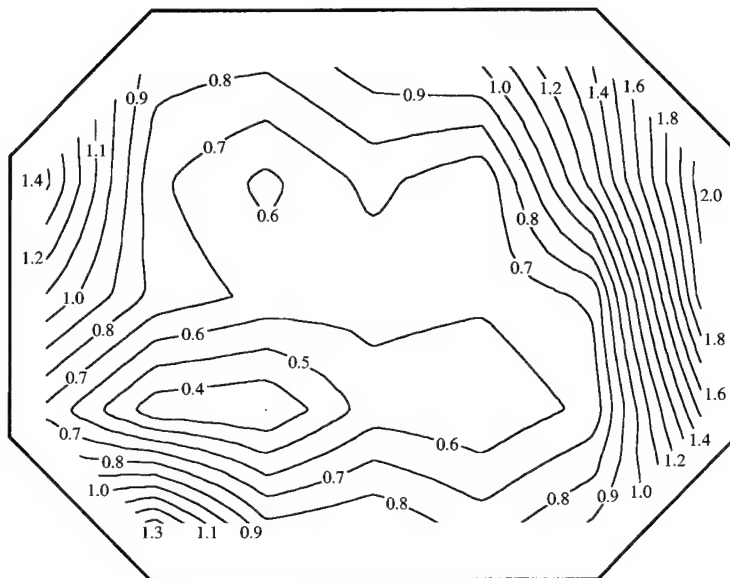
The flow is out of the page.



$$\frac{(\overline{w^2})^{0.5}}{\overline{U}_{0.0}} \%$$

$$\overline{U}_{\text{NOM}} = 60 \text{ m/s}$$

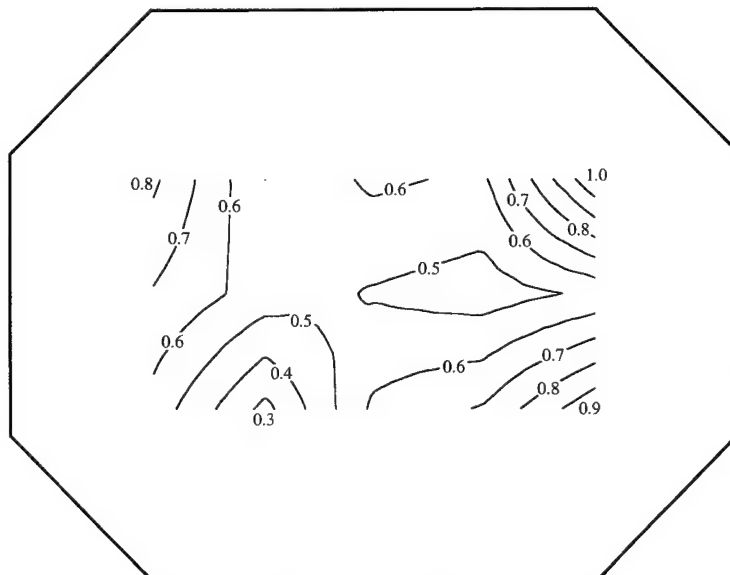
$$x_T = -1.0 \text{ m}$$



$$\frac{(\overline{w^2})^{0.5}}{\overline{U}_{0.0}} \%$$

$$\overline{U}_{\text{NOM}} = 60 \text{ m/s}$$

$$x_T = 0.0 \text{ m}$$



$$\frac{(\overline{w^2})^{0.5}}{\overline{U}_{0.0}} \%$$

$$\overline{U}_{\text{NOM}} = 60 \text{ m/s}$$

$$x_T = 1.0 \text{ m}$$

Figure 34. Contours of w-component intensity for  $\overline{U}_{\text{NOM}} = 60 \text{ m/s}$  for  $x_T = -1.0, 0.0$  and  $1.0 \text{ m}$ .

The flow is out of the page.

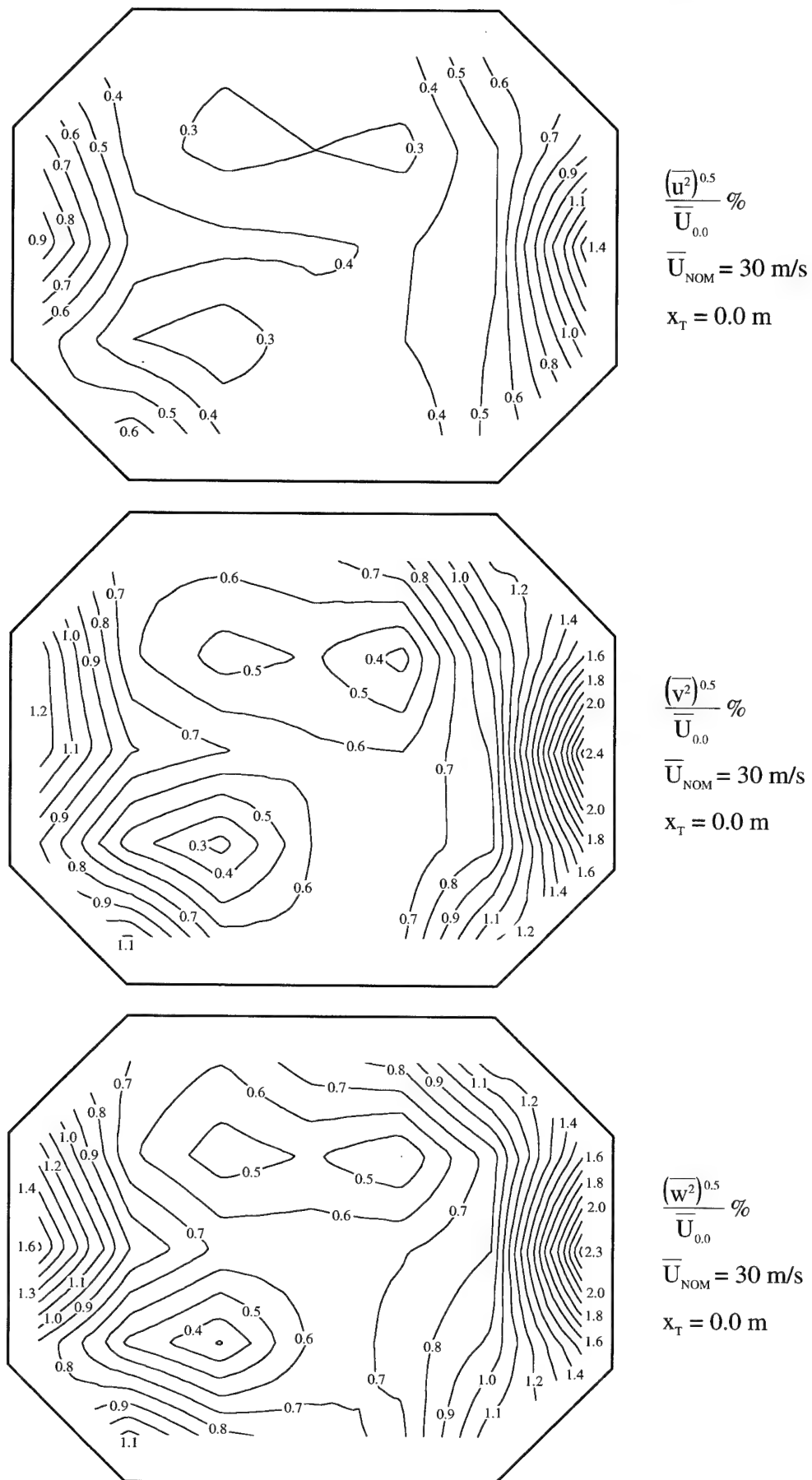
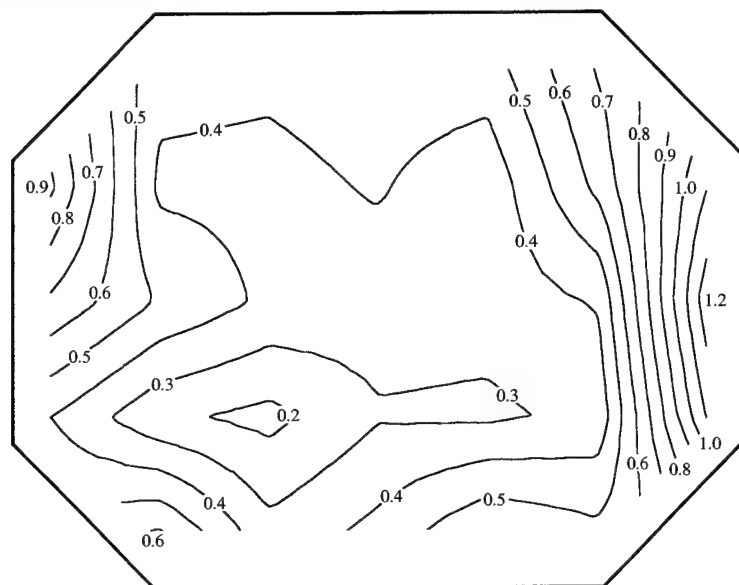


Figure 35. Contours of u- v- and w-component intensities for  $\overline{U}_{\text{NOM}} = 30 \text{ m/s}$  for  $x_T = 0.0 \text{ m}$ .

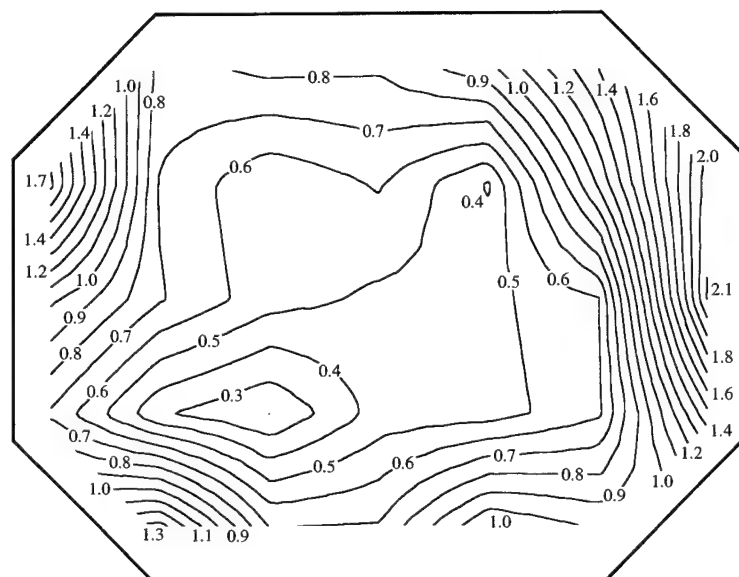
The flow is out of the page.



$$\frac{(\overline{u^2})^{0.5}}{\overline{U}_{0.0}} \%$$

$$\overline{U}_{\text{NOM}} = 60 \text{ m/s}$$

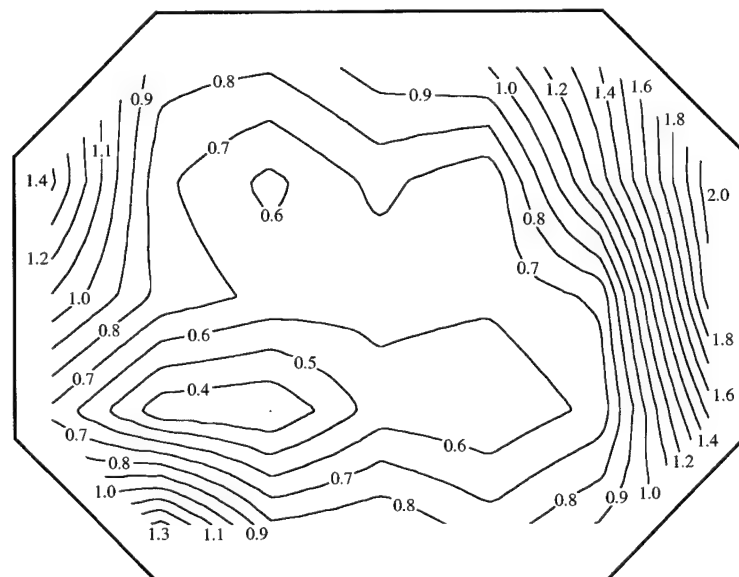
$$x_T = 0.0 \text{ m}$$



$$\frac{(\overline{v^2})^{0.5}}{\overline{U}_{0.0}} \%$$

$$\overline{U}_{\text{NOM}} = 60 \text{ m/s}$$

$$x_T = 0.0 \text{ m}$$



$$\frac{(\overline{w^2})^{0.5}}{\overline{U}_{0.0}} \%$$

$$\overline{U}_{\text{NOM}} = 60 \text{ m/s}$$

$$x_T = 0.0 \text{ m}$$

Figure 36. Contours of u- v- and w-component intensities for  $\overline{U}_{\text{NOM}} = 60 \text{ m/s}$  for  $x_T = 0.0 \text{ m}$ .

The flow is out of the page.

#### 4.5 Errors in Measured Turbulence Intensities

There are errors in the measured turbulence intensities,  $(\overline{u^2})^{0.5}/\overline{U}_{0.0}$ ,  $(\overline{v^2})^{0.5}/\overline{U}_{0.0}$  and  $(\overline{w^2})^{0.5}/\overline{U}_{0.0}$ , due to instrumentation errors and also due to the fact that the calibration of the hot wires may have drifted slightly between the start and finish of a set of measurements. Instantaneous velocities measured by the hot wires were accurate to within about  $\pm 1.5\%$  due to the drifting of the calibration of the hot wires. It was found that, for  $\overline{U}_{\text{NOM}} = 30$  m/s, errors in  $(\overline{u^2})^{0.5}/\overline{U}_{0.0}$ ,  $(\overline{v^2})^{0.5}/\overline{U}_{0.0}$  and  $(\overline{w^2})^{0.5}/\overline{U}_{0.0}$  were about  $\pm 0.011$ ,  $\pm 0.018$  and  $\pm 0.018$  percentage points respectively. Corresponding errors for  $\overline{U}_{\text{NOM}} = 60$  m/s were about  $\pm 0.007$ ,  $\pm 0.013$  and  $\pm 0.013$  percentage points respectively.

#### 4.6 Turbulence Signals and Mean-Velocity Variations

It should be possible to determine if there are any significant periodic mean-velocity variations in the flow by analysing the sampled hot-wire anemometer output voltages corresponding to the instantaneous velocities. Variations in velocity of this type cannot be determined from the mean-flow measurements given earlier in Section 2. A good tunnel should not have any significant periodic mean-velocity variations in the test section.

As mentioned in Section 4.3, the turbulence intensities at each grid point were determined by sampling the hot-wire-anemometer voltages 30 000 times at a sampling frequency of 200 Hz, which corresponds to a sampling time of 150 s. During this time, air particles travel around the tunnel circuit about 40 times when  $\overline{U}_{\text{NOM}} = 30$  m/s and about 80 times when  $\overline{U}_{\text{NOM}} = 60$  m/s.

Examples of the anemometer output voltages corresponding to the u-, v-, and w-components of the turbulence for three grid points are shown plotted against time, for the full 150 s sampling time, in Figures 37 and 38 for  $\overline{U}_{\text{NOM}} = 30$  and 60 m/s respectively. The first 15 s of the traces are also plotted using a magnified time scale. For convenience, each voltage trace has been plotted with the appropriate mean voltage removed. The values of the mean voltages were not important and they were arbitrarily set on the anemometer system when measuring turbulence intensities. The three grid points chosen are on the 'inner side' (starboard side) of the tunnel in the  $x_T = 0.0$  m transverse plane, and the  $y_T/W$  and  $z_T/H$  coordinates of the points are  $-0.3, -0.4$ ;  $-0.45, 0.0$ ; and  $-0.3, 0.4$  (see Figure 2). These points were selected because if there are any irregularities in the flow, for example, due to separation near the contraction inlet, then they are more likely to be evident on the 'inner side' of the tunnel. The traces in Figures 37 and 38 remain 'straight' and parallel with the time axis, indicating that there are no significant periodic irregularities in the mean velocities for these three points. Similar results were obtained for other grid points.

## 5. Spectral Measurements

### 5.1 Test Schedule

Spectra for the u-, v- and w-components of the turbulence were measured in the test section at the 5 grid points shown in Figure 28 (a) for  $x_T = 0.0$  m as well as at the 5 grid points shown in Figure 28 (b) for  $x_T = -1.0$  and 1.0 m. Spectra were measured for  $\bar{U}_{\text{NOM}} = 30$  and 60 m/s.

### 5.2 Procedure Used to Measure Spectra

Spectra were measured using the hot-wire anemometer system and the modified cross-tunnel rake that were used for the intensity measurements. The spectral and intensity experimental programs were combined so that data for a given spectrum was generally measured immediately before or immediately after data for the corresponding intensity.

When measuring spectra, each hot-wire voltage was sampled 65536 times (i.e.  $2^{16}$  times –see below) at a sampling frequency of 20 kHz and the low-pass filters were set at 10 kHz. This filter setting was used since velocity fluctuations above 10 kHz in the free-stream have negligible energy (Reference 13) and the setting corresponds to the maximum frequency that can be resolved when sampling at 20 kHz, due to aliasing. Spectra were obtained by processing hot-wire voltages, rather than by processing velocities determined from voltages, as for the intensities, and it was not necessary to know hot-wire sensitivities. Power spectral densities,  $S_u$ ,  $S_v$  and  $S_w$ , were computed from the voltages using a Fast-Fourier-Transform (FFT) algorithm (where the number of data points required is a power of 2). For each spectrum, power spectral densities were computed using the 65536 ( $= 2^{16}$ ) consecutively sampled voltages, without any averaging. For a sampling frequency of 20 kHz, the frequencies at which power spectral densities were computed ranged from 0.3052 Hz to 10 kHz in increments of 0.3052 Hz, i.e.  $20000/65536$  Hz, corresponding to  $32768 (= 2^{15})$  values of frequency.

Whenever a fluctuating velocity waveform is represented by a finite number of points, then the mean velocities near the start and finish of the finite sample can be significantly different. When computing spectra from these waveforms, this behaviour can be interpreted as a low-frequency phenomenon, coupled with high frequency effects due to the step change between the beginning and end of the sample, and it can cause an increase in spectral densities at low frequencies. One way of correcting for this behaviour is to apply a Blackman window to the data (Reference 14). A Blackman window adjusts velocities (or any given measurand) so that their values at the start and finish of the chosen range are gradually diminished, becoming zero at the extremes. The application of a Blackman window also smoothes the spectra. This is done by first smoothing with a Hanning window and then further smoothing with weights of 0.16, 0.68 and 0.16 (Reference 14). All spectra given in this report have been smoothed with a Blackman window and the spectra have been normalized by dividing by the variance.



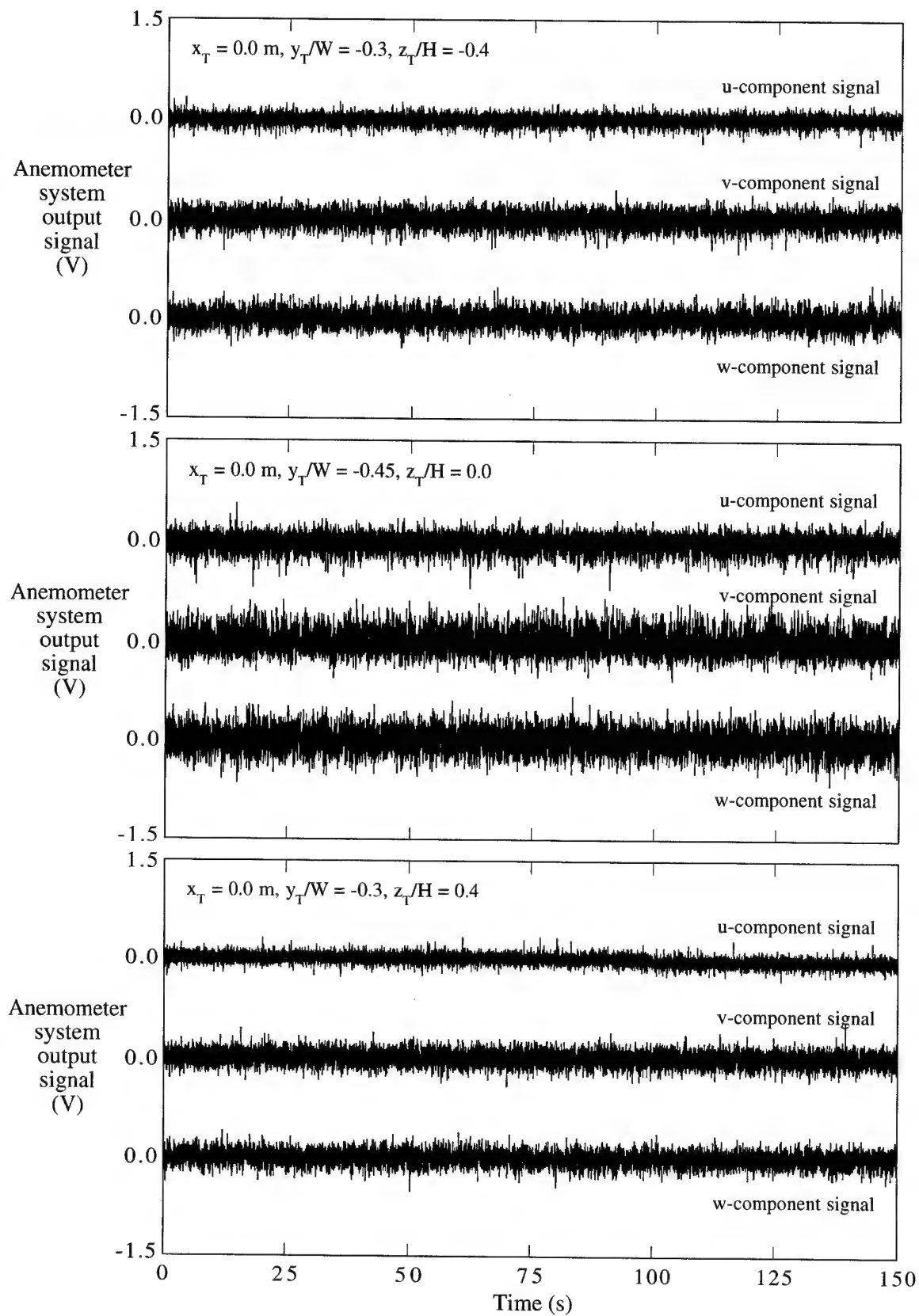


Figure 37a. Sampled turbulence voltage signals at selected grid points for  $\bar{U}_{\text{NOM}} = 30.0 \text{ m/s}$ .

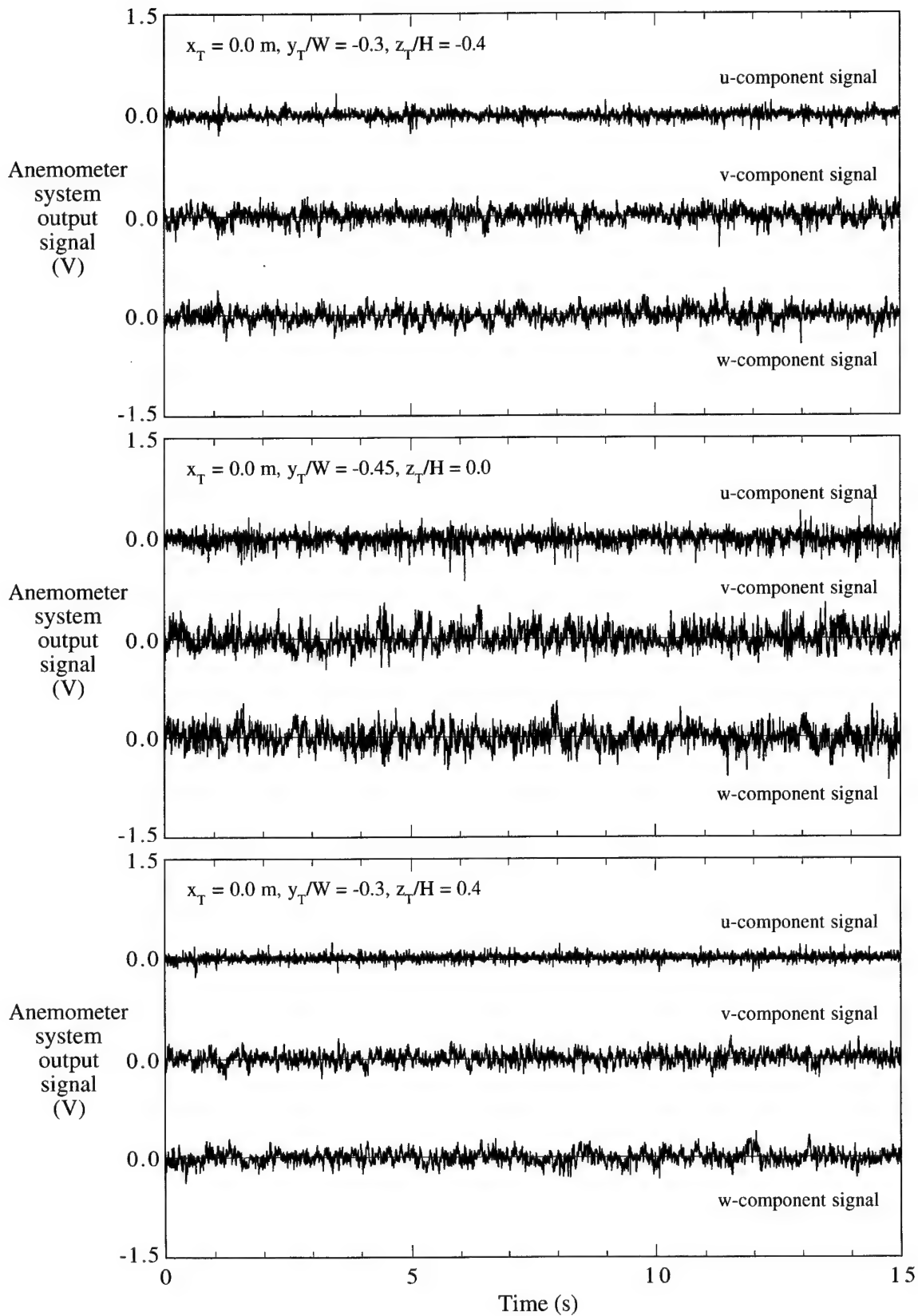


Figure 37b. Sampled turbulence voltage signals at selected grid points for  $\bar{U}_{\text{NOM}} = 30.0 \text{ m/s}$ .

Magnified time scale.

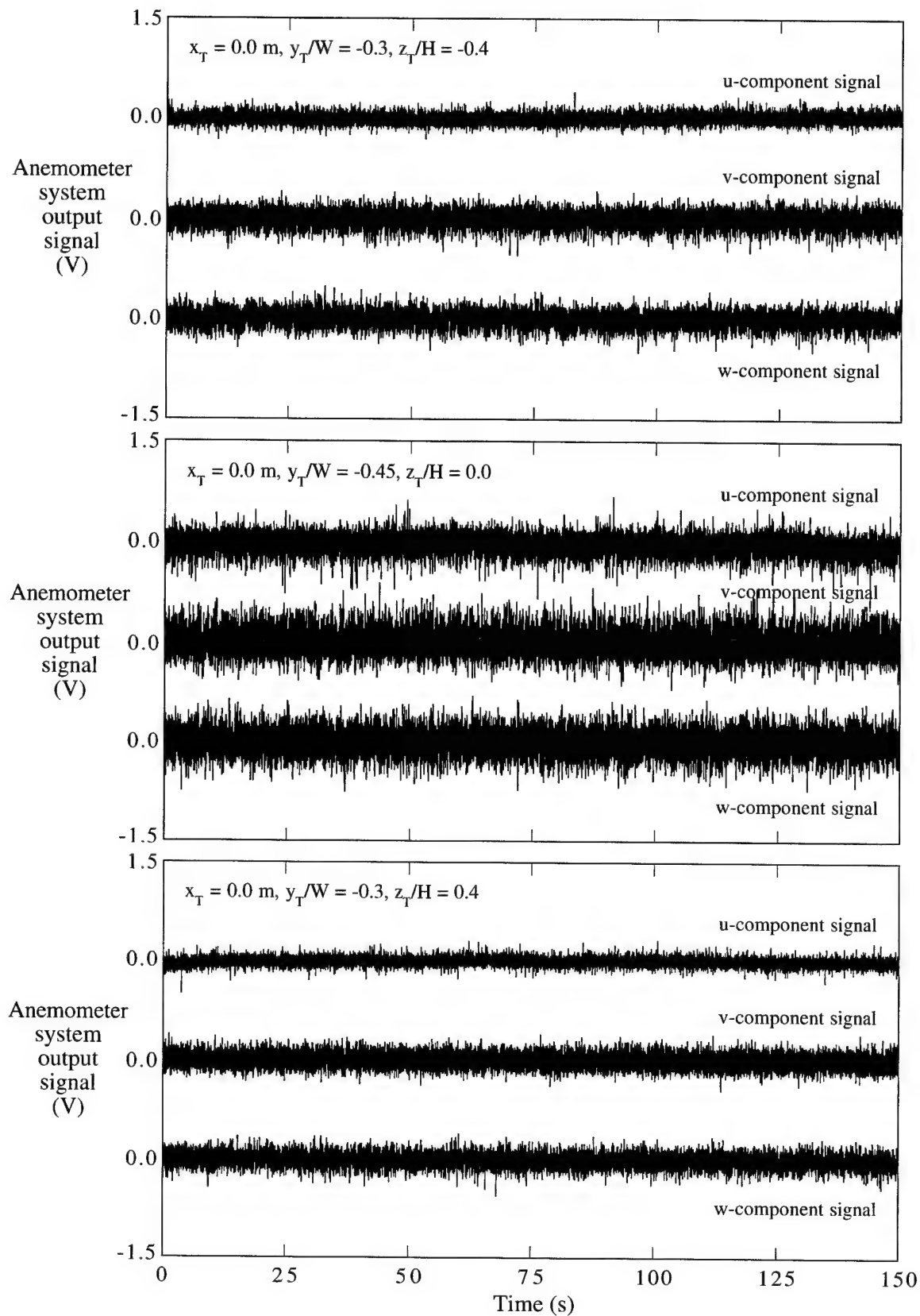


Figure 38a. Sampled turbulence voltage signals at selected grid points for  $\bar{U}_{\text{NOM}} = 60.0 \text{ m/s}$ .

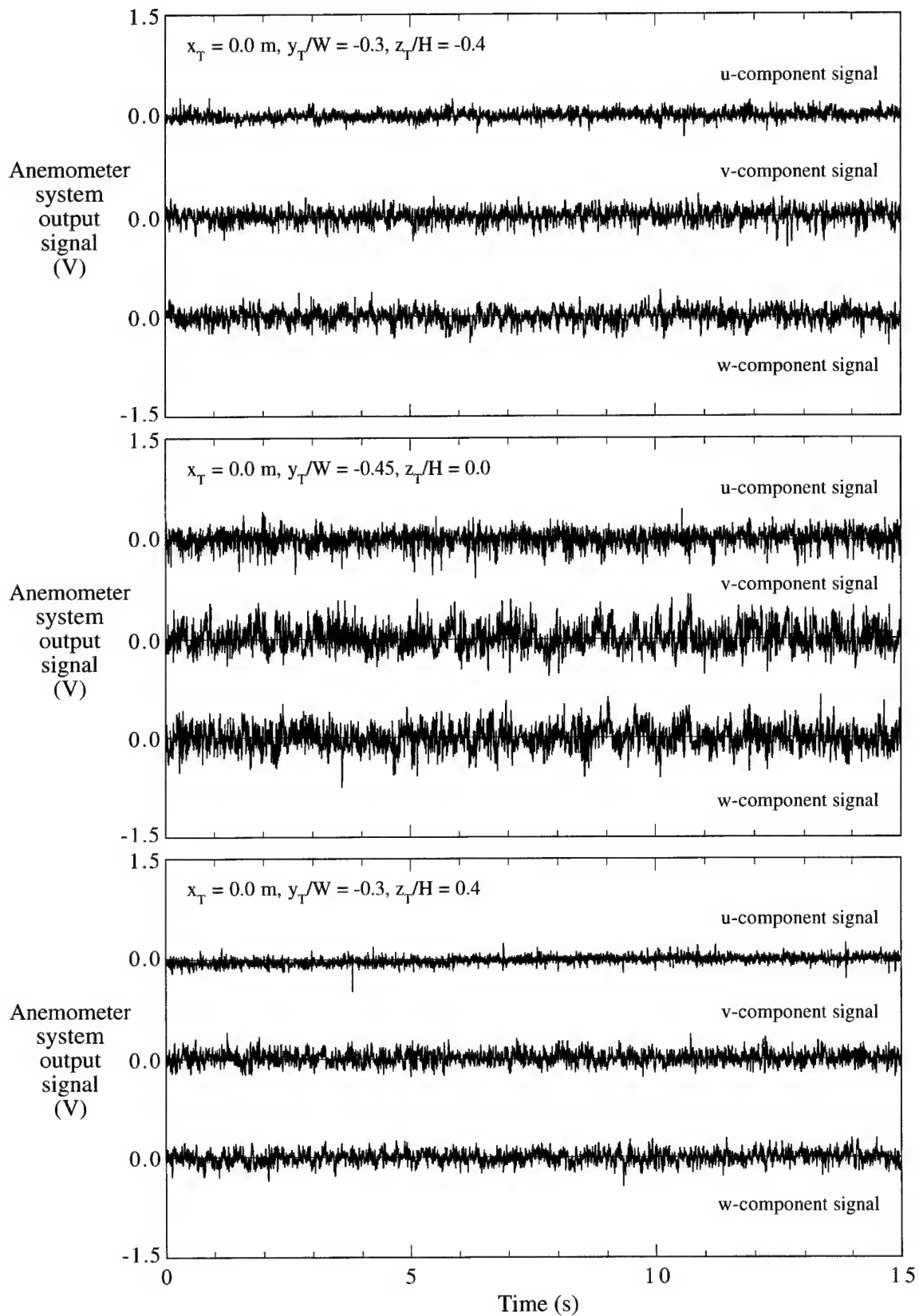


Figure 38b. Sampled turbulence voltage signals at selected grid points for  $\bar{U}_{\text{NOM}} = 60.0 \text{ m/s}$ .

Magnified time scale

### 5.3 Analysis of Spectra

Spectra corresponding to conventional wind-tunnel-generated turbulence should be relatively smooth, but if the turbulent flow contains eddies of dominant frequencies, such as vortices shed by the fan, then these will produce harmonics or spikes on the spectra. If there is any significant “noise” on a fluctuating turbulent signal, caused by say electrical interference or probe vibration, then this will also cause spikes. As a result of this noise, calculated turbulence intensities will be higher than actual intensities existing in the tunnel. By noting the frequency at which the spikes occur, it is often possible to identify the source of the irregularities, e.g. the frequency of the spikes may correspond with the frequency of the electrical mains supply or the frequency of rotation of the fan. A knowledge of the causes of the irregularities is valuable when trying to eradicate them.

Power spectral densities,  $S_u$ , plotted against frequency,  $f$ , are shown in Figure 39 at the grid points shown in Figure 28 for  $\bar{U}_{\text{NOM}} = 30$  m/s for  $x_T = -1.0, 0.0$ , and  $1.0$  m. Corresponding spectra for  $S_v$  and  $S_w$  are shown in Figures 40 and 41 respectively. The spectra in each of Figures 39 to 41 are plotted together without being identified individually. Figures 42 to 44 show spectra for  $\bar{U}_{\text{NOM}} = 60$  m/s. The spectra cover the central region of the flow in the test section. The spectra show that there are no major irregularities in the turbulence signals over the frequency range 0.3 Hz to 10 kHz. For all of the u-component spectra, there are small but consistent spikes at about 150 Hz, and the reason for these is uncertain. The spikes are not associated with the frequency of the fan rotation since they are present at about 150 Hz for both  $\bar{U}_{\text{NOM}} = 30$  and 60 m/s and they do not appear to be caused by electrical interference from mains supply (50 Hz). The irregularity, whatever its cause, does not significantly affect measured values of turbulence intensities, for reasons given below. There are also some isolated spikes at the high-frequency ends of some spectra.

Spectra can be plotted in premultiplied form, whereby power spectral densities are multiplied by the associated frequencies and the product of these two terms is plotted on a linear scale against frequency. With this type of plot, the energy contribution to the intensities over any given frequency range is represented as an area under the spectrum.

Premultiplied spectra for the u-component of the turbulence for  $\bar{U}_{\text{NOM}} = 30$  and 60 m/s and for  $x_T = 0.0$ ,  $y_T = 0.0$ , and  $z_T = 0.0$  m are shown in Figure 45. It is apparent that fluctuations having frequencies below about 20 Hz for  $\bar{U}_{\text{NOM}} = 30$  m/s and below about 40 Hz for  $\bar{U}_{\text{NOM}} = 60$  m/s make relatively little contribution to the measured u-component intensities despite the fact that such fluctuations correspond to the highest power spectral densities, as evident from Figures 39 and 42 respectively. The irregularity at around 150 Hz, referred to above, is shown quite clearly, but owing to the very small frequency band the contribution of this “spike” to the turbulent energy in the flow is very small. Most of the turbulent energy contributing to the intensities is associated with frequencies between 20 Hz and 2 kHz for  $\bar{U}_{\text{NOM}} = 30$  m/s and between 40 Hz and 4 kHz for  $\bar{U}_{\text{NOM}} = 60$  m/s.

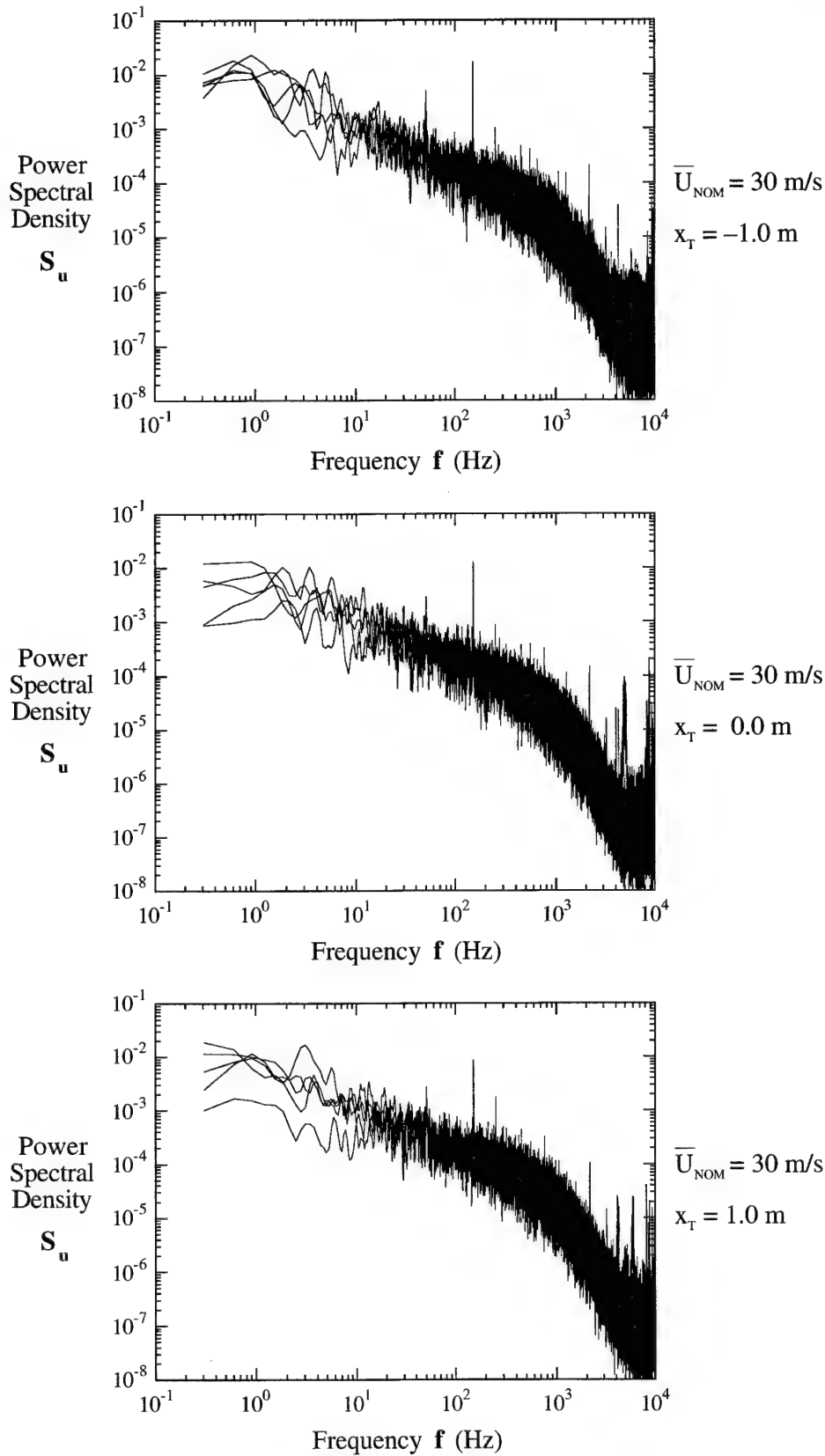


Figure 39. Spectra for the  $u$  component of the turbulence for  $\overline{U}_{\text{NOM}} = 30 \text{ m/s}$  for  $x_T = -1.0$ ,  $0.0$  and  $1.0 \text{ m}$  for  $y_T$  and  $z_T$  locations denoted by filled circles in Figure 28.

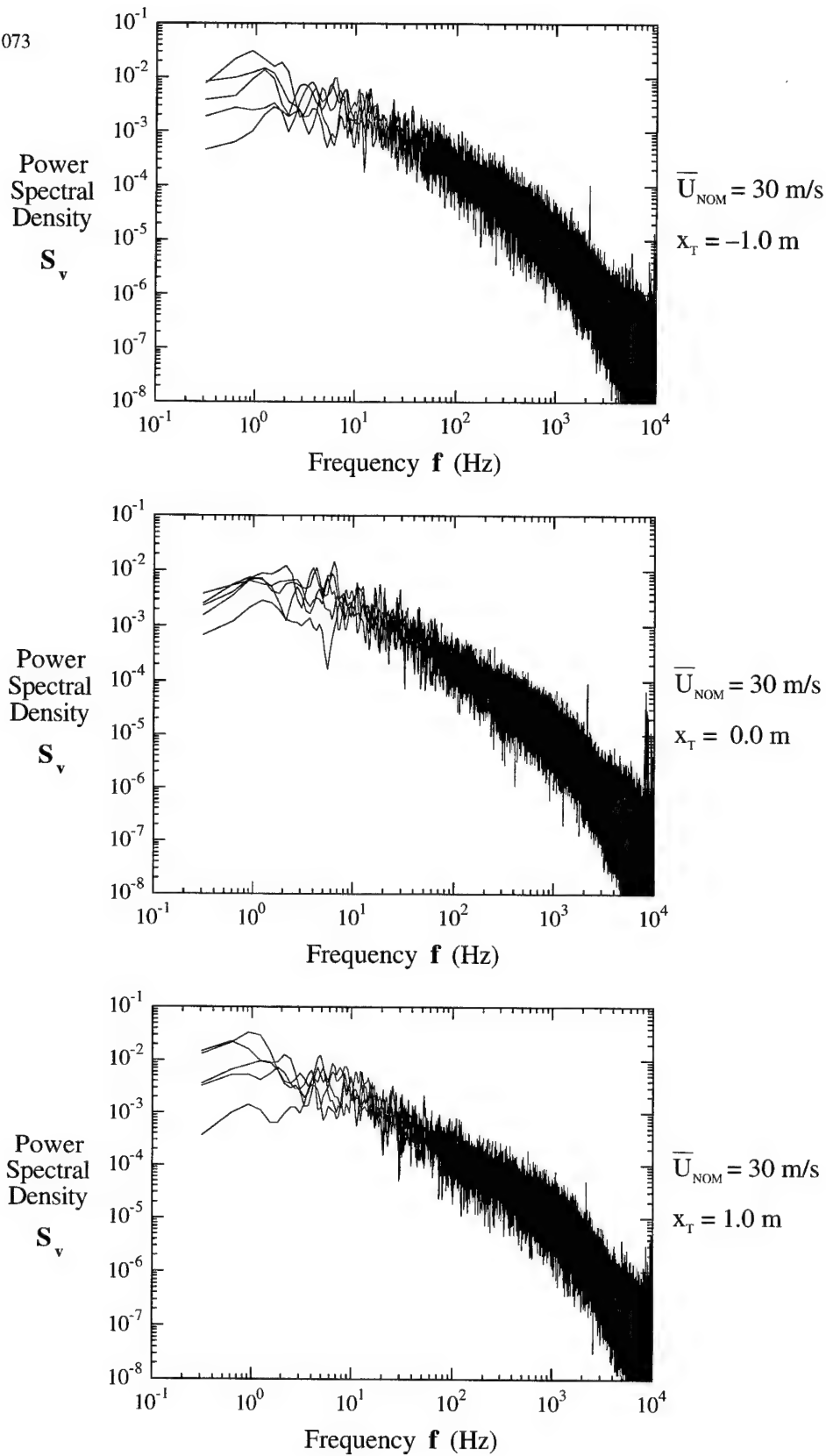


Figure 40. Spectra for the  $v$  component of the turbulence for  $\bar{U}_{\text{NOM}} = 30 \text{ m/s}$  for  $x_T = -1.0$ ,  $0.0$  and  $1.0 \text{ m}$  for  $y_T$  and  $z_T$  locations denoted by filled circles in Figure 28.

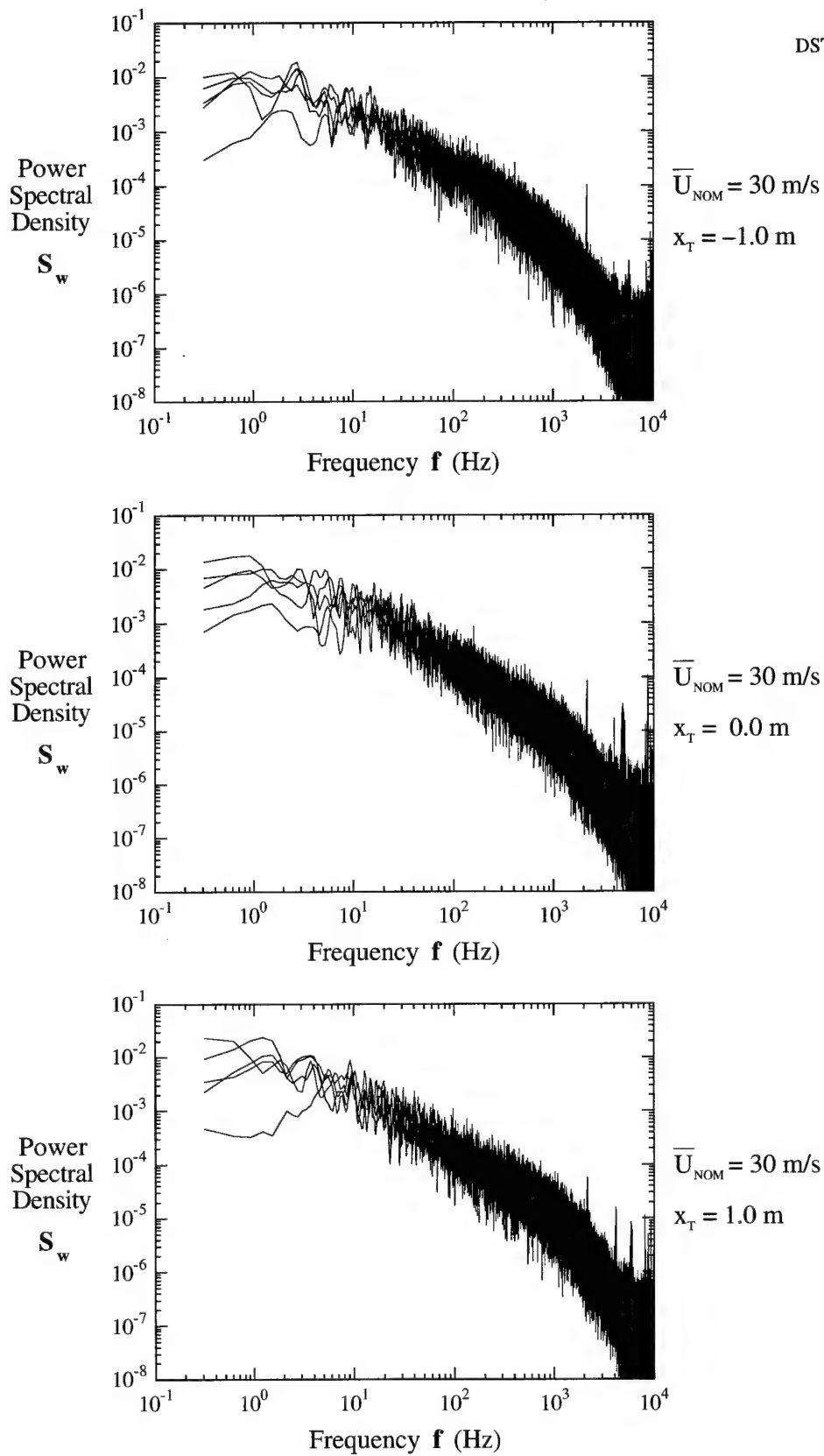


Figure 41. Spectra for the  $w$  component of the turbulence for  $\bar{U}_{\text{NOM}} = 30 \text{ m/s}$  for  $x_T = -1.0$ ,  $0.0$  and  $1.0 \text{ m}$  for  $y_T$  and  $z_T$  locations denoted by filled circles in Figure 28.



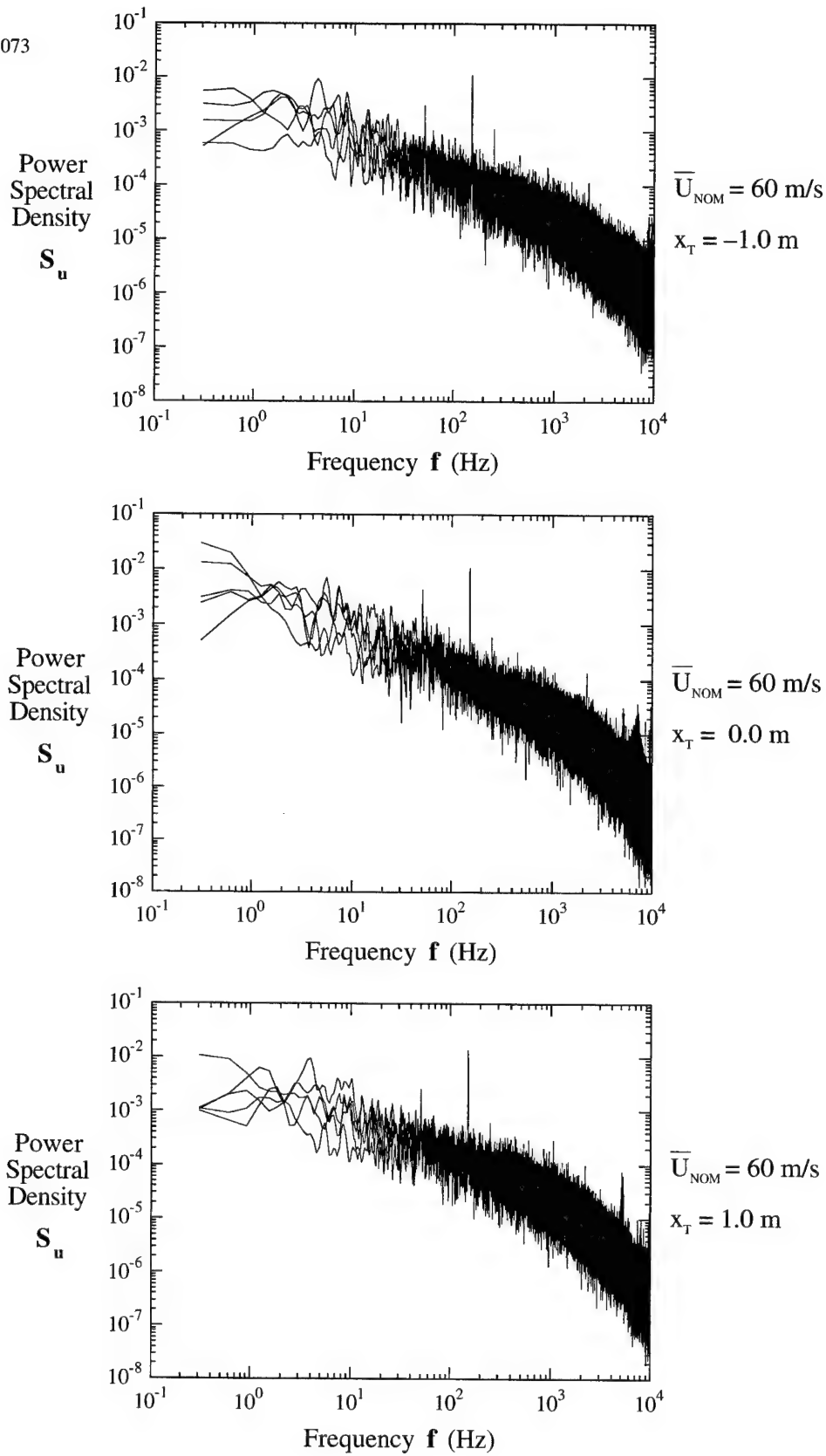


Figure 42. Spectra for the  $u$  component of the turbulence for  $\overline{U}_{\text{NOM}} = 60$  m/s for  $x_T = -1.0$ ,  $0.0$  and  $1.0$  m for  $y_T$  and  $z_T$  locations denoted by filled circles in Figure 28.

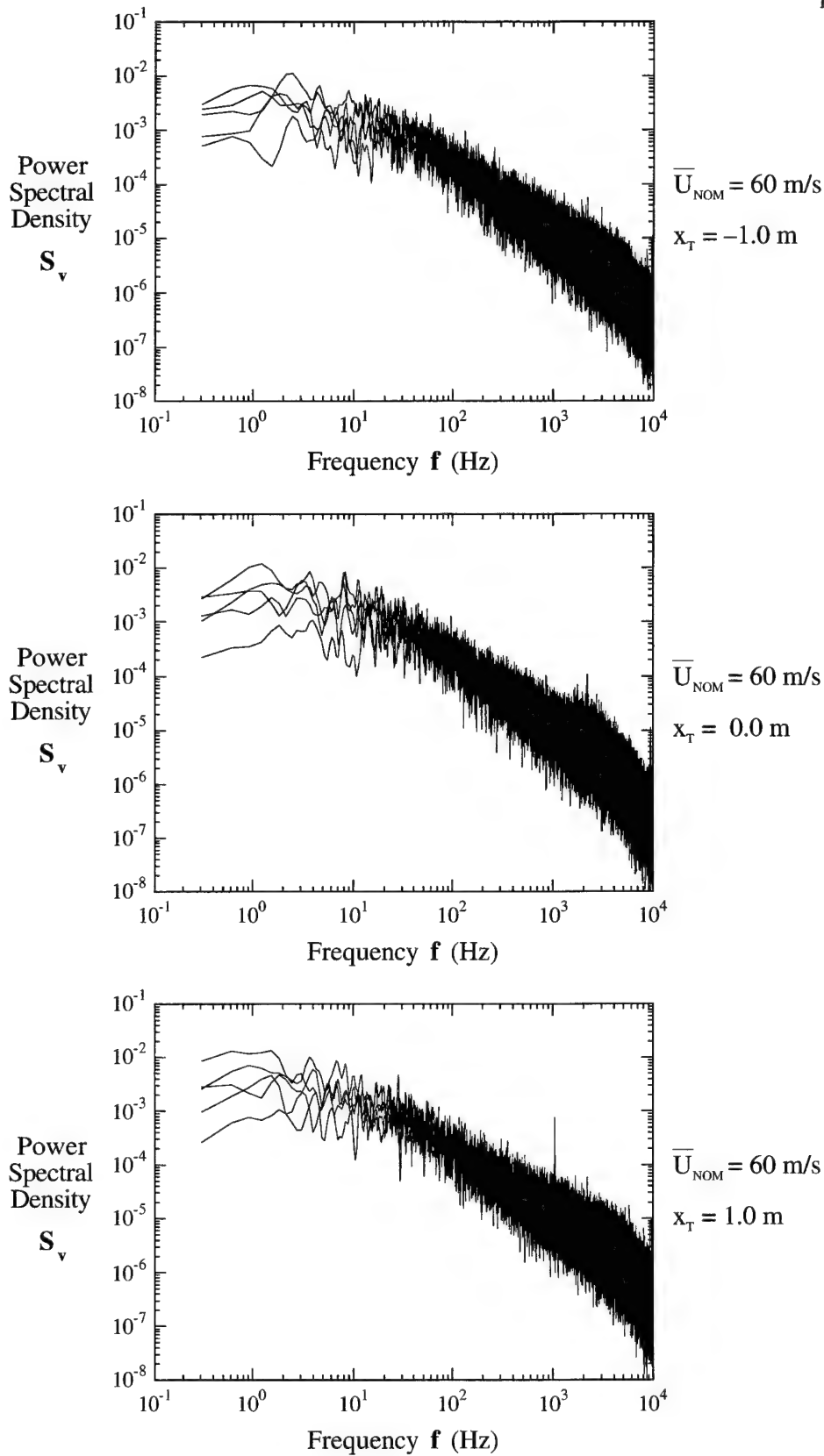


Figure 43. Spectra for the  $v$  component of the turbulence for  $\overline{U}_{\text{NOM}} = 60 \text{ m/s}$  for  $x_T = -1.0$ ,  $0.0$  and  $1.0 \text{ m}$  for  $y_T$  and  $z_T$  locations denoted by filled circles in Figure 28.

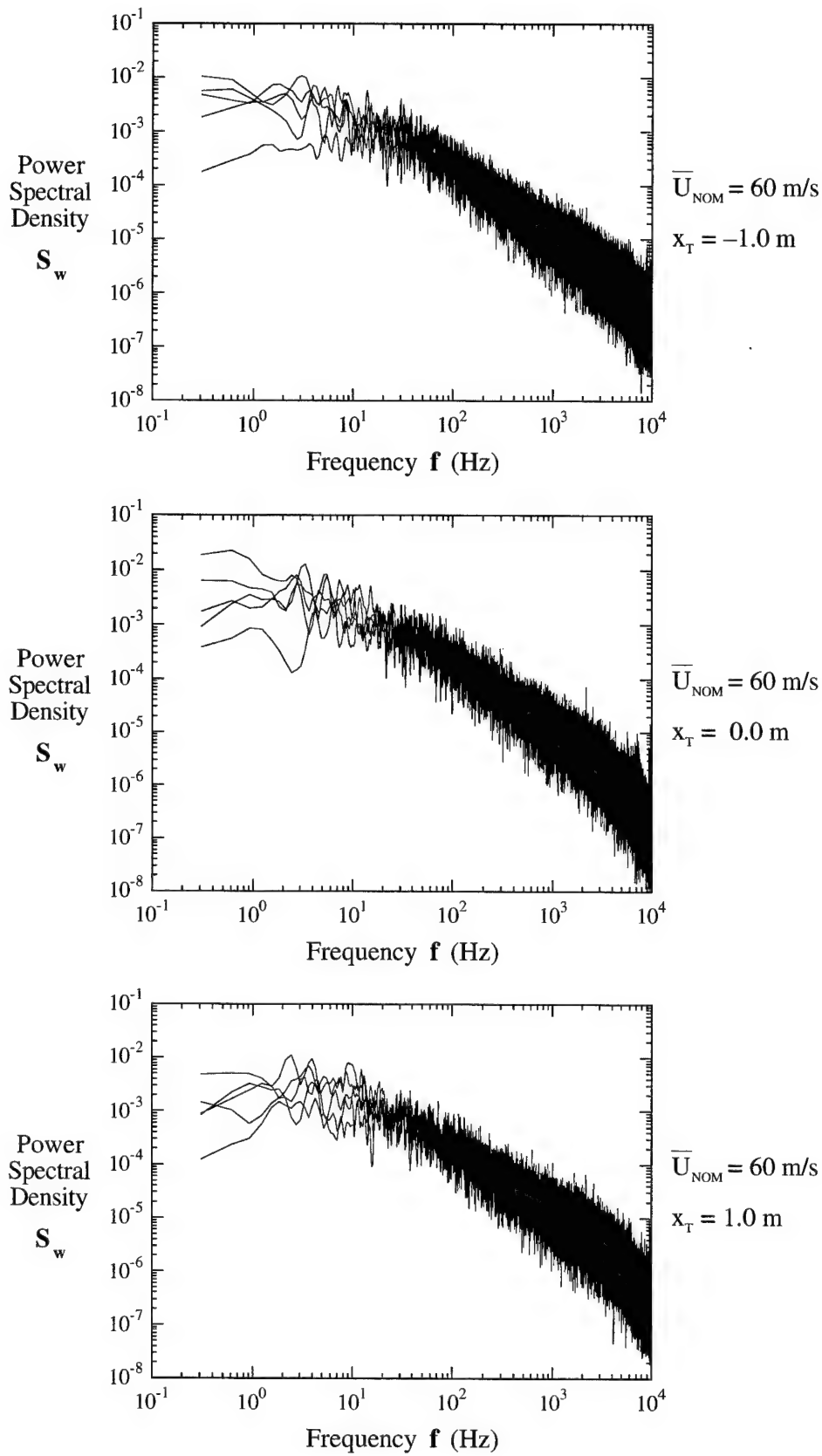


Figure 44. Spectra for the  $w$  component of the turbulence for  $\overline{U}_{\text{NOM}} = 60 \text{ m/s}$  for  $x_T = -1.0$ ,  $0.0$  and  $1.0 \text{ m}$  for  $y_T$  and  $z_T$  locations denoted by filled circles in Figure 28.

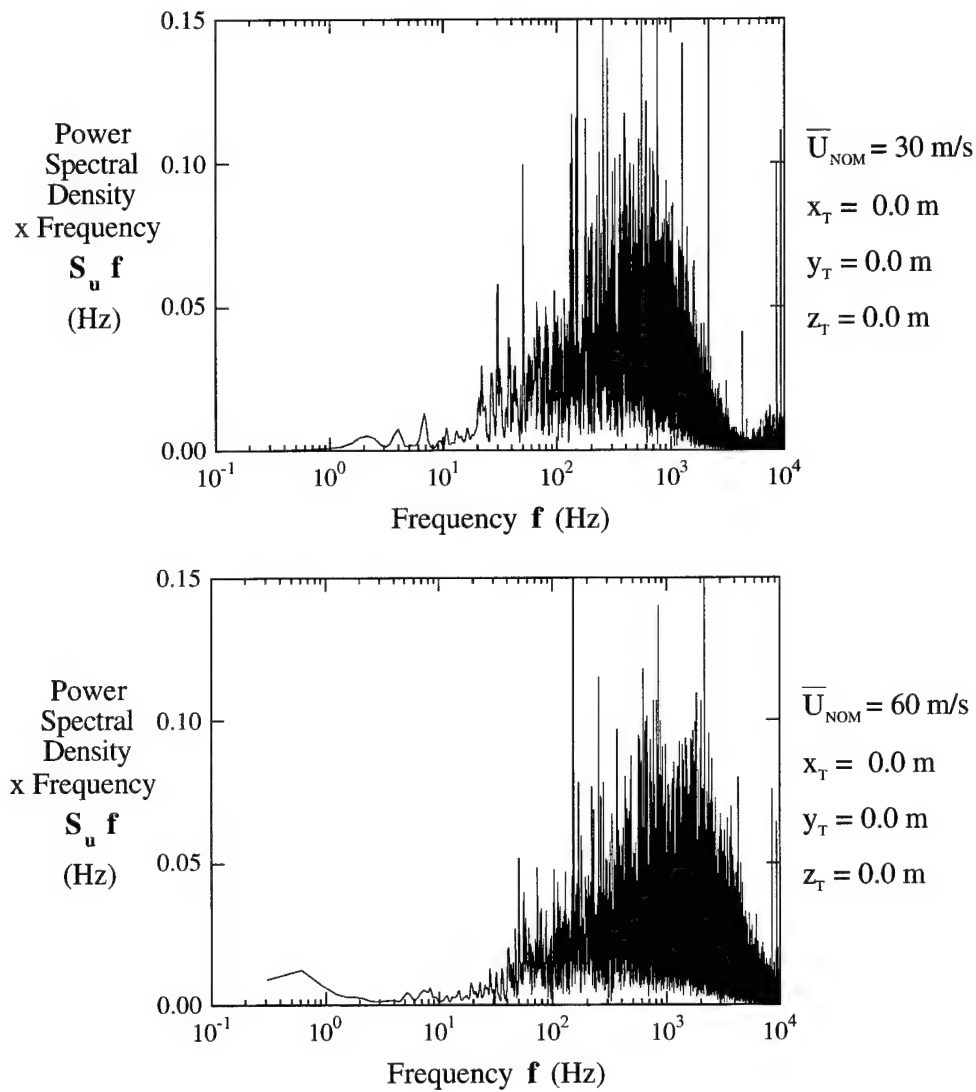


Figure 45. Premultiplied spectra for the u component of the turbulence for  $\bar{U}_{\text{NOM}} = 30$  and  $60$  m/s for  $x_T = 0.0$ ,  $y_T = 0.0$  and  $z_T = 0.0$  m.

## 6. Assessment of Flow Quality in the LSWT

It has been shown that, like nearly all fully-enclosed flows, the flow in the test section of the LSWT with the contraction that was in place from 1941 until 1996 had some non-uniformity in terms of mean-velocity deviations, flow angularity and turbulence intensities. In the following, flow non-uniformities for the tunnel are quoted for approximately the central 50% of the cross-sectional area of the test section.

### 6.1 Mean Velocities

For  $\bar{U}_{\text{NOM}} = 30$  m/s, the maximum variation in longitudinal mean velocities between  $x_T = -1.0$  m and  $x_T = +1.0$  m was from  $-0.6\%$  to  $+2.0\%$  from their values at the centre of the test section ( $x_T = 0.0$ ,  $y_T = 0.0$  and  $z_T = 0.0$  m) (Figure 9). Corresponding variations for other nominal free-stream velocities were from  $-0.8\%$  to  $+1.6\%$  for  $\bar{U}_{\text{NOM}} = 45$  m/s (Figure 10), from  $-0.6\%$  to  $+1.8\%$  for  $\bar{U}_{\text{NOM}} = 60$  m/s (Figure 11) and from  $-0.2\%$  to  $+2.0\%$  for  $\bar{U}_{\text{NOM}} = 75$  m/s (Figure 12).

In Reference 9 it is indicated that acceptable longitudinal mean-velocity deviations across the test section are often quoted in the range  $\pm 0.20\%$  to  $\pm 0.30\%$  variation from the average value of the mean velocity across the test section. Reference 15 indicates that acceptable mean-velocity variations of a high performance tunnel are  $\pm 0.2\%$ . In the 8 m  $\times$  6 m test section of the German-Dutch large low-speed wind tunnel, the total-pressure deviations (expressed as pressure coefficients) are less than 0.3% at 90 m/s, and the static-pressure deviations (expressed as pressure coefficients) are well within 0.6% at 100 m/s (Reference 13). The deviations in the total and static pressures are relative to the total and static pressures respectively at the centre of the tunnel test section. (Unfortunately, it has not been possible to determine variations in mean velocity from the published data since the given deviations in total pressure apply to a region and not specific locations, so that total pressures and static pressures cannot be matched). The five metre low-speed wind tunnel at the Defence Evaluation and Research Agency (formerly Royal Aircraft Establishment) has mean-velocity variations of about  $\pm 0.12\%$  although the design aim was only  $\pm 0.05\%$  (Reference 16).

As shown in Section 4.6, the hot-wire measurements were used to indicate if there were any periodic mean-velocity variations in the flow. These results showed that there were no significant periodic or intermittent irregularities in the mean velocity in the test section.

### 6.2 Flow Angles

For  $\bar{U}_{\text{NOM}} = 30$  m/s, the variation in the horizontal flow angles between  $x_T = -1.0$  m and  $x_T = +1.0$  m was from  $-0.8^\circ$  to  $+0.6^\circ$  (Figure 23). Similarly, the variation in vertical flow angles was from  $-0.8^\circ$  to  $+0.4^\circ$  (Figure 24). For  $\bar{U}_{\text{NOM}} = 60$  m/s, horizontal flow angles varied from  $-0.4^\circ$  to  $+0.8^\circ$  (Figure 25) and vertical flow angles varied from  $-1.0^\circ$  to  $+0.4^\circ$  (Figure 26).

According to Reference 9, it would be desirable to have horizontal and vertical flow angle variations of less than  $\pm 0.10^\circ$ , but if this cannot be achieved, then the variations should be held to  $\pm 0.20^\circ$ . In Reference 15 it is indicated that acceptable flow angle variations for a high performance tunnel are  $\pm 0.1^\circ$ . For the German-Dutch wind tunnel (Reference 13), the horizontal and vertical flow angles vary by less than  $0.2^\circ$  across the central region of the  $8 \text{ m} \times 6 \text{ m}$  test section for a reference free-stream velocity of 90 m/s.

### 6.3 Turbulence Intensities and Spectra

For  $\bar{U}_{\text{NOM}} = 30$  and 60 m/s, and for  $x_T = -1.0, 0.0$  and 1.0 m, values of  $(\bar{u}^2)^{0.5}/\bar{U}_{0.0}$  were generally below about 0.4%, whereas corresponding values of  $(\bar{v}^2)^{0.5}/\bar{U}_{0.0}$  and  $(\bar{w}^2)^{0.5}/\bar{U}_{0.0}$  were generally below about 0.7% (Figures 29 to 34). Spectra for the u- v- and w-components of the turbulence were relatively smooth over the frequency range 0.3 Hz to 10 kHz, with no significant spikes associated with irregularities in the flow (Figures 39 to 45).

Reference 17 indicates that a root-mean-square u-component fluctuation of 0.1% of the mean velocity is often quoted as low enough for most experiments and that the best low-turbulence research tunnels have a turbulence intensity of the order of 0.02% at low speeds. In Reference 9 it is indicated that tunnels used for developmental testing can have longitudinal turbulence intensities as high as 0.5%, and that tunnels used for research in boundary layers and boundary layer transition should have lateral values of intensity below about 0.05%. In the German-Dutch wind tunnel (Reference 13), the longitudinal intensities are quoted to be less than about 0.08% and the lateral intensities less than about 0.15% in the central region of the  $8 \text{ m} \times 6 \text{ m}$  test section for a reference free-stream velocity of 75 m/s. However, for a velocity of about 40 m/s, the longitudinal intensities are 0.02%, which is comparable with the best low turbulence wind tunnels.

### 6.4 Adequacy of Flow Quality in the LSWT

The foregoing suggests that although the quality of the flow in the test section of the LSWT with the contraction that was in place until 1996 is acceptable, it could be improved. However, there is no point spending a large amount of money on the tunnel to improve the flow if it is adequate for the investigations likely to be undertaken. The question of whether the quality of the flow is adequate depends upon the types of tests.

For flow-visualization investigations, where qualitative rather than quantitative answers are often required, the quality of the flow is not all that important and the tunnel should be adequate for this type of work.

For experiments in which boundary-layer transition phenomena are important, the free-stream turbulence intensities should be low since high intensities can cause early

transition and this can lead to difficulties in interpreting experimental results. Longitudinal turbulence intensities of 0.1% to 0.5%, similar to those in the LSWT, are classed as moderate turbulence levels (Reference 18), so that some lack of similarity may result if the tunnel was used for these types of experiments.

Accurate force, moment and surface pressure measurements taken on a model of say an aircraft are needed in a number of areas, including to determine loading programs for fatigue tests on full-scale aircraft, to provide data for the development of flight-dynamic models of aircraft behaviour, and to provide data for the verification of computational-fluid-dynamic (CFD) codes. If there are imperfections in the flow, then this may lead to data being produced that does not represent the full-scale aircraft to the accuracy required. For example, if the angle of the flow incident on one of the wings of a model of a typical fighter aircraft is  $1^\circ$  different from that on the other wing, due to the flow asymmetry in the test section, then potentially this could produce an error of the order of 5 to 10% in the maximum measured rolling moment coefficient for the aircraft. However, to provide accurate data from wind-tunnel tests to enable the performance of a full-scale aircraft to be predicted, irregularities in the flow is only one of the factors that needs to be considered. Reynolds number effects and the size of the model with respect to the size of the test section are also important.

## **7. Possible Causes of Flow Non Uniformities and Possible Methods for Improving the Flow**

Flow irregularities in the test sections of wind tunnels may arise from a number of different flow mechanisms and generally it is not possible to identify with certainty the causes of these irregularities simply by analysing measured calibration data. Variations in mean velocity can be caused by flow separations in the tunnel return circuit, flow separations in the contraction, poor corner vane design or incorrectly set vanes (resulting in the vanes over or under turning the flow), and poor design of the fan or straightening vanes (resulting in a rotation of the whole flow downstream of the fan). Turbulence can be generated in the boundary layers on the tunnel walls and from the wakes of the fan blades, the turning vanes and the honeycombs. Angularity in the flow can persist into the test section if the honeycomb has cells of an inappropriate size and aspect ratio (see below). Flow non-uniformities in a test section are also more pronounced close to the outlet of a contraction than they are further downstream in the test section (Reference 19). Despite the uncertainties involved in making a precise assessment of the causes of flow irregularities in a tunnel, it is possible to identify some of the likely causes for the LSWT at AMRL.

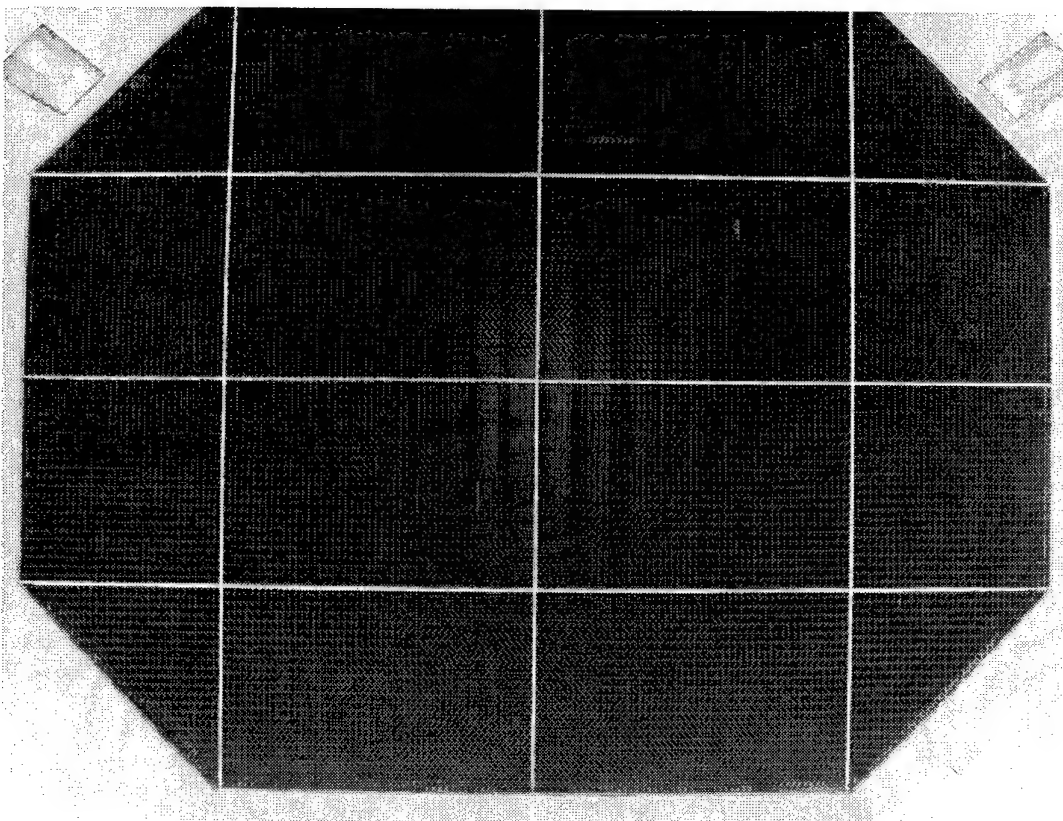
If the contraction in a wind tunnel is not well designed then adverse pressure gradients can occur near the inlet and this can lead to either continuous flow separation, or

intermittent flow separation, depending on the magnitude of the adverse pressure gradient (Reference 9). Wool-tuft studies in the contraction in the early 1960s, after the replacement of the air-flow propulsion system (see Section 1), indicated that there was no separation and that the contraction met requirements (unpublished). However, from later studies reported in Reference 20, it is stated that "Recent wool tuft flow visualization studies have confirmed that the boundary layers at the entry to the contraction suffer from intermittent separation". Discussions with wind-tunnel staff indicated that some intermittent separation was occurring in the contraction of the tunnel at about 0.3 to 0.7 Hz, while others believed there was no separation. The conflicting nature of this previous evidence relating to adverse pressure gradients and intermittent separation has not been resolved. However, there is no evidence of intermittent flow separation in the current measurements –see fluctuating turbulence signals shown in Section 4.6 and spectra shown in Section 5.3.

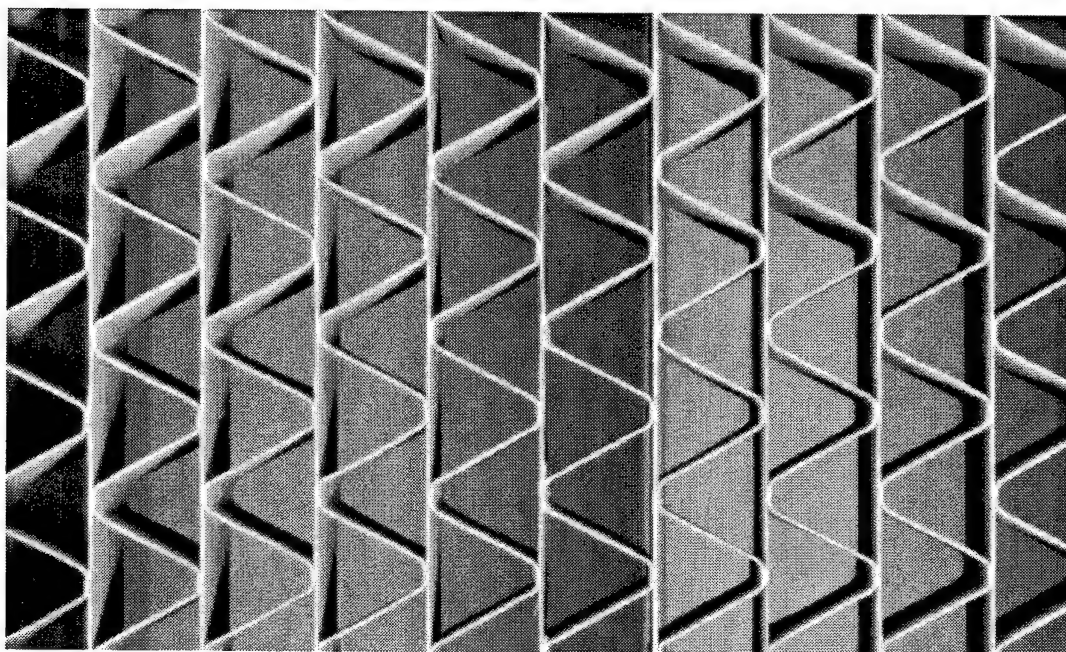
Honeycombs and screens are known to improve the quality of the flow in the test section of a tunnel, both in terms of improved longitudinal and lateral mean-velocity distributions and reduced longitudinal and lateral turbulence intensities. Screens reduce longitudinal components of mean velocities and intensities more than lateral components, as for a contraction, whereas honeycombs reduce lateral components of mean velocities and intensities more than longitudinal components. The honeycomb in the LSWT has triangular cells whose frontal dimensions are 48, 41 and 41 mm and the depth of the cells is 127 mm (approximate dimensions), as shown in Figure 46. The diameter of a circle having the same cross-sectional area of a cell is about 32 mm so that the ratio of the depth of the cells to the effective diameter of the cells is about 4:1, which is somewhat lower than the recommended aspect ratio of about 6:1 to 8:1 (References 9 and 17). The sizes of the cells in the honeycomb are also larger than normal. In Reference 21, a study was made of honeycombs in wind tunnels and it was found that the honeycombs had cell sizes ranging from 1.6 mm (1/16 inch) to 9.5 mm (3/8 inch) and aspect ratios varying between 6:1 and 8:1. The existing honeycomb is not continuous as it has been installed in the tunnel in 16 sections. Between each section there is a solid edge about 15 mm thick and these edges may have a detrimental effect on the flow in the test section (Reference 9). If it is decided that a new honeycomb is needed (see below), then it should have cells with a smaller frontal area and a larger aspect ratio, and follow the design dimension guidelines given above. It would be preferable to use a honeycomb having hexagonal cells since the pressure loss coefficient for this type of honeycomb is less than for honeycombs having square or circular cross sections (Reference 9). It would probably be necessary to use some type of supporting structure to prevent the honeycomb deflecting, and it should be less intrusive than the rigid supporting structure presently in the tunnel. Currently the tunnel does not have any screens. If it is decided to install them, an open-to-total area ratio of the order of 57% is preferable (Reference 22).

Most likely there is not a single cause of the flow non uniformities and it may be necessary to change more than one component of the tunnel to obtain a large improvement in the flow. It is preferable that the modifications to the tunnel be carried out in





(a) view of complete honeycomb, showing details of the 16 sections



(b) close-up view of the honeycomb, showing frontal details of the triangular cells

Figure 46. Honeycomb used in the low-speed wind tunnel.

stages. As mentioned in Section 1, a new test section and contraction were installed in 1996 to meet the requirement of testing longer models. Within the constraints imposed by the space available in the existing settling chamber and the new contraction design, the length of the test section was increased from 4.12 m to 6.56 m. The effect on the flow of the new test section and contraction will be reported at a later date. If it is decided to install a new honeycomb, then preformed aluminium hexagonal honeycomb or stacks of thin-walled hexagonal metal tubing could be inserted into the existing honeycomb supporting structure to replace the current triangular cells and minimize cost. This type of modification would reduce the maximum obtainable velocity in the test section. Installing screens would reduce turbulence intensities, but this would also increase losses and reduce the maximum velocity in the test section. Additional cleaning would also be necessary as both the screens and modified honeycomb could accumulate dust which could change the quality of the flow with time (Reference 9). A new contraction, or a new contraction and a new honeycomb, may provide sufficient improvement in the flow without screens.

## 8. Concluding Remarks

A detailed calibration of the flow in the test section of the low-speed wind tunnel with the contraction that was in place until 1996 is given in this report. An extensive range of longitudinal mean-flow velocities, flow angles, turbulence intensities and turbulence spectra were measured at up to 155 grid points across the flow for longitudinal positions,  $x_T$ , of  $-1.0$ ,  $0.0$  and  $1.0$  m from the centre of the turntables in the test section and for nominal free-stream velocities,  $\bar{U}_{\text{NOM}}$ , ranging from 30 to 75 m/s.

Longitudinal mean-flow velocities were measured using pressure probes fitted to a rake which spanned the test section. Flow angles were measured using a six-hole probe mounted on a specially-designed traversing mechanism. Turbulence intensities and power spectral densities were obtained using constant-temperature hot-wire anemometers.

Considering approximately the central 50% of the cross-sectional area of the test section, the following flow non-uniformities were observed.

### • Mean-Flow Velocities

For  $\bar{U}_{\text{NOM}} = 30$  m/s, the maximum variation in longitudinal mean velocities between  $x_T = -1.0$  m and  $x_T = +1.0$  m was from  $-0.6\%$  to  $+2.0\%$  from their values at the centre of the test section ( $x_T = 0.0$ ,  $y_T = 0.0$  and  $z_T = 0.0$  m). Corresponding variations for other nominal free-stream velocities were from  $-0.8\%$  to  $+1.6\%$  for  $\bar{U}_{\text{NOM}} = 45$  m/s, from  $-0.6\%$  to  $+1.8\%$  for  $\bar{U}_{\text{NOM}} = 60$  m/s and from  $-0.2\%$  to  $+2.0\%$  for  $\bar{U}_{\text{NOM}} = 75$  m/s. No significant periodic variations in mean velocities were found.

- Flow angles

For  $\bar{U}_{\text{NOM}} = 30$  m/s, for  $x_T = -1.0$  to  $+1.0$  m, the variation in the horizontal flow angles was from  $-0.8^\circ$  to  $+0.6^\circ$  and the variation in the vertical flow angles was from  $-0.8^\circ$  to  $+0.4^\circ$ . For  $\bar{U}_{\text{NOM}} = 60$  m/s, horizontal flow angles varied from  $-0.4^\circ$  to  $+0.8^\circ$  and vertical flow angles varied from  $-1.0^\circ$  to  $+0.4^\circ$ .

- Turbulence Intensities and Spectra

For  $\bar{U}_{\text{NOM}} = 30$  and  $60$  m/s, at  $x_T = -1.0, 0.0$  and  $+1.0$  m, the root-mean-square u-component turbulence intensities were generally below about 0.4%, whereas corresponding v- and w-component intensities were generally below about 0.7%. Spectra for the u- v- and w-components of the turbulence were relatively smooth over the frequency range 0.3 Hz to 10 kHz, with no significant spikes associated with irregularities in the flow.

From the present tests it is not possible to identify with certainty the causes of the variations in mean velocities, flow angles, turbulence intensities and spectra in the test section. If there was intermittent boundary-layer separation at the inlet to the contraction then its effects are not apparent. The honeycomb has larger cells with a lower aspect ratio (cell depth divided by effective cell diameter) than recommended for this type of tunnel, and this could contribute to the flow irregularities.

In 1996, the length of the test section was increased from 4.12 m to 6.56 m, to enable longer models to be tested. At the same time the contraction had to be replaced and a new design was selected (Reference 20). It was expected that the extended test section and the new contraction would lead to some improvement in the flow quality. If further improvement of flow quality is required, the honeycomb could be replaced with one having smaller cells that have a larger aspect ratio. It may also be necessary to install screens to reduce turbulence intensities, but this will result in a reduction in the maximum velocity in the test section and increased maintenance to clean the screens.

## 9. Acknowledgements

The author is grateful for help received from Dr N. Matheson, Head Flight Mechanics, and from Messrs P. T. Malone, I. D. Amott, A. A. Gonzalez, J. C. Clayton, D. M. Carnell and G. D. Ainger, who assisted with the experimental program.

## 10. References

1. 'The 9 ft.  $\times$  7 ft. wind tunnel at C.S.I.R. Division of Aeronautics, Fishermen's Bend, Melbourne'. *Report No. A.6.*, Council for Scientific and Industrial Research, Division of Aeronautics, August 1943.
2. Matheson, N., 'Static pressure and axial velocity distributions near the centre of the working section of the ARL 2.7 m  $\times$  2.1 m wind tunnel'. *Aerodynamics Technical Memorandum 346*, Aeronautical Research Laboratories, Melbourne, Australia, January 1983.
3. 'U. S. Standard Atmosphere 1962'. Prepared under sponsorship of National Aeronautics and Space Administration, United States Air Force and United States Weather Bureau, Washington, D. C. For sale by the Superintendent of Documents, U. S. Government Printing Office, Washington 25, D. C., USA.
4. Pressures Systems Incorporated. 'System 8400 Users Manual, Version 3.0'. Published by Pressures Systems Incorporated, Hampton, Virginia, USA, May 1990.
5. Glaister, M. K. & Hill, S. D. 'Electronic pressure scanning experience and software development'. *Proceedings of the Commonwealth Advisory Aeronautical Research Council (CAARC) specialists meeting on experimental aerodynamics and test techniques*, Defence Research Agency, Farnborough, UK, September 1992.
6. Chue, S. H. 'Pressure probes for fluid measurement'. *Progress in Aerospace Sciences*, Vol. 16, No. 2, 1975.
7. Melbourne, W. H. & Griss, R. J. 'Digital computation of velocity vectors using a suitably calibrated hemispherical head yawmeter'. *Aerodynamics Technical Memorandum 245*, Aeronautical Research Laboratories, Melbourne, Australia, November 1968.
8. Fairlie, B. D. 'Algorithms for the reduction of wind-tunnel data derived from strain gauge force balances'. *Aerodynamics Report 164*, Aeronautical Research Laboratories, Melbourne, Australia, May 1984.
9. Rae, W. H. Jr. & Pope, A. 'Low-speed wind tunnel testing'. John Wiley & Sons, New York, USA, 1984.
10. Erm, L. P. 'Modifications to a constant-temperature hot-wire anemometer system to measure higher-order turbulence terms using digital signal processing'. *DSTO Technical Report 0506*, Aeronautical and Maritime Research Laboratory, Melbourne, Australia, September 1997.

11. Watmuff, J. H. 'A hybrid hot-wire data acquisition system'. *Aerodynamics Report 172*, Aeronautical Research Laboratories, Melbourne, Australia, November 1986.
12. Eckert, D. 'First performance and calibration tests'. *Construction 1976-1980, Design Manufacturing Calibration of the German-Dutch Windtunnel (DNW)*, Edited by M. Seidel, Published by DNW, Printed in Germany by Hans Oeding, Braunschweig; 1982. Copies obtainable from DNW, Postbus 175, 8300 AD Emmeloord, The Netherlands.
13. 'Compilation of calibration data of the German-Dutch wind tunnel'. *Duits-Nederlandse Windtunnel, Deutsch-Niederlandischer Windkanal*, MP-82.01, March 1982.
14. Blackman, R. B. '*Linear data-smoothing and prediction in theory and practice*'. Addison-Wesley, Massachusetts, USA, 1965.
15. Bradshaw, P. & Pankhurst, R. C. 'The design of low speed wind tunnels'. *Progress in Aeronautical Sciences*, Vol. 5, Edited by D. Kucheman & L. H. G. Sterne, Pergamon Press, New York, USA, 1964.
16. Spence, A. et al. 'The RAE 5 metre pressurised low speed wind tunnel'.
17. Bradshaw, P. '*Experimental fluid mechanics*'. Pergamon Press Ltd, London, UK, 1964.
18. Coles, D. E. 'The turbulent boundary layer in a compressible fluid'. *Rand Report R-403-PR*, Appendix A: A manual of experimental boundary layer practice for low-speed flow, September 1962.
19. Chmielewski, G. E. 'Boundary-layer considerations in the design of aerodynamic contractions'. *J. Aircraft*, Vol. 11, No. 8, pp. 435-438, August 1974.
20. Watmuff, J. H. 'Design of a new contraction for the ARL low speed wind tunnel'. *Aerodynamics Report 171*, Aeronautical Research Laboratories, Melbourne, Australia, August 1986.
21. Scheiman, J. & Brooks, J. D. 'Comparison of experimental and theoretical turbulence reduction from screens, honeycomb, and honeycomb-screen combinations'. *JAS*, Vol. 18, pp. 638-643, 1981.
22. Bradshaw, P. 'The effect of wind tunnel screens on nominally two-dimensional boundary layers'. *J. Fluid Mech.*, Vol. 22, pp. 679-689, 1965.

## **DISTRIBUTION LIST**

Calibration of the Flow in the Test Section of the Low-Speed Wind Tunnel at AMRL

Lincoln P. Erm

### **AUSTRALIA**

#### **DEFENCE ORGANISATION**

##### **Task Sponsor**

##### **S&T Program**

Chief Defence Scientist	} shared copy
FAS Science Policy	
AS Science Corporate Management	
Director General Science Policy Development	
Counsellor Defence Science, London (Doc Data Sheet only)	
Counsellor Defence Science, Washington (Doc Data Sheet only)	
Scientific Adviser to MRDC Thailand (Doc Data Sheet only)	
Scientific Adviser Policy and Command	
Navy Scientific Adviser (Doc Data Sheet and Distribution List only)	
Scientific Adviser - Army (Doc Data Sheet and Distribution List only)	
Air Force Scientific Adviser	
Director Trials	

##### **Aeronautical and Maritime Research Laboratory**

Director, W. H. Schofield	
Chief of Air Operations Division, C. R. Guy	
Research Leader Avionics and Flight Mechanics, N. Pollock	
Head Flight Mechanics, N. Matheson	
Head Aerodynamic Applications, D. H. Thompson	
Head Flight Dynamics Applications, J. S. Drobik	
Author, L. P. Erm (5 copies)	
G. D. Ainger	V. Baskaran
D. M. Carnell	J. C. Clayton
G. S. Dietachmayer	C. D. Edwards
M. Giacobello	M. K. Glaister
A. A. Gonzalez	S. S. Lam
P. T. Malone	H. A. Quick

**DSTO Library and Archives**

Library Fishermans Bend (Doc Data Sheet only)  
Library Maribyrnong (Doc Data Sheet only)  
Library Salisbury  
Australian Archives  
Library, MOD, Pyrmont (Doc Data Sheet only)  
US Defense Technical Information Center (2 copies)  
UK Defence Research Information Centre (2 copies)  
Canada Defence Scientific Information Service  
NZ Defence Information Centre  
National Library of Australia

**Capability Systems Staff**

Director General Maritime Development (Doc Data Sheet only)  
Director General Aerospace Development (Doc Data Sheet only)

**Knowledge Staff**

Director General Command, Control, Communications and Computers  
(DGC4) (Doc Data Sheet only)

**Navy**

SO (Science), Director of Naval Warfare, Maritime Headquarters Annex,  
Garden Island, NSW 2000. (Doc Data Sheet only)

**Army**

ASNSO ABCA, Puckapunyal, (4 copies)  
SO (Science), DJFHQ(L), MILPO Enoggera, Queensland 4051 (Doc Data Sheet  
only)

**Intelligence Program**

DGSTA Defence Intelligence Organisation  
Manager, Information Centre, Defence Intelligence Organisation

**Corporate Support Program**

Library Manager, DLS-Canberra (Doc Data Sheet only)

**UNIVERSITIES AND COLLEGES**

Australian Defence Force Academy  
Library  
Head of Aerospace and Mechanical Engineering  
Flinders University, Librarian  
Monash University, Hargrave Library (Doc Data Sheet only)  
University of Melbourne, Library

**OTHER ORGANISATIONS**

NASA (Canberra)  
AusInfo

## **OUTSIDE AUSTRALIA**

### **ABSTRACTING AND INFORMATION ORGANISATIONS**

Library, Chemical Abstracts Reference Service

Engineering Societies Library, US

Materials Information, Cambridge Scientific Abstracts, US

Documents Librarian, The Center for Research Libraries, US

### **INFORMATION EXCHANGE AGREEMENT PARTNERS**

Acquisitions Unit, Science Reference and Information Service, UK

Library - Exchange Desk, National Institute of Standards and Technology, US

SPARES (5 copies)

Total number of copies: 60



<b>DEFENCE SCIENCE AND TECHNOLOGY ORGANISATION DOCUMENT CONTROL DATA</b>				1. PRIVACY MARKING/CAVEAT (OF DOCUMENT)	
2. TITLE  Calibration of the Flow in the Test Section of the Low-Speed Wind Tunnel at AMRL.			3. SECURITY CLASSIFICATION (FOR UNCLASSIFIED REPORTS THAT ARE LIMITED RELEASE USE (L) NEXT TO DOCUMENT CLASSIFICATION)  Document (U) Title (U) Abstract (U)		
4. AUTHOR(S)  Lincoln P. Erm			5. CORPORATE AUTHOR  Aeronautical and Maritime Research Laboratory PO Box 4331 Melbourne Vic 3001		
6a. DSTO NUMBER DSTO-TR-1073		6b. AR NUMBER AR-011-637		6c. TYPE OF REPORT Technical Report	
				7. DOCUMENT DATE November 2000	
8. FILE NUMBER M1/8/1013		9. TASK NUMBER RDI 98/179		10. TASK SPONSOR RDI	
				11. NO. OF PAGES 80	
				12. NO. OF REFERENCES 22	
13. URL ON THE WORLD WIDE WEB  <a href="http://www.dsto.defence.gov.au/corporate/reports/DSTO-TR-1073.pdf">http://www.dsto.defence.gov.au/corporate/reports/DSTO-TR-1073.pdf</a>				14. RELEASE AUTHORITY  Chief, Air Operations Division	
15. SECONDARY RELEASE STATEMENT OF THIS DOCUMENT  <i>Approved for public release</i>					
OVERSEAS ENQUIRIES OUTSIDE STATED LIMITATIONS SHOULD BE REFERRED THROUGH DOCUMENT EXCHANGE, PO BOX 1500, SALISBURY, SA 5108.					
16. DELIBERATE ANNOUNCEMENT  No limitations					
17. CASUAL ANNOUNCEMENT Yes					
18. DEFTTEST DESCRIPTORS  low speed wind tunnels, calibration, measurement, velocity, flow, turbulence, spectra					
19. ABSTRACT The circuit of the low-speed wind tunnel remained essentially the same from when the tunnel was built in 1941 until 1996 when an extended test section and a new contraction were installed. In this report, the results of a detailed calibration of the flow in the test section are given for the tunnel with the contraction as installed from 1941 to 1996. The calibration was performed to: (1) provide a data base of the flow quality, to be used when analysing tests carried out between 1941 and 1996, and (2) provide a data base for assessing the changes in the flow quality resulting from the new contraction and extended test section installed in 1996. Longitudinal mean-flow velocities, flow angles, turbulence intensities and spectra, were measured at up to 155 grid points across the flow for longitudinal positions of $x_T = -1.0, 0.0$ and $1.0$ m from the centre of the turntables in the test section for nominal free-stream velocities of 30, 45, 60 and 75 m/s. The most important area of the test section, where models are usually located, is the region comprising approximately the central 50% of the cross sectional area of the test section. In this region, over the longitudinal measurement range ( $x_T = -1.0$ to $1.0$ m), the following flow non-uniformities were observed. For the four velocities, longitudinal mean-flow velocities deviated within the range $-0.8\%$ to $+2.0\%$ from their values at the centre of the tunnel test section ( $x_T = 0.0$ m). For velocities of 30 and 60 m/s, horizontal flow angles deviated within the range $-0.8^\circ$ to $+0.8^\circ$ and vertical flow angles deviated within the range $-1.0^\circ$ to $+0.4^\circ$ . For velocities of 30 and 60 m/s, the u-component turbulence intensities were generally below 0.4%, and the v- and w-component intensities were generally below 0.7%. Corresponding spectra for the u- v- and w-components of the turbulence were relatively smooth over the frequency range 0.3 Hz to 10 kHz, with no significant spikes associated with irregularities in the flow.					